

Advances in Electronics and Electron Physics

EDITED BY
L. MARTON

National Bureau of Standards, Washington, D. C.

EDITORIAL BOARD

T. E. Allibone	W. B. Nottingham
H. B. G. Casimir	E. R. Piore
L. T. DeVore	M. Ponte
W. G. Dow	A. Rose
A. O. C. Nier	L. P. Smith

VOLUME VIII



1956

ACADEMIC PRESS INC., PUBLISHERS
NEW YORK, N. Y.

TK 7800
A 37

Copyright© 1956, by
ACADEMIC PRESS INC.
111 Fifth Avenue
NEW YORK 3, N. Y.
All Rights Reserved

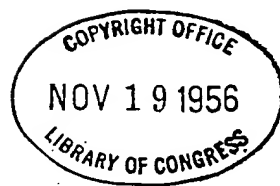
NO PART OF THIS BOOK MAY BE REPRODUCED IN
ANY FORM, BY PHOTOSTAT, MICROFILM, OR ANY
OTHER MEANS, WITHOUT WRITTEN PERMISSION
FROM THE PUBLISHERS

Library of Congress Catalog Card Number: 49-7504

THE LIBRARY OF
CONGRESS
SERIAL RECORD

NOV 27 1956

Copy



PRINTED IN THE UNITED STATES OF AMERICA

CONTENTS

CONTRIBUTORS TO VOLUME VIII v

PREFACE vii

Some New Applications and Techniques of Molecular Beams

BY JOHN G. KING AND JERROLD R. ZACHARIAS, *Department of Physics and Research
Laboratory of Electronics, Massachusetts Institute of Technology,
Cambridge, Massachusetts*

I. Introduction	2
II. Sources of Neutral Molecular Beams	12
III. Detectors of Beams of Neutral Molecules	32
IV. Deflecting and Uniform Fields	61
V. Radio-Frequency Equipment	73
VI. Miscellany	77
References	83

Field Emission

BY W. P. DYKE AND W. W. DOLAN, *Linfield College, McMinnville, Oregon*

I. Introduction	90
II. Field-Emission Theory	91
III. Experimental Test of Field-Emission Theory	96
IV. The Field-Emission Initiated Vacuum Arc	122
V. Field-Emission Microscopy	128
VI. Electrical Stability and Cathode Life	163
VII. Progress towards Practical Application	168
VIII. Experimental Techniques	172
References	182

Mass Spectroscopy

BY LARKIN KERWIN, *Université Laval, Québec, Canada*

I. Introduction	188
II. Instrumentation	189
III. Applications	233
References	246

Amplitude and Time Measurement in Nuclear Physics

BY E. BALDINGER, *University of Basel, Basel, Switzerland* AND W. FRANZEN,
University of Rochester, Rochester, N. Y.

I. Introduction	256
II. Amplitude Measurement of Signals of Variable Duration	256
III. Signal and Noise in Amplifiers and Physical Instruments	268
IV. The Timing of Nuclear Events	289
References	314

Field Emission

W. P. DYKE AND W. W. DOLAN

*Linfield College
McMinnville, Oregon*

	<i>Page</i>
I. Introduction.....	90
II. Field-Emission Theory.....	91
III. Experimental Test of Field-Emission Theory.....	96
1. Calculation of the Field Factor β	98
2. Current-Density Distribution.....	102
3. Dependence of Current Density on Electric Field.....	105
4. Space Charge in Field Emission.....	109
5. The Dependence of Field Emission on Work Function.....	111
6. The Distribution in Energy of Field-Emission Electrons.....	118
7. Energy Exchanges during Electron Emission at High Fields.....	120
8. The Dependence of Current Density on Temperature and Field.....	121
IV. The Field-Emission Initiated Vacuum Arc.....	122
V. Field-Emission Microscopy.....	128
1. Introduction.....	128
2. Magnification and Resolving Power.....	129
3. Emission from Clean Metals.....	133
4. On the Visibility of Single Adatoms and Admols.....	137
5. Adsorption and Desorption.....	143
6. Pulsed T-F Emission Microscopy.....	147
7. Electron Emission from a Single Lattice Step.....	148
8. Surface Migration.....	153
a. Clean Metals in the Absence of Externally Applied Surface Stress.....	153
b. Clean Metals in the Presence of Externally Applied Surface Stress.....	158
c. The Surface Migration of Adsorbates.....	160
VI. Electrical Stability and Cathode Life.....	163
1. The Cold Cathode with Steady-State Fields.....	163
2. The T-F Emitter with Pulsed Fields.....	166
VII. Progress towards Practical Application.....	168
1. Large Total Current.....	168
2. Application to X-ray Devices.....	171
VIII. Experimental Techniques.....	172
1. Fabrication of Metal Cathodes.....	172
2. Determination of Cathode Geometry.....	177
Appendix I.....	180
Appendix II.....	182
References.....	182

I. INTRODUCTION

Electrons are emitted from a cold metal under the action of a strong electric field, a process called "field emission." The phenomenon was first reported by Wood (1); subsequent field-emission studies have made significant contributions to basic science.

The emission mechanism, which was not explained by classical methods, has been well described by wave mechanics: free electrons "tunnel" through the metal's surface potential barrier when the latter is thinned by the applied field. Experimental confirmation of the theory gave an early verification of the then-new wave mechanics; it also strongly supported the Fermi-Dirac statistical theory of electron supply within the metal. More recently, the field-emission electron-projection microscope has fostered important basic advances. Among those described herein are studies of emission effects possibly due to single adsorbed molecules and atoms, surface migration of both adsorbates and the cathode material itself, desorption of contaminants, etc. Recently, pulse electronic techniques have extended field emission studies to very high current densities at which the theory has been re-examined, space-charge effects noted, and the field-emission initiated vacuum arc studied. There are also new studies concerning electron emission from metals when both temperature T and electric field F are high, i.e., $T\text{-}F$ emission.

A review of the more recent basic advances in field and $T\text{-}F$ emission is undertaken in the following pages. A discussion of much of the earlier work is left to the excellent surveys of Jenkins (2) and Müller (3); in particular, this work adds to, but attempts to avoid duplication of the review of field emission microscopy by Ashworth (3a) which is found in Vol. III of this series.

Recent advances toward the practical application of field emission are also reported: a method has been found which stabilizes the electric performance of the pulsed cathode during long periods of operation at useful levels of power and duty cycle; a means for operating several needle-shaped cathodes in parallel has yielded peak powers of 3 Mw; a field-emission flash x-ray source is described which permits microsecond exposures and cineradiographic application. These practical advances are described, together with a number of fundamental developments on which they depend. The latter may permit both new basic studies and important electron device developments which employ the unique electrical properties of the field and $T\text{-}F$ emitters (4). Notable among such properties are these: the enormous current density, of the order 10^8 amp/cm², exceeds that of other conventional cathodes by a factor of a million; no energy need be added to cause field emission; current density depends exponen-

FIELD EMISSION

tially on the applied electric field and hence is subject to direct electronic control; the minute emitting surface provides a virtual point source useful in electron optical devices.

A general review of the recent advances in field emission appears timely in view of the foregoing developments and increased activity in this field of work. To aid the newcomer, a short section on techniques is included.

The field-ion microscope, a device of interest and importance in the microscopy of surfaces as developed by Müller (3, 5a), is closely related to the field-emission microscope in purpose and in physical embodiment, but does not employ electron-emission phenomena and is thus judged by the present authors to be outside the scope of this paper; furthermore, most of the published material concerning it is already included in Müller's review (3), to which the reader's attention is directed.

II. FIELD-EMISSION THEORY

The basic theoretical considerations of a theory of the emission of electrons from metals under the influence of electric field and temperature will be described and certain recent additions indicated; however, no attempt will be made here to present the general emission theory in detail. No satisfactory explanation of the field-emission phenomenon was known prior to 1928, although Schottky (5) in 1923 attempted to clarify it by assuming that the classical potential barrier would be lowered in the presence of high fields through the electron image force sufficiently to permit conduction electrons to surmount the barrier. Although this effect was verified for thermionic emission at relatively low fields (the Schottky effect), it failed in the case of field emission to predict the observed relationship between applied fields and current density and called for a more rapid increase of emission with temperature at high fields than was measured experimentally. No refinement of classical theory proved capable of resolving such difficulties, but the development of wave mechanics opened the way to an inclusive and experimentally valid theory through discovery of the tunnel effect.

Fowler and Nordheim (6) succeeded in applying wave-mechanical methods to the problem in 1928, adding the effect of the image force later (7); probably the presentation of Sommerfeld and Bethe (8) is the clearest discussion available. It is important to understand the basic assumptions underlying this development, since many refinements have been suggested through changes in assumptions or the addition of new conditions. The usual development assumes the following: (1) a simple one-band electron distribution using the Fermi-Dirac statistics; (2) a smooth, plane metal surface where irregularities of atomic dimensions are

neglected; (3) a classical image force; (4) a uniform distribution of work function.

Under such assumptions one has a situation such as that expressed by Fig. 1. Within the metal (at left in the figure) the significant quantity is the electron supply function $N(\epsilon, T)$. At a given absolute temperature T , this function measures the relative number of electrons whose kinetic

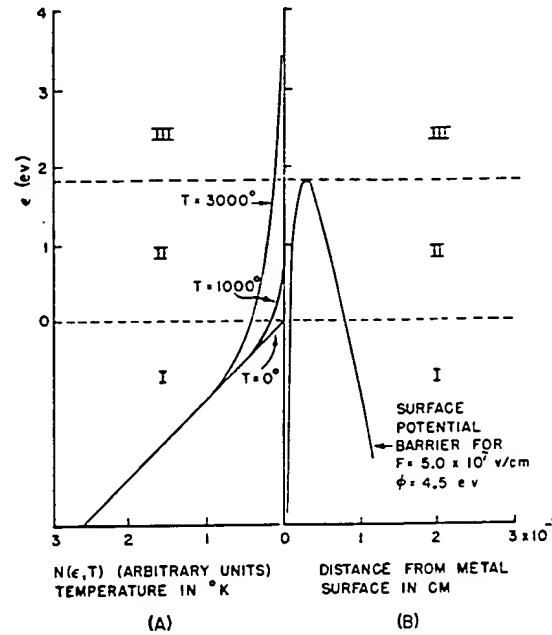


FIG. 1. Schematic drawing showing, on the left, the electron supply function $A(\epsilon, T)$ in a metal for several values of the temperature T , and, on the right, the potential barrier for a typical value of the electric field, the vertical line at 0 representing the metal surface. Region I, below Fermi level at $\epsilon = 0$, corresponds to field emission; Region III, above the barrier, to thermal emission; if there is appreciable emission from Region II, between Fermi level and top of barrier, the total emission is called T-F emission.

energy, based on the component of velocity normal to the surface, has the value ϵ . When $T = 0$, the upper limit of energy is at the so-called "Fermi level," which is here used as an origin for the variable ϵ . At higher temperatures the supply function acquires a "thermal tail," which lifts an increasing number of electrons to higher energy levels, where emission is more readily achieved. This function, as used by Sommerfeld and Bethe, has the form

$$N(T, \epsilon) = \ln [1 + \exp (-\epsilon/kT)] \quad (1)$$

where k is the Boltzmann constant.

In the presence of suitably large values of the electric field F , the potential barrier becomes thinned and lowered, as illustrated at the right in Fig. 1. Electrons impinging on this finite barrier from inside the metal have a certain probability of penetrating the barrier and appearing outside the metal. The probability is expressed by a transmission coefficient which has been calculated by several authors (7-11), in a variety of final forms. Of these the simplest and most readily adapted to further calculation is again that of Sommerfeld and Bethe (8), from which the various alternate forms do not differ by more than a factor of 2 at pertinent energy levels. The transmission coefficient may be written

$$D(F, \epsilon, \phi) = \exp [-6.83 \times 10^7 (\phi - \epsilon)^{3/4} f(y)/F] \quad (2)$$

Here ϕ is the electron work function in ev, F is the electric field in v/cm, ϵ is in ev, and $f(y)$ is a dimensionless elliptic function of the variable $y = 3.79 \times 10^{-4} F^{1/2}/(\phi - \epsilon)$, introduced by Nordheim (7) in taking account of the image force. Nordheim's original tabulation of $f(y)$, also quoted by Sommerfeld and Bethe, contained errors which have been corrected recently by Burgess, Kroemer, and Houston (12), whose table reads as follows:

TABLE I

y	$f(y)$	y	$f(y)$
0.00	1.0000		
.05	.9948	0.55	0.6351
.10	.9817	.60	.5768
.15	.9622	.65	.5152
.20	.9370	.70	.4504
.25	.9068	.75	.3825
.30	.8718	.80	.3117
.35	.8323	.85	.2379
.40	.7888	.90	.1613
.45	.7412	.95	.0820
.50	.6900	1.00	0.0000

The numerical factors in Eq. (2) and in the expression above for y were also adjusted by Burgess, Kroemer, and Houston in conformity with improved values of the physical constants.

It is clear that the number of available electrons at a given energy level, multiplied by the transmission coefficient and integrated over all energies, must yield the emission current J , which may thus be written

$$J \text{ (electrons/cm}^2 \text{ sec)} = \int_{-\infty}^{\infty} cN(T, \epsilon) D(F, \epsilon, \phi) d\epsilon \quad (3)$$

in which the constant c has the form $4\pi mkT/h^3$, where m is the mass of the electron and h is Planck's constant.

Although Richardson's law for thermionic emission,

$$J = A_1 T^2 e^{-\phi/kT} \quad (4)$$

was originally derived otherwise, it can be obtained readily by integration of Eq. (3) under the assumption of high T and low F , the integral being significant only in Region III of Fig. 1, above the potential barrier.

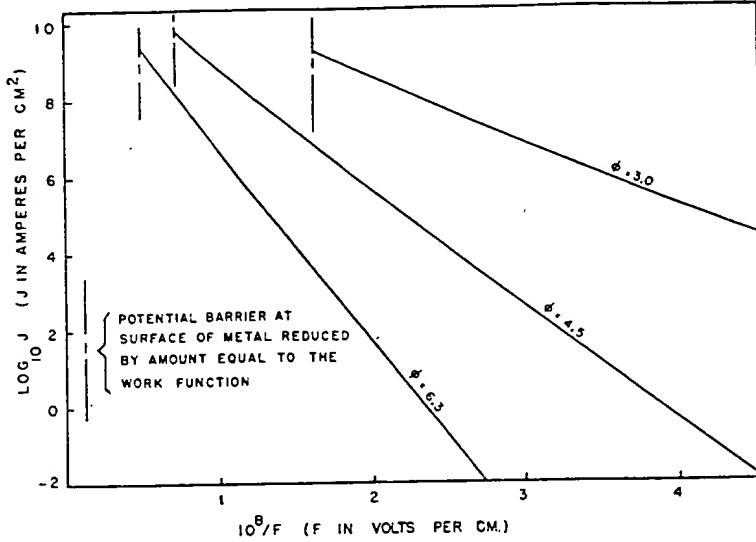


FIG. 2. Graphs of the modified Fowler-Nordheim relation of Eq. (5), showing field-current density J as a function of applied surface electric field F , for several values of the work function ϕ in ev.

In such conditions the barrier is too thick to permit any appreciable tunnel effect.

When T is assumed zero, one obtains pure field emission, with no electrons surmounting the barrier. In this case Eq. (3) can be integrated analytically by use of reasonable approximations and leads to the Fowler-Nordheim equation

$$J = (1.54 \times 10^{-6} F^2/\phi) \exp [-6.83 \times 10^7 \phi^{3/2} f(y)/F] \quad (5)$$

where numerical values, as before, use Burgess, Kroemer, and Houston's corrections, and the current density J is in amp/cm² when F is in v/cm and ϕ in ev. Appreciable field emission is observed at fields greater than 3×10^7 v/cm. Tables of J for several values of ϕ and a wide range of useful fields have been published (18), and are included here in Appendix I.

In Fig. 2 are shown typical graphs of the convenient logarithmic form of Eq. (5) for three different values of ϕ .

The distribution in energy of the emitted electrons in cold field emission has been calculated and experimentally verified by several authors (14-17); more recently, the distributions shown in Fig. 3 were derived for a wide range of both electric field and temperature (18). The illustrations of Fig. 3 indicate how narrowly the emission is confined to the neighborhood of the top Fermi energy level at low cathode temperatures.

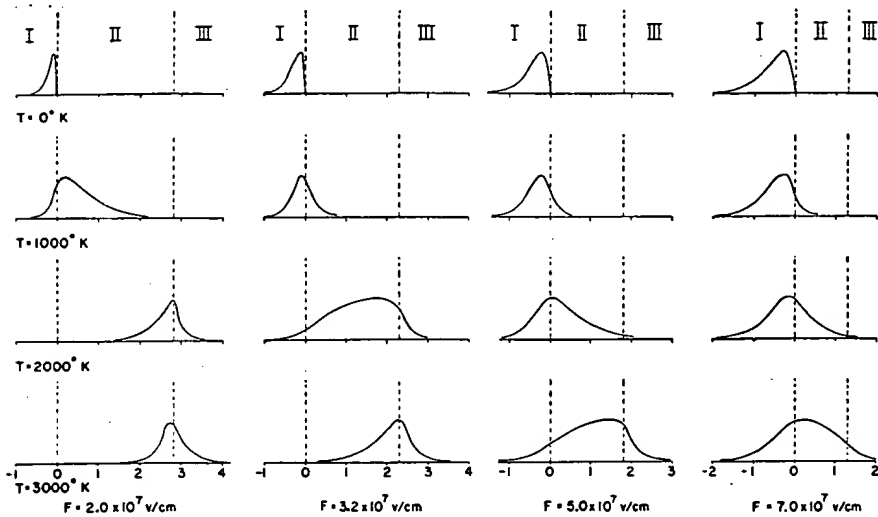


FIG. 3. Theoretical energy distributions for emitted electrons at indicated fields and temperatures, for $\phi = 4.5$ ev, with amplitudes arbitrarily normalized to a common maximum; abscissas ϵ in ev relative to the top Fermi level at 0. Regions I, II, III correspond to those in Fig. 1.

Recently the yield of Eq. (3) has been calculated when T and F are both high enough to permit appreciable emission both over and through the potential barrier (18); the descriptive term T - F emission has been applied to this case. Early investigators (19, 20) looked for a temperature effect in field emission but did not find it significant in their experimental conditions. Guth and Mullin (9) integrated Eq. (3), using their own form of the transmission coefficient, but had to make modifications in the equation in order to perform an analytic evaluation of the integral, so that the results were applicable at high temperatures for only a restricted range of fields. Nakai (21) recently calculated the integral numerically for the special case of no image force.

It is a straightforward task to integrate Eq. (3) numerically after calculating the values of the supply function A and the transmission coeffi-

cient D over the entire significant range of energies for a desired combination of T and F . The method of Simpson is easily applied and leads simultaneously to energy-distribution curves and total emitted current. The results are illustrated in Figs. 3 and 4, while Appendix II offers a partial tabulation of current for various fields, temperatures, and work functions.

The general characteristics of Fig. 4 were predicted by Houston in 1929 (22), and are in agreement with Guth and Mullin as far as comparisons can be made. Emission is greatly increased by added temperatures at the lower range of fields shown, but the effect is small at the higher

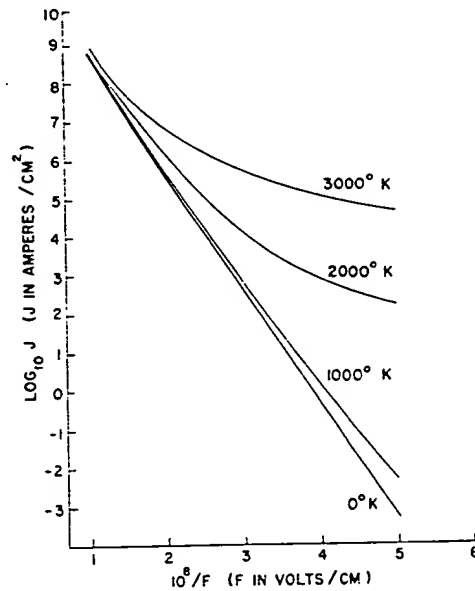


FIG. 4. Graph relating calculated current density J to electric field F at various temperatures T , for $\phi = 4.5$ ev.

values of the field. The significance of T - F emission in the search for emitter stability is discussed in Section VI.

It would be desirable to re-examine the theory subject to refined boundary conditions for clean metals, considering at least a nonclassical image force (22a), the properties of the surface as influenced by its structure of atomic scale, and the band structure in the electron supply function.

III. EXPERIMENTAL TEST OF FIELD-EMISSION THEORY

There are important reasons for subjecting field-emission theory to an experimental test. The wave-mechanical process by which charged par-

ticles penetrate a potential barrier can be accurately examined when the particles are electrons for which convenient experimental techniques are available. It is possible also to judge the validity of the electron supply function, and from the failings of the theory to learn more about effects due to space charge and refined boundary conditions needed for further improvement of the theory.

Equally important is the fact that most field emission experiments have been interpreted through the assumed validity of Eq. (5); in such cases the experimental uncertainty depends directly on that of the emission theory, and refined experimental tests of Eq. (5) correspondingly clarify a great deal of published work.

It is not an easy job to measure ϕ and F at a metal surface whose cross section is about 1μ ; however, recently improved techniques make that task much simpler and its results more accurate. Because of their importance, such techniques are emphasized in this section; thereafter, the experimental test of Eq. (5) is discussed through use of those techniques.

An experimental test of Eq. (5) requires a simultaneous determination of the values of the variables J , F , and ϕ . It is convenient in practice to record current I and voltage V , thereafter deriving J and F from the following relationships:

$$I = \int_0^A J dA \quad (6)$$

where I is in amperes, A is the emitting area in square centimeters, and

$$F = \beta V \quad (7)$$

where V is in volts and β is a geometrical factor in cm^{-1} whose derivation is described in the following pages.

Substitution of Eq. (7) in (5) and Eq. (5) in (6) yields

$$I = \int_0^A 1.54 \times 10^{-6} \frac{(\beta V)^2}{\phi} \exp \left[-6.83 \times 10^7 \phi^{3/4} \frac{f(y)}{\beta V} \right] dA \quad (8)$$

which for the special case of constant values of A , ϕ , and the area distribution of J can be approximated as

$$I = Ce^{-D/V} \quad (9)$$

where C and D are appropriate constants.

The latter relationship between I and V was discovered experimentally by Millikan and Lauritsen (23), prior to its theoretical derivation and remains correct today, to a good approximation, for current densities less than those for which space-charge effects are observed ($J < 6 \times 10^6$ amp/cm² for $\phi = 4.5$ ev; see Section III,4). Clearly, the constants C

and D will vary from emitter to emitter, depending on the given values of ϕ , β , and A . Typical values of the latter are described in the following sections.

We discuss next means for obtaining values of β , A , and the distribution of J over the emitting area and apply them thereafter to a test of the theory.

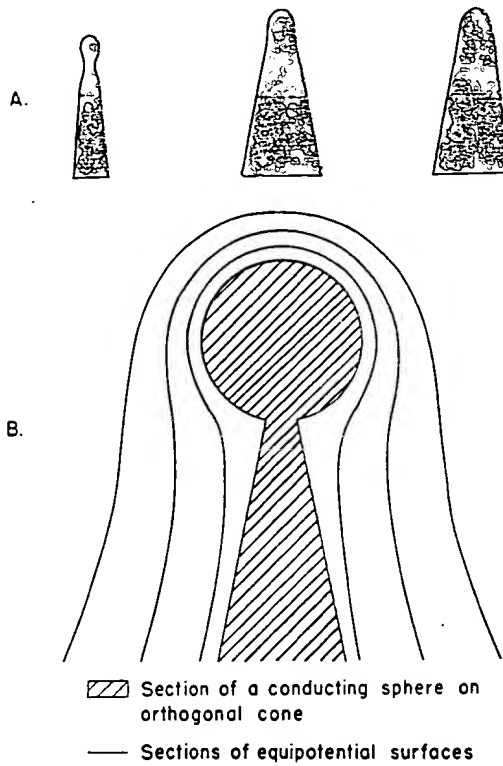


FIG. 5. A comparison between (a) typical field emitter geometries from electron micrographs and (b) equipotential surfaces surrounding a charged, isolated sphere-on-orthogonal-cone.

1. Calculation of the Field Factor β

In order to provide appreciable field-current density, electric fields in the range $3 \times 10^7 < F < 7 \times 10^7$ v/cm are required. To establish such fields with convenient values of potential, e.g., in the kilovolt range, the cathode is usually needle-shaped, approximating a cone with hemispherical tip of cross section of the order of a micron. Typical geometries of tungsten cathodes are shown in Fig. 5a; methods for fabricating such

cathodes and obtaining their geometries from electron micrographs are discussed in Sections VIII,1 and VIII,2, respectively.

Direct measurement of the cathode electric field is difficult because of its high value, its large space rate of change, and the microscopic cathode size. One therefore obtains the field value through Eq. (7), using measured values of the applied voltage and values of β calculated by one of the following methods.

The value of β may be computed from the electrode geometries by use of potential theory. When electron space charge is negligible in the region between electrodes, solutions of Laplace's equation are applicable, a case which is treated in this section. When space charge is appreciable, Poisson's equation is solved subject to boundary conditions appropriate to field emission, a case covered in Section III,4.

The value of β can be calculated at all points on a cathode surface which is closely fitted with a suitable equipotential surface from a family, one of which also conforms to the experimental anode surface. Approximate values of β have been derived, using hyperbolic (24) and parabolic surfaces (25); however, it has been shown to be difficult to fit such forms to cathode geometries as revealed by electron microscopy (26), values of β being correspondingly inaccurate by as much as a factor of 2.

By the hyperboloidal approximation, the electric field F at the vertex of the hyperboloid in the case $r \ll R$ is $F = 2V/r \ln(4R/r)$, where r is the emitter radius, R is the cathode-anode spacing, and V is the applied potential between electrodes. An approximation for the paraboloidal case, using the same notation, is $F = 2V/r \ln(2R/r)$.

More recently (26), equipotential surfaces surrounding a charged isolated sphere-on-orthogonal-cone (Fig. 5) have been shown to fit well the typical cathode geometries shown in that figure. Such an equipotential system has been used to provide values of β whose accuracy is limited primarily by available techniques in electron microscopy, e.g., a 5-to-10% error. This method is presented briefly as follows.

For the potential distribution surrounding a charged, isolated sphere-on-orthogonal-cone, one uses (27)

$$V = \frac{V_R}{R^n} [r^n - a^{2n+1} r^{-n-1}] P_n(\cos \theta) \quad (10)$$

where r and θ are ordinary plane polar coordinates referred to the center of the sphere as origin and the pole of the sphere opposite its contact with the cone as zero direction; R is the anode distance, V_R the applied potential, a the radius of the sphere, and P_n the Legendre function with n chosen so that the function vanishes when θ is equal to the exterior half-angle α of the cone.

The theoretical anode corresponding to the equipotential system defined by Eq. (10) can be described by setting $V = V_R$. In this case the second term in the parentheses becomes negligible, and the polar equation of the anode is

$$r^n = \frac{R^n}{P_n(\cos \theta)} \quad (11)$$

The surface described by Eq. (11) somewhat resembles a paraboloid; it can be readily reproduced as an experimental anode.

To draw a chosen equipotential conforming to a given emitter, one has three variables in Eq. (10) at his disposal: n , related through the Legendre function to the cone angle of the core cone (dashed lines, Fig. 6), a , the radius of the sphere, and V , the potential above that of the core. After some experimentation it is not difficult to find a combination of these parameters that leads to a surface closely approximating a given emitter profile.

The equipotential surface fitted to a typical emitter in Fig. 6 was derived from Eq. (10), where $n = 0.10$, $a = 1.235 \times 10^{-5}$ cm, and $r_0 = 4.00 \times 10^{-5}$ cm (r_0 is the value of r at $\theta = 0$ deg on the surface which approximates the emitter). For the surface of Fig. 6 the value β_0 at the emitter apex is

$$\beta_0 = \frac{F_0}{V_R - V} = \frac{r_0^{n-1}}{R^n} \left[n + (n+1) \left(\frac{a}{r_0} \right)^{2n+1} \right] \frac{V_R}{(V_R - V)} \quad (12)$$

where V_R is the potential difference between core and anode, V is the potential on the surface which was substituted for the emitter, and $V_R - V$ is the potential difference between the emitter (i.e., the substitute surface) and anode; F_0 is the electric field at the emitter apex, i.e., the negative gradient of V evaluated at $r = r_0$, $\theta = 0$ deg.

The values of β defined as $F/(V_R - V)$, at various points on the substitute cathode surface are found in the usual way when the electric field components are derived from the potential gradient, with the aid of Eq. (10). There results

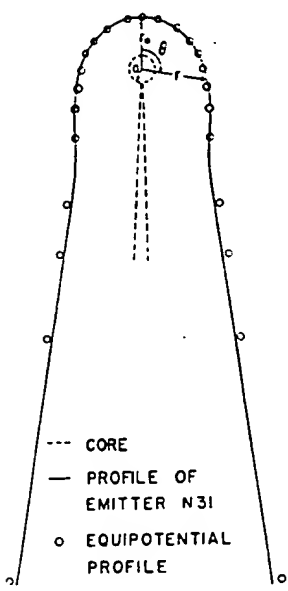


FIG. 6. An enlarged profile of a typical field emitter (from an electron micrograph) fitted with an equipotential surface from Eq. (10), using the values $n = 0.10$, $a = 1.235 \times 10^{-5}$ cm, and $r_0 = 4.00 \times 10^{-5}$ cm.

$$\frac{\beta}{\beta_0} = \left(\frac{r}{r_0}\right)^{n-1} \frac{\{[n + (n+1)(a/r)^{2n+1}]^2 [P_n(\cos \theta)]^2 + [1 - (a/r)^{2n+1}]^2 [dP_n(\cos \theta)^2/d\theta]\}}{[n + (n+1)(a/r_0)^{2n+1}]} \quad (13)$$

Values of β/β_0 are shown in Fig. 7 for extremities of cathode geometry

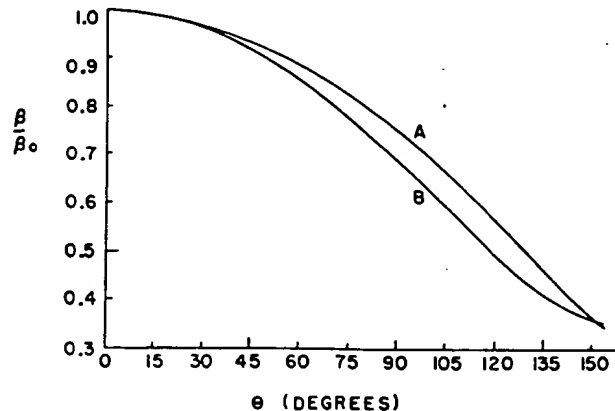


FIG. 7. A graph showing the dependence of the ratio β/β_0 upon polar angle θ for the emitter profiles (a) and (b), respectively, of Fig. 8.

frequently encountered in practice; those geometries as obtained from electron micrographs are shown in Fig. 8. Values of $P_n(\cos \theta)$ were obtained from a numerical evaluation of its hypergeometric series (27). Values of $P_n(\cos \theta)$ are given in Table II.

It may be necessary to correct calculated values of β for effects due to electrical charges on surfaces near the cathode needle. For example (28), a cathode support structure similar to that shown in Section VIII,1 was found to decrease β by 7%.

As an alternative, it is often convenient to calculate β from Eqs. (5) and (7) when J , ϕ , and V are known from experiment. By this method, the value of β is known within limits determined by the uncertainty of Eq. (5), whose electric field dependence has been established within 15% (see Section III,3).

More recently, Drechsler and Henkel (29) have proposed a method for calculating β in which the cathode configuration is approximated by

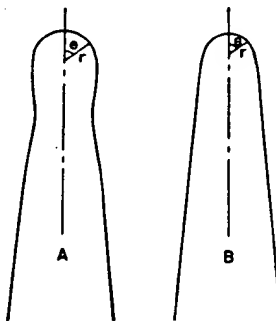


FIG. 8. Typical emitter profiles, (a) with neck constriction, and (b) without constriction, corresponding respectively to curves (a) and (b) of Fig. 7.

TABLE II. Values of $P_n(\cos \theta)$ for Various Values of n and θ

θ	$n = 0.21$ $\alpha \approx 169^\circ$	$n = 0.14$	$n = 0.11$	$n = 0.01$	θ	$n = 0.16$ $\alpha \approx 175^\circ$
15°	0.996	0.997	0.998	0.9998	13°	0.997
30°	0.982	0.989	0.992	0.9993	29°	0.986
45°	0.960	0.975	0.981	0.9984	39°	0.975
60°	0.928	0.955	0.965	0.997	55°	0.950
75°	0.880	0.927	0.944	0.995	65°	0.929
90°	0.831	0.892	0.917	0.993	75°	0.904
105°	0.762	0.850	0.882	0.990	90°	0.872
120°	0.673	0.789	0.837	0.986	100°	0.842
135°	0.557	0.712	0.776	0.981	110°	0.803
150°	0.395	0.602	0.692	0.974	120°	0.756
165°	0.250	0.420	0.565	0.959	130°	0.701
					140°	0.632
					150°	0.543
					160°	0.450

combined equipotentials from the spherical and hyperboloidal solutions. Simplicity accrues from use of only two variables, the cathode radius and a fraction α which determines the contribution of the two equipotentials. Ratios of β/β_0 found by this method are in good agreement with those shown in Fig. 7; however, the absolute value of β may suffer from difficulties in fitting some cathode forms commonly found.

2. Current-Density Distribution

Values of field-current density J have been experimentally measured at a few crystal faces having low indexes on the hemispherical tungsten cathode tip by (1) direct measurement of the electron emission current (15, 30, 31), and (2) photometric measurement of the light output from a phosphor-on-conducting-glass screen on which such electrons were incident (32). Those measurements are discussed in Section III,5.

Improved photometric measurements were recently extended to a sufficient number of crystal faces to derive accurately both a value for the total emitting area and the average value of current density over that area (33).

Graphs from the latter work showing the variation of J with polar angle θ for several azimuths of a clean hemispherical tungsten cathode are shown in Fig. 9. For a similar cathode, the graph of current density, averaged over all azimuths at successive values of θ , is shown in Fig. 10; in this case the polar axis was intentionally chosen asymmetric with the crystal symmetry. The latter graph was used with the tables in Appendix I to verify the ratios β/β_0 shown in Fig. 7. Houston (34) has inde-

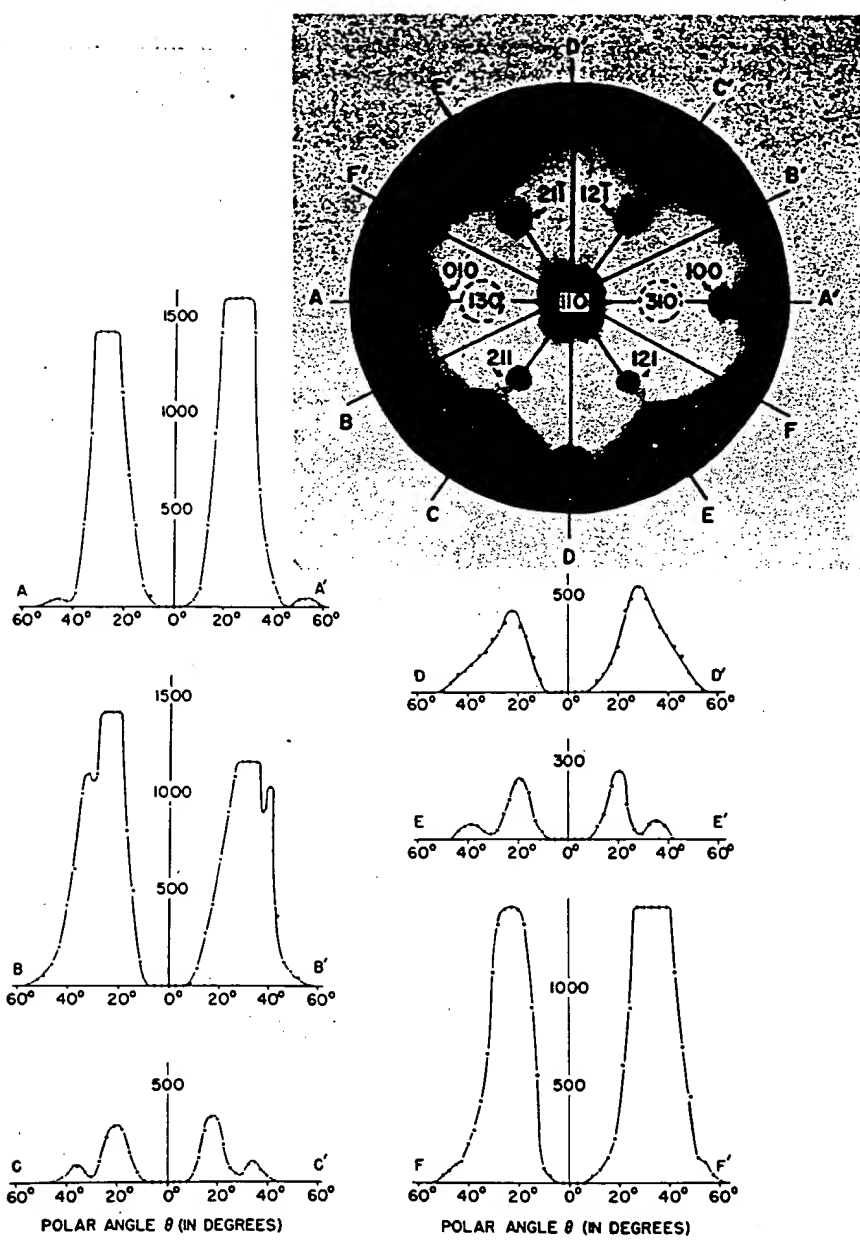


FIG. 9. Graphs illustrating the variation of current density J with polar angle θ for several azimuths of a typical emitter; vertical scale arbitrary; needle axis coincides with (110) crystal direction. Upper right: emission pattern for same emitter, with identification of principal crystal faces and positions of azimuths AA' , etc., for the corresponding graphs.

pendently verified the same ratios by a similar method, and Drechsler and Henkel (29) obtained a comparable relationship.

The distribution of emitting area may be measured quantitatively from Fig. 9, using the emitter radius as revealed in the electron microscope; however, it is often convenient and adequate to define the total effective area by reference to a graph of the type in Fig. 10. Using the

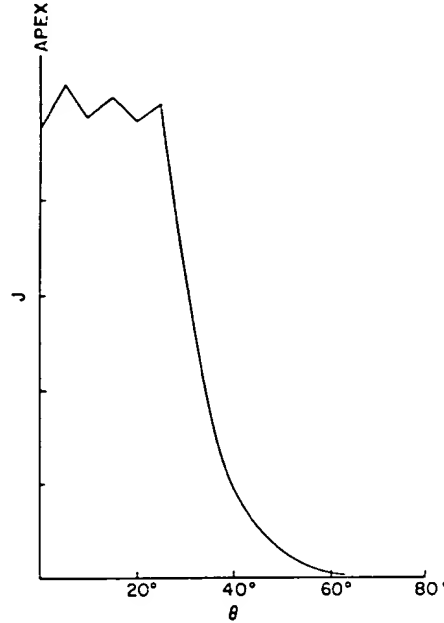


FIG. 10. Current density J as a function of polar angle θ averaged over all azimuths for an emitter whose emission pattern was asymmetrical with the polar axis; vertical scale arbitrary.

latter, and ignoring $J < 0.01J_{\max}$, the emitting area A for that particular cathode is included in the interval $0 < \theta < 60^\circ$. Using θ thus determined, and the known emitter tip radius r , the emitting area is found from

$$A = 2\pi r^2(1 - \cos \theta) \quad (14)$$

Typical values of A for single needle-shaped cathodes are $10^{-10} < A < 10^{-7} \text{ cm}^2$. For a given radius, the area is influenced by the dependence of β/β_0 on θ (Fig. 7) and it increases with increasing values of electric field (Section III,3).

An average value \bar{J} of current density for any area A is derived from

$$\bar{J} = \frac{I}{A} \quad (15)$$

where I is the measured current from A ; values of \bar{J} differ by about a factor of 1.5 as derived from the total area and as derived from that part of the area near the emitter tip for which the electric field is constant to within a few percent ($\theta < 30^\circ$, Fig. 10). Since that factor is small compared with other uncertainties, the value of \bar{J} used for the comparison with theory in the following section was derived from Eq. (15), using the total emitting area.

3. Dependence of Current Density on Electric Field

Several early experimenters related observed field current to applied voltage in the manner of Eq. (9), and such work is well summarized by both Jenkins (2) and Müller (3). In such work, field currents were detected at a field one to two orders of magnitude lower than expected from Eq. (5); this effect was later attributed to unresolved surface roughness. Only recently have the improved techniques described above permitted the simultaneous experimental determination of J , F and ϕ in a manner adequate to test Eq. (5).

Müller (35) recorded current and voltage from a tungsten cathode whose emission pattern was observed in the field emission microscope described in Section V. The pattern revealed that the cathode was clean, which justified use of $\phi = 4.5$ ev obtained from thermionic measurements; the pattern was also used to determine the emitting area in a manner satisfactorily approximating that described in Section III,2. The emitter radius was estimated in an oil-immersion microscope and used with the hyperbolic approximation to derive β . From β and the measured voltage, the electric field was calculated as in Eq. (7). The resulting agreement established within a factor of 2 the electric-field dependence of the wave-mechanical theory, Eq. (5). The principal experimental uncertainty was introduced by the inadequacies of optical microscopy and the hyperboloidal approximation of cathode geometry.

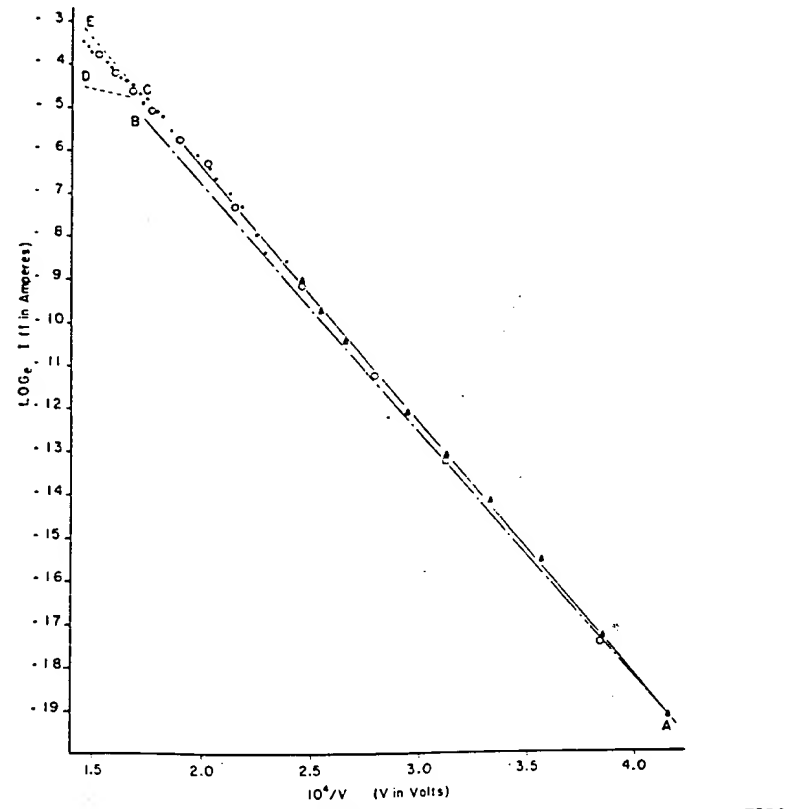
The next significant refinement in the experimental test of Eq. (5) was introduced by Haefer (36), who used the electron microscope with its better resolution to reveal the cathode geometry. The electric field was calculated by the hyperbolic method; current densities were derived from measured currents by a method equivalent to Eq. (15). Using the abbreviated theoretical equation,

$$J = C_1 F^2 e^{-D/F} \quad (16)$$

and the known average value of $\phi = 4.5$ ev for tungsten, Haefer found $\ln C_1 = 5.10$ and $D = 2.76 \times 10^8$ v/cm, in good agreement with theory. This may have been fortuitous in view of uncertainties introduced by (1) use of the hyperbolic method for calculating β , (2) omission of a correc-

tion in β for the effect of the support filament, and (3) lack of a viewed emission pattern from which to judge that the cathode was clean and hence to justify the assumed value of ϕ .

A new experimental test of Eq. (5) has recently been undertaken (28) which is based on earlier methods with the following improvements: the



△ Direct currents ○ Pulsed currents ○ Data reproduced; emitter X89

FIG. 11. Field current-voltage graph for combined pulse and direct current operation of emitter X89. Curve AB corresponds to the hypothetical case of a constant emitting area equal to that at A. Curve ACE was predicted by the theory of Eq. (5); the deviation of experimental data in the region CE is attributed to space charge in Section III,4.

current and voltage measurements and a photograph of the cathode emission pattern were recorded simultaneously from a field-emission microscope type tube; the emitting area A and an average current density J were determined by the methods described in Section III,2; β was calculated by the "sphere-on-cone" method of Section III,1, using the cathode geometry from electron micrographs; observations were made over an ex-

tended range of current densities, $100 < J < 10^8$ amp/cm², by use of pulse electronic techniques at the higher levels.

A typical current-voltage relationship obtained from a clean tungsten needle, in which direct-current and pulse observations are combined, is shown in Fig. 11. This graph has several significant characteristics. First, the portion *AC* is nearly linear; in that portion, $J < 6 \times 10^6$ amp/cm² and Eq. (5) is applicable when *F* is calculated from Eq. (7). Second, in the portion *CE*, current density falls below the dashed line predicted by Eq. (5), an effect which is shown in Section III,4 to be due to space charge; however, Eq. (5) also applies in this portion when *F* is calculated

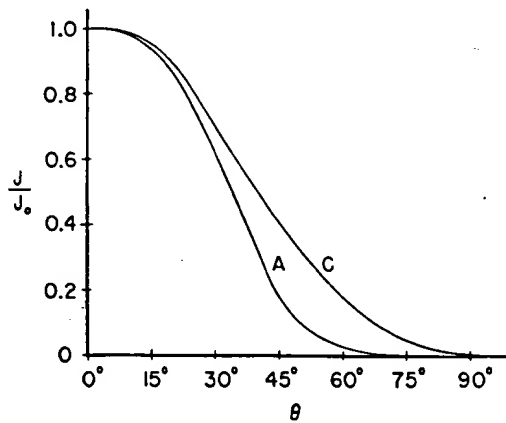


FIG. 12. Current density *J* as a function of polar angle θ for emitter X89 calculated from Eq. (5), using values of β/β_0 from curve *B*, Fig. 7, and assuming a constant work function 4.5 ev; curves *A* and *C* correspond to $F_0 = 3 \times 10^7$ v/cm and $F_0 = 7 \times 10^7$ v/cm at points *A* and *C* of Fig. 11, respectively.

through Poisson's equation in the manner of Section III,4. Third, the data are reproducible provided current density is less than about 10^8 amp/cm², corresponding to the point *E*; at larger current densities, the cathode undergoes geometric alteration during a low-impedance vacuum arc (see Section IV).

In order to use the data in the linear portion *AC* for a test of the theory, one must first correct for a gradual increase in emitting area expected with increasing field. This correction is seen from Fig. 12, whose graphs were calculated from the curves for β/β_0 in Fig. 7, together with the current-density tables of Appendix I. Figure 12 predicts the ratio J/J_0 vs θ for the two values of electric field applicable at *C* and *A*, respectively, in Fig. 11; for $F_C = 7 \times 10^7$ v/cm, the significant emission extends to a polar angle $\theta = 90^\circ$, whereas for $F_A = 3 \times 10^7$ v/cm, the emitting area is bounded at about $\theta = 60^\circ$. Using those values of θ in

Eq. (14) together with the emitter radius $r = 2.3 \times 10^{-5}$ cm from electron micrographs, the corresponding emitting areas are $A_c = 1.2 \times 10^{-9}$ cm² and $A_A = 7.6 \times 10^{-10}$ cm². The observed area increase is such that in its absence the current-voltage relationship would have followed the hypothetical curve AB in Fig. 11. Using the areas just calculated and the corresponding experimental currents at C and A , Fig. 11, the corresponding current densities were calculated from Eq. (15); they are $J_c = 6 \times 10^6$ amp/cm² and $J_A = 6$ amp/cm². The corresponding values of electric field, F_c and F_A , were calculated from Eq. (7), using the voltages V_c and V_A ,

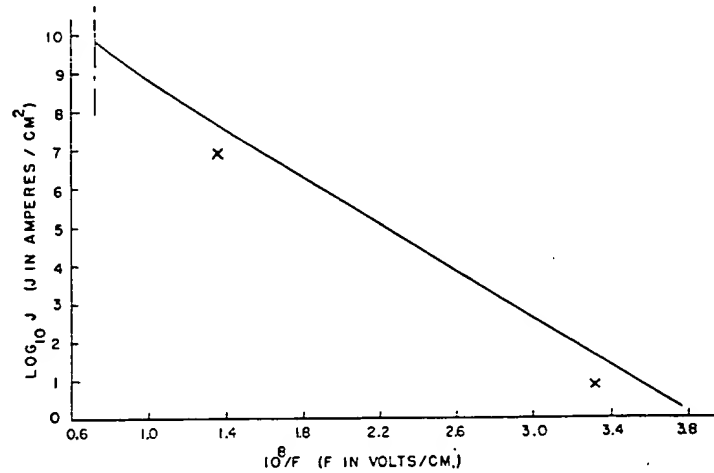


FIG. 13. Current density J as a function of electric field F at work function 4.5 ev, calculated from Eq. (5) (solid line); indicated experimental points correspond to points A and C of Fig. 11.

respectively, from Fig. 11. For this purpose, $\beta_0 = (9.9 \pm 1.5) \times 10^3$ cm⁻¹ was calculated from Eq. (12) with $a = 0.33 \times 10^{-5}$ cm, $r_0 = 1.8 \times 10^{-5}$ cm, $n = 0.07$. This value of β included a 7% correction for the effect of the cathode support structure.

The resulting experimental data are plotted in Fig. 13; the solid curve is taken from the wave-mechanical theory, Eq. (5), with the help of the tables in Appendix I. The electric-field dependence of Eq. (5) is confirmed within an error of 15% for direct-current measurements and within $\pm 20\%$ for pulse observations. Figure 13 has been redrawn since its original publication, to conform with Burgess, Kroemer, and Houston's theory corrections (12).

The foregoing agreement between experiment and theory was valid for $J < 6 \times 10^6$ amp/cm², for which space charge was negligible. When

space-charge effects are considered, the agreement is extended to higher current densities as is described in the following section.

4. Space Charge in Field Emission

Stern, Gossling, and Fowler (37) obtained a solution of Poisson's equation for plane electrodes subject to boundary conditions appropriate to field emission, particularly a nonzero cathode field F_0 . From this solution it was possible to judge values of current density for which space-charge effects were negligible and to conclude that available experimental data, then restricted to relatively low current densities by direct-current techniques, illustrated no space charge effect.

In agreement with Stern, Gossling, and Fowler, no space-charge effects were observed experimentally for current densities less than 6×10^6 amp/cm², as described in the previous section. However, when pulse electronic techniques permitted yet larger current densities to be drawn without emitter damage (28), the experimental values were found to fall below those predicted by Eq. (5), e.g., C to E, of Fig. 11. At such current densities, an elementary analysis revealed that the electron space charge in the neighborhood of the emitter surface was sufficient to reduce the applied field appreciably and possibly to cause the observed deviation (28). To investigate that possibility, a new study was required to predict the field current-voltage relationship in the presence of space charge, since the results of Stern, Gossling, and Fowler are applicable only at low space charge densities.

In the presence of space charge, the cathode field F_0 cannot be calculated from Eq. (7) and is derived in the following manner. On the assumption of plane metal electrodes and a nonvanishing value of F_0 , Poisson's equation was integrated (38), yielding a relationship between F_0 , current density J , and potential V at any distance d from the cathode. By substituting in this equation the value of J from Eq. (5), there was obtained the equation

$$4kcV^{3/2} \exp(-b/F_0) - 3V = 9k^2c^2F_0^2d^2 \exp(-2b/F_0) - 3F_0d \quad (17)$$

relating surface field to applied potential in the presence of space charge. In Eq. (17) the constant k is $2\pi(2m/e)^{1/2}$, and the parameters c and b correspond to an abbreviated form of Eq. (5), $J = cF_0^2 \exp(-b/F_0)$. For a given applied potential between plane electrodes, the cathode surface field F_0 may be calculated from Eq. (17) with $d = 1/\beta$ and the corresponding value of J obtained from the tables in Appendix I.

The resulting graphs of current density vs applied voltage have the form shown in the curve ACD of Fig. 14. Up to $J = 10^6$ amp/cm², the graph is identical with curve ACE from Eq. (5); hence, from A to C the

effect of space charge is negligible. At current densities greater than J_c , the values of J lie below the straight line CE ; then at very high levels, not yet attained experimentally, the graph approaches the curve BD , which corresponds to Child's equation,

$$J = \left(\frac{4}{9kx^2} \right) V^{3/2} \quad (18)$$

When the increase in emitting area is considered, the experimental current densities have been found to agree with the space-charge modified wave-mechanical theory for current densities up to 4×10^7 amp/cm².

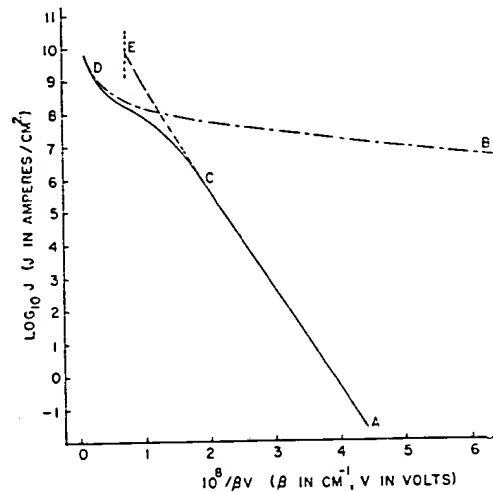


FIG. 14. Theoretical dependence of current density J on applied voltage V . Curve ACE calculated from Eq. (5) with $F = \beta V$ in the absence of space charge; curve ACD , calculated from Eq. (5) with F_0 from Eq. (17) in the presence of space charge; curve BD , Child's equation for comparison.

The agreement between experiment and theory is shown in Fig. 15, where the various work functions were obtained by depositing barium on tungsten in successive degrees of coverage.

Additional proof that space charge does limit field-current density is seen from the observed absence of current density dependence on temperature (18) and on work function (38) at a sufficiently high density. The latter is illustrated by an interesting reduction of the characteristic variation of current density with crystallographic direction as revealed in the emission pattern for the tungsten hemispherical monocrystal. This is interpreted as evidence that space charge retards further current-density increases at the areas of high emission, while current density continues to increase with increasing voltage at the areas of low emission.

While the calculated effect of space charge is sufficient to account for the departure from linearity in the current-density-voltage graph observed at high current densities, it is not necessarily the only effect contributing to such departure. The present theory assumes a plane metal surface with classical image force and a Fermi-Dirac electron supply; a re-examination of the theory subject to a nonclassical image force (22a) has been suggested (39) but not yet attempted. In addition, consideration should be given to such factors as surface roughness of atomic scale, including both its effect on β and on work function (40, 41), polarization of the emitting surface, and the band structure of the electron supply.

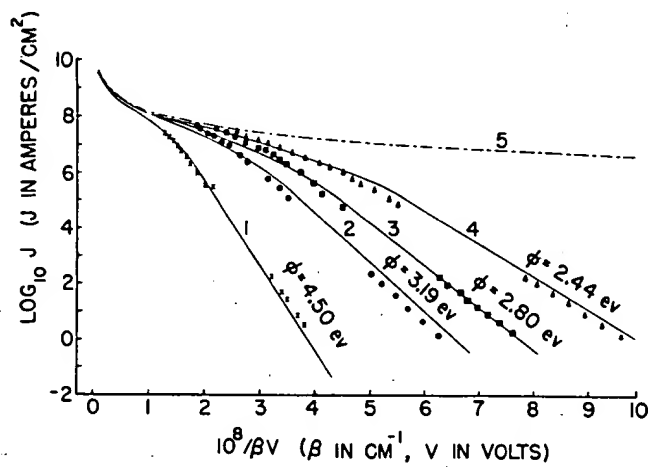


FIG. 15. Comparison of experimental data with space-charge modified field-emission theory obtained in the manner of Fig. 14 (solid lines); curve 1, clean tungsten; curves 2-4, barium on tungsten; curve 5, Child's equation.

Although it is not immediately obvious that these effects would be comparable with that of space charge, their investigation appears desirable.

5. The Dependence of Field Emission on Work Function

The work function of a metal is an important parameter in electron-emission theory. Its effect in field emission has been the basis of considerable study, and in part this section concerns experiments which verify the $\phi^{3/2}$ dependence shown in Eq. (5). In part it also concerns two field-emission methods for the measurement of work functions in general, which methods have several advantages.

When the metal under study is also the cathode of a field-emission microscope, its surface condition can be judged from the observed emission pattern; in particular, it is possible to judge the surface cleanliness.

Also, when the cathode is a hemispherical single crystal, field emission occurs at all crystal faces and may be studied simultaneously and under identical experimental conditions; such data are important when one recalls that the variation of work function with crystallographic direction is known at present only for tungsten. Furthermore, observations may be made over a range of temperatures; in particular, the use of room temperatures excludes confusion of the results by a possible thermal dependence of the work function. A disadvantage of the method is that direct measurement of the work function of the emitter's surface by other means, e.g., thermionic or photoelectric, is precluded by insufficient emission current because of the microscopic cathode area. Because much of the better work along these lines is both recent and important, a summary is given below.

Measured slopes of the current-voltage graph may be used to investigate the dependence of field emission on work function. The slope α of the $\log J/F^2$ vs $1/F$ graph is derived by differentiation of the logarithmic form of Eq. (5) as follows:

$$\alpha = \frac{d(\log_{10} J/F^2)}{d(1/F)} = -2.97 \times 10^7 \phi^{3/2} \left(f - \frac{y}{2} \frac{df}{dy} \right) \quad (19)$$

or

$$\alpha = -2.97 \times 10^7 \phi^{3/2} s(y) \quad (20)$$

The function $s(y)$ has been tabulated by Burgess, Kroemer, and Houston (12); it is close to unity for the ranges of field strengths and work functions generally encountered in experiments.

In order to test Eq. (20), the values of α predicted therefrom, using independently determined work functions, can be compared with measured values from experimental graphs, the error being sensitive to the value of β which is used in Eq. (7). In Section III, 1, errors in β as calculated for the gross cathode are discussed. Other errors may enter into the use of Eq. (20) because of the manner in which β varies locally on the hemispherical cathode surface. These include (1) a gradual decrease of β with polar angle, as in Fig. 7; (2) a decrease at "flats," i.e., crystal planes of extended area such as the (211) and (110); and (3) an increase in β at regions of surface roughness in the form of outward-grown crystallites of adsorbates or isolated atomic irregularities.

Equation (20) has been checked experimentally by two methods. In the first, average values of the work function over the emitter surface are assumed to correspond to those measured by thermionic or photoelectric methods. For various adsorbates on tungsten, the average work function is altered by an amount which is assumed to be known. This can be done

either by depositing a thick layer for which ϕ is independent of thickness, or by using an optimum coating of about a monolayer for which the work-function change is a maximum. Values of ϕ are then taken from independent measurements with similar surfaces by other methods. Two difficulties arise with this first method: first, with thick coatings, crystallites may cause localized increases in β , an effect which at one time led to the erroneous conclusion (42) that α depended on ϕ^3 in variance with Eq. (20); and second, optimum coatings appear to involve the mechanism of field emission at single adsorbed atoms, about which relatively little is known. While, for these reasons, the use of adsorbates may presently be questioned, it is interesting to note that Haefer (36) found agreement with Eq. (20) in experiments in which a tungsten needle was coated with both thick and optimal layers of Ba, K, and Cs.

In the second method, values of α are obtained from field emission at several crystal faces of the tungsten monocrystal whose corresponding work functions have been determined by other means. Wilkinson (32) established the $\phi^{3/2}$ dependence of Eq. (20) by that method, using Nichols' values of ϕ from thermionic measurements (43), and experimental values of α from a photometric analysis of the emission pattern as viewed on a calibrated phosphor screen. The work function distribution observed by Wilkinson for the strongly emitting planes is presently accepted as correct; however, revision of his results have been necessary at the weakly emitting planes, e.g., (110), for which spurious effects at the phosphor screen masked the true emission. These effects may have included secondary electrons, scattered light, internal light reflections at the glass-air face, and x-rays; they are particularly troublesome because true current densities may vary by as much as a factor of 10^4 at neighboring emission pattern areas, as will appear in the following.

When Eq. (20) has thus been established, field emission furnishes a convenient method for the determination of work functions, requiring the same precautions as before with regard to uncertainties in local values of β . Although at the present absolute values of β are insufficiently well known to yield absolute values of ϕ accurately from Eq. (20), precise relative values of ϕ can be derived therefrom when one value of α can be associated with a known value of ϕ .

Revised measurement of ϕ_{110} was obtained (33) for tungsten by an improved photometric analysis of the field-emission pattern which was developed for the special purpose of obtaining the current-density distribution for the entire emitting area from data obtained during a single microsecond pulse of emission at very large current densities, as is described in Section III,2. Calibrated photographic emulsions were used to record and store the entire pattern data for later analysis. Use of a metal-

backed willemite phosphor and an optically absorbent coating on external glass surfaces increased the observed current density ratios J_{310}/J_{110} from 30, as reported by Wilkinson, to 1600, yielding values of ϕ_{110} in the range $5.0 < \phi_{110} < 5.5$ ev for several cathodes. The authors pointed out that these values probably represented a lower limit on ϕ_{110} , since the experimental method would considerably reduce but not necessarily remove the spurious effects noted above.

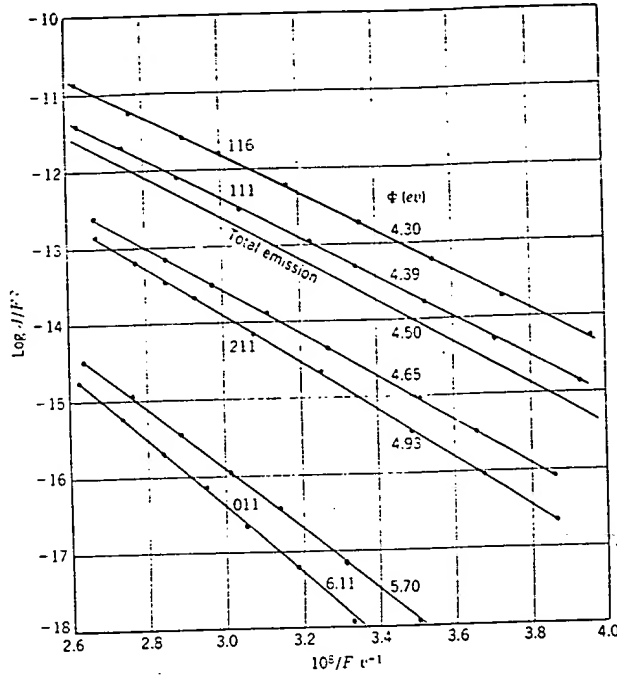


FIG. 16. Experimental graphs showing the current-density electric field relationship for various crystal faces of the clean tungsten monocrystal. [Permission of E. W. Müller and the American Institute of Physics (31).]

Accurate values of J_{110} have recently been obtained by two methods which reduce the pattern contrast at a suitable current collector, thereby avoiding the troublesome spurious effects noted above at higher contrasts. Müller (31), in an improvement of his earlier method (15), used a field-emission microscope with a probe which collected the current transmitted through a small anode aperture from a single face of the cathode crystal. A rotation of the electrodes permitted collection from several crystal faces, though by chance not the (100). Trolan *et al.* (44) reduced the pattern contrast through space-charge effects (see Section III,4), and were then able to observe accurately the distribution of J in the vicinity

of the (110) face by use of the photometric technique; pulse electronic measurements were used at fields about 7×10^7 v/cm for both the cold and the simultaneously heated cathode. Trolan's method is described in more detail in Section V,6. Results from the two methods appear to have an interesting interrelation noted below.

Müller obtained field-emission data as reproduced in Fig. 16, for several faces of the tungsten monocrystal. In calculating the values of F shown, corrections in β were included for its dependence on polar angle if the crystal face was not located at the emitter apex and for reductions at flats. For the latter, β was reduced 3% at the (110) plane with 5.5-deg half-angle and 0.5% at the (211) plane with 2.5-deg half-angle. Those angles were estimated from the work of Becker (25) and from field-ion microscope measurements (3, 5a). From the measured slopes α of the foregoing graphs, by use of Eq. (20), Müller obtained the values of work function shown in Table III; included for comparison are corresponding recent values from Smith (45) and Hutson (46) by thermionic measurements and from Houston (34) by Wilkinson's photometric method with improvements similar to those of Reference 33.

Houston's values of ϕ are shown in Table III without correction for flats. Using estimated flat sizes from Becker (25), he obtained the corre-

TABLE III. Work Functions of Tungsten Crystal Planes

Plane	Field emission at $T = 300^\circ\text{K}$		Thermionic emission $1500\text{--}2000^\circ\text{K}$	
	Müller	Houston †	Smith	Hutson
(116)	4.30	4.26	4.29	$4.20\text{--}4.31 + (3 \times 10^{-6})T$
(013)	4.31	4.35		
(012)	4.34			
(122)	4.35			
(111)	4.39	4.38*	4.38	$4.30 + (3 \times 10^{-6})T$
(233)	4.46			
(123)	4.52			
(112)	4.65-4.88	4.91	4.65	$\begin{cases} 4.57 - (5 \times 10^{-6})T \\ \text{or} \\ 4.66 - (8 \times 10^{-6})T \end{cases}$
(011)	5.70-5.99	5.5‡	5.29‡	5.09 (at 2000°K)
(100)	...	4.71	4.52	$4.44 - (2 \times 10^{-6})T$
Total:	4.50*	4.39		

* Assumed reference value.

† Measured after the cathode was flashed at 2400°K .

‡ Estimated.

sponding corrections in β from electrolytic trough measurements using enlarged models of the emitter tip. Those corrections, which are shown in Table IV, are somewhat larger than Müller's, and if correct, bring into closer agreement the thermionic and field-emission values of ϕ shown in Table III.

TABLE IV

Plane	Flat half-angle in degrees*	$\Delta\phi$ ev
(100)	2.5	-0.12
(112)	3.8	-0.18
(110)	14.5	-0.71

* Measured after 2400° K flash; major and minor axes averaged in the case of elliptical planes.

Hutson (46) made the significant suggestion that the spread in values for ϕ_{110} was due to differences in the heat-treatment of the crystals. Müller (31) found that the values of ϕ_{112} and ϕ_{110} depended on the temperature to which the cathode was annealed before the measurement; his data are reproduced in Fig. 17. In part, Müller attributed this effect to a known increase in flat size during annealing at intermediate temperatures (25); the ion microscope revealed (5a) increases in half-angle from 5.5 to 7 deg at the (110) plane and from 2.5 to 4.5 deg at the (112) plane when the annealing temperature was lowered from 2200 to 1200° C. In part, it was thought that the dynamic disorder of the heated surface was retained as surface roughness after cooling, the decrease in work function due to roughness being well known (40). In particular, the random location of lattice edges and individual atoms on the outermost planes were suggested causes of variable roughness.

These effects are clearly seen from the work of Trolan *et al.* (44) in Fig. 36 of Section V,6, which reveals the current-density distribution in the vicinity of the (110) plane as its outermost lattice plane dissolves at high temperature through surface migration. The following features are revealed: first, current density is lowest on the top atomic plane and in general decreases with increasing plane radius; second, current density increases appreciably at the first lattice edge, which is proven to have atomic dimension; third, current density is larger just outside the top atom plane than it is on that plane, presumably because of isolated atoms on top of the second plane being freed from the edge of the first plane.

Although Trolan observed current-density increases at certain surface roughness that was proven to be of atomic dimension, it is not clear that the increase should be attributed entirely to work function, as Müller

does in Fig. 17. While it appears reasonable to assign those increases in part to a decrease in work function, in part it may be due to localized increases in β . An interpretation of these current-density increases apparently requires an understanding of the field-emission process at lattice steps of atomic dimension, possibly at single atom sites, about which little is presently known.

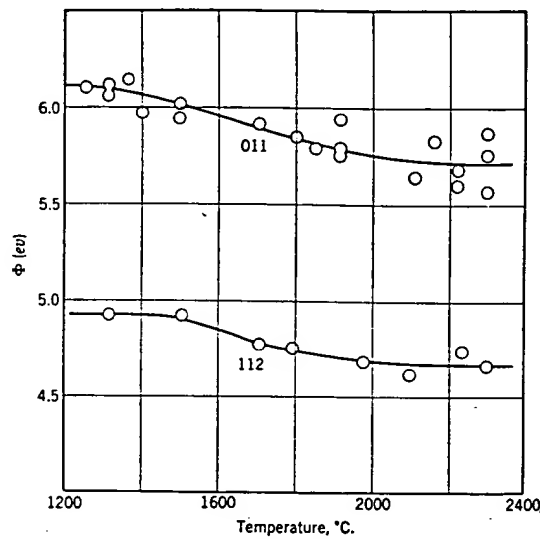


FIG. 17. Work function of (011) and (112) planes as a function of the temperature at which the cathode was annealed before the measurement. [Permission of E. W. Müller and the American Institute of Physics (31).]

The work function of a metal may be measured by a distinctly different method when the metal is used as a collector for field-emission electrons. Henderson *et al.* (47-49b) introduced the method and made preliminary measurements on the work functions of copper, platinum, and nickel, using coaxial cylinders as electrodes. A spherically concentric electrode arrangement was used (42, 50) to measure the work functions of nickel, silver, and copper; with the same method, Müller (15) observed that the work function of a freshly evaporated molybdenum layer increased from 4.57 to 6.8 ev as the result of oxygen adsorption. The method is understood from Fig. 18, which shows the potential diagram at the surfaces of the cathode and collector, between which an anode is placed at high positive potential. Electrons emitted from the cathode by barrier transmission in the energy range W_p , cannot penetrate the thick collector barrier; hence, collection occurs only if the collector is positive relative to the cathode by an amount $V_c = \phi_c$, where ϕ_c is the collector

work function. The solid lines show the potential diagram for $V_c = 0$, the dashed lines for $V_c = \phi_c$. The accuracy of the method depends on the relatively sharp cut-off of the energy distribution, no electrons appearing at energies above the top Fermi level for the cold cathode.

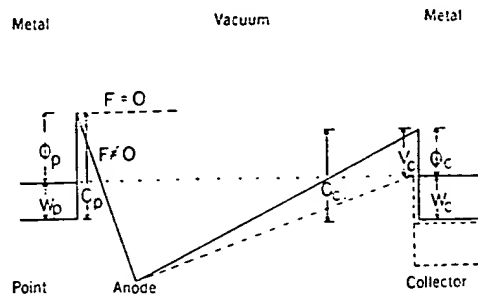


FIG. 18. Diagram of potential between point cathode, screen anode, and collector; electrons tunneling the thin cathode barrier at the top Fermi level F_p must go over the thick collector barrier, collection therefore occurring when $V_c = \phi_c$ (dashed lines), where ϕ is work function.

6. The Distribution in Energy of Field-Emission Electrons

In one of the more important field-emission experiments, Müller (42) and Henderson and Dahlstrom (14) verified two features of the energy distribution curves for the cold cathode shown in Fig. 3, namely, that the emission is restricted to electron energy levels below the top Fermi level ($\epsilon = 0$), and that the maximum of the distribution curve occurs at the order of a volt below that level. This observation supported the hypothesis of the wave-mechanical tunnel effect, in which electrons are transmitted through the thinned potential barrier, rather than over it. It also supported the validity of the then relatively new Fermi-Dirac electron supply function, Eq. (1), and the barrier transmission coefficient, Eq. (2). It added strength to the proposal that no energy need be added to the cathode to cause field emission. A practical significance of the latter is that field emission avoids problems associated with conventional cathode energy sources, such as batteries or filament transformers, which add weight and expense and difficulties with heat dissipation and electrical insulation.

In order to measure experimentally the energy distribution among field electrons, Henderson and Dahlstrom applied the counter potential method which Goss (47) and others used later to measure collector work functions, as was described in Section III,5. According to Fig. 18, electrons emitted at the top Fermi level are collected at the threshold potential $V_c = \phi_c$. Further increases in V_c effect the collection of all electrons

emitted above a corresponding cathode energy level; hence, the derivative with respect to V_e of the curve of collector current vs V_e is plotted as a graph in the form of the energy distribution curves of Fig. 3.

In disagreement with theory, they found more electrons at low energy than predicted and correctly attributed part of the cause to a low-energy current of secondary electrons and to end effects associated with their cylindrical electrode arrangement. From their published electric field values one can infer that field emission originated primarily from surface roughness on their fine wire cathode. Richter (17) suggested that under such conditions an appreciable fraction of the total electron energy acquired in transit would be associated with transverse velocity, which

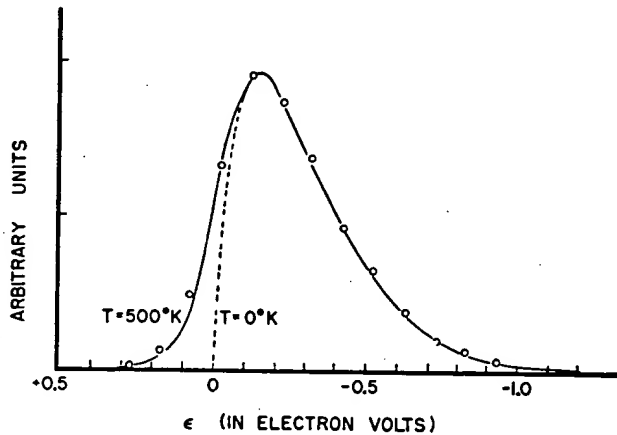


FIG. 19. Calculated distribution of electron energies (solid curve) for $F = 3.5 \times 10^7$ v/cm and $T = 0^\circ\text{K}$, 500°K , together with measured values (adapted from Müller in notation of the present text).

would account for the observed "tails" on the experimental distribution curves. He also derived energy distribution curves for both the transverse and normal velocity components for emission at the plane surface. Müller (15) remeasured the distribution curves with the following experimental improvements: a field-emission microscope with a clean, smooth cathode surface; a concentric spherical electrode arrangement with collected emission restricted to a small solid angle, resulting in a reduction of end effects as well as of errors due to transverse velocity; a collector of uniform work function; selection of emission from any of several crystal faces at the cathode.

Müller obtained the distribution curve shown in Fig. 19, using an experimental electric field value $F = 3.5 \times 10^7$ v/cm. By comparison of that curve with the one shown in column 2, line 2 of Fig. 3, the width of

the distribution is seen to be about 1 ev as expected; however, a "toe" to the curve was observed for $V_c < \phi_c$ which was attributed to thermal electrons corresponding to an estimated cathode temperature of 500° K. Gomer's recently calculated curves (16) are substantially in agreement. The magnitude of similar toes for a copper cathode have been shown to increase with increasing cathode current (50).

The foregoing experiments confirm the predicted energy distribution for low temperature and one value of electric field. No experimental data were found in the literature for the general case of both high temperature and high field described in Fig. 3.

7. Energy Exchanges during Electron Emission at High Fields

A property of field emission already mentioned is that it is not necessary to add energy to the metallic cathode to cause emission; electrons tunnel through the surface potential barrier without gain or loss of energy, according to the wave-mechanical mechanism. This is contrasted to other types of emission in which energy must be added to enable electrons to surmount the normally rectangular barrier.

This property was recently demonstrated in a striking manner by Gomer and Hulm (51) when field emission was obtained in an evacuated tube immersed in liquid helium at 4° K. However, a more quantitative measurement of the energy exchange during electron emission was made earlier by Fleming and Henderson (52), who studied both field emission and thermal emission in the same experimental tube. Temperature changes were measured by observing the thermal electromotive force in a bimetallic junction from which emission currents were drawn. No measurable temperature change was detected for field emission up to thermionic temperatures. The authors concluded that their experiment gave strong support to the hypothesis of the field-emission tunnel effect.

In an exchange of letters (53, 54) concerning the foregoing paper, Nottingham made the interesting suggestion that there should be a heating effect accompanying strong field emission from a cold, sharp cathode, analogous to the well-known cooling effect which accompanies thermal emission. Conditions for heating or cooling during emission may be seen from the energy distribution curves of Fig. 3. When the average emitted electron energy $\bar{\epsilon}$ is positive, cooling results, as in thermal emission; when $\bar{\epsilon}$ is negative, as in field emission, vacated electron energy levels within the metal are replaced by electrons from the conduction level $\epsilon = 0$, the energy difference being imparted to the metal.

Whether or not this energy transfer is experimentally significant depends on its magnitude and proximity to the emission surface, about which there has been some disagreement (53, 54). If it is confined within

the hemispherical tip of a conventional needle-shaped cathode, it may be expected to be important under certain experimental conditions; for example, it may limit the current which can be drawn from a cathode without removing it from the superconducting state.

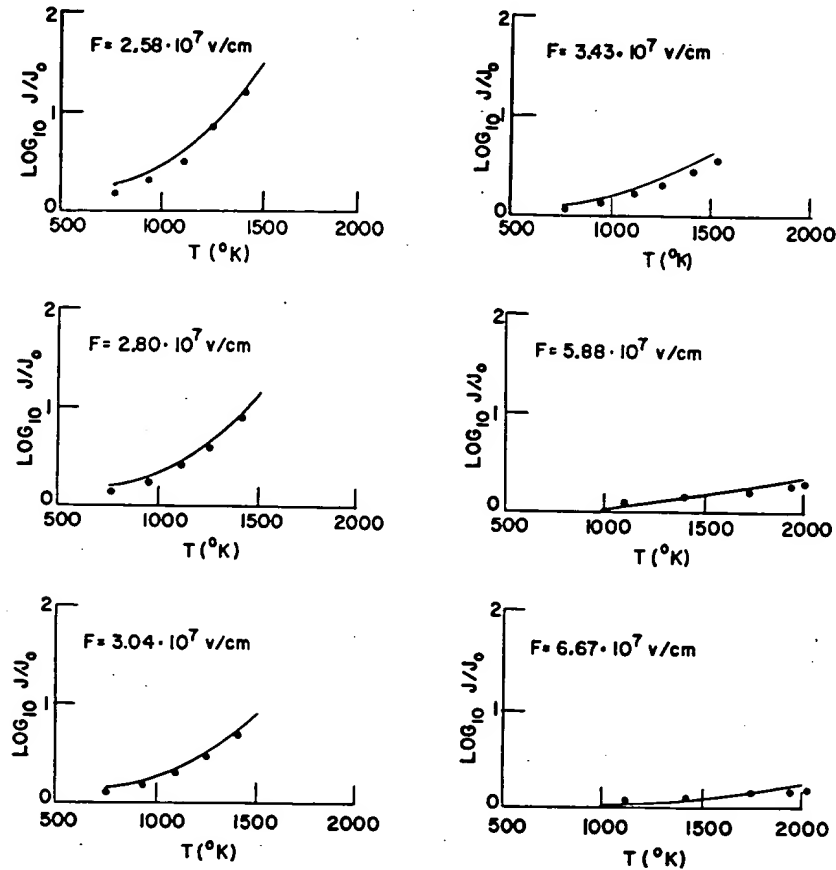


FIG. 20. Calculated values of J/J_0 vs temperature T at several fields (solid curves), and corresponding experimental data from tungsten (circles). J and J_0 are current densities at stated temperature and at room temperature, respectively.

No published experimental confirmation of emission heating has been found. For a discussion of resistive heating at large current densities see Section IV.

8. The Dependence of Current Density on Temperature and Field

Current densities expected from the tungsten cathode for values of the electric field in the range $2 \times 10^7 < F < 10^8 \text{ v/cm}$ and for temperatures

of 0, 1000, 2000, and 3000° K were presented in Fig. 4. One feature of those relationships is that the effect of temperature on field emission is small for temperatures below 1000° K, a fact which was established experimentally at an early date (19, 20). This was used as further evidence for the tunnel effect, since thermal emission over the surface potential barrier is sensitively dependent on temperature.

Early experiments were confined to steady-state operation at relatively low fields and temperatures in order to avoid cathode geometric distortion (see Section V,8). Recently (55), pulse electronic techniques were used to measure experimentally the average current density from the hemispherical tungsten monocrystal in the extended ranges of variables $2.5 \times 10^7 < F < 7 \times 10^7$ v/cm and $300 < T < 2000$ ° K. The comparison between those experiments and the theoretical predictions are reproduced in Fig. 20. The agreement supports the wave-mechanical theory at higher combined values of T and F than previously reported.

IV. THE FIELD-EMISSION INITIATED VACUUM ARC

Electrical breakdown between metallic electrodes in high vacuum is a problem throughout the electronics industry and particularly with high-energy particle accelerators. Many theories have been proposed to account for various observations, e.g., Cranberg's "clump" mechanism (56), the particle exchange processes of Trump and Van de Graaff (57, 58), Germer's (59) enhancement of field emission by anode-formed ions, and self-focusing of electron-ion streams proposed by Bennett (60), to name a few. The diversity of theory reflects the complication of the physical processes which may be involved; a summary of the complete field is beyond the scope of this work.

Experiments are described in which field emission is known to have initiated breakdown in the form of a vacuum arc, the discussion being limited to cases in which sufficiently quantitative measurements permit interpretation of the data in terms of basic concepts. Two experimental conditions will receive particular emphasis. In the first, cathode resistive heating at large field-current densities is an arc-initiating factor, which is important herein, since it sets an upper limit on the current densities which may be drawn for useful purposes from a given cathode. In the second, anode-formed ions enhance the cathode emission leading to a similar breakdown, a case which limits the power density which can be sustained at the anode.

It is interesting to relate the data in Fig. 11 to voltage insulation. A significant observation is that neither field emission nor breakdown is observed for $F < 3 \times 10^7$ v/cm when a clean tungsten cathode is used, a

value of F higher by about two orders of magnitude than those achieved in common electronic practice. At higher fields, the field currents are reproducible, provided that a critical current density is not exceeded; however, an increase in microsecond pulse current density above about $J = 10^8$ amp/cm² leads to a violent, low-impedance vacuum arc which usually deforms the cathode. As a result, β is changed and the original current-voltage relationship is not thereafter reproducible. Electron micrographs of a typical cathode before and after arc are shown in Fig. 21.

Evidence has been presented that the arc can be initiated by resistive heating (28, 61, 62) in the absence of other energy sources. In this case, it appears that space charge is neutralized by ions supplied from the heated cathode surface, thus permitting the large observed current increase.

The presence of a high cathode temperature just prior to such arc initiation is inferred from experiment and predicted by calculation of the temperature rise expected from resistive heating. The tungsten emission pattern undergoes an abrupt change with increasing current density. A bright ring of emission appears around the normal pattern, its emission originating on the cathode neck at polar angles $\theta > 90^\circ$. This increase in emitting area results (61) from $T\text{-}F$ emission when the neck is resistively heated to temperatures exceeding 3000° K. Other experimental evidence includes an increase in current with time, while voltage is constant, which again results from the thermal increase in field-current density. Also, other experiments have shown that barium is evaporated from the tungsten tip at the critical current density, an effect which cannot be attributed to field stripping which occurs only at fields large compared with the value $F = 7 \times 10^7$ v/cm used here (3).

A mathematical analysis of the resistive generation of heat and its simultaneous dissipation by conduction was made (62) using values of the physical constants for the polycrystalline metal which were valid at intermediate temperatures, and cathode geometry from typical electron micrographs as in Fig. 22. For mathematical purposes, the geometry was approximated as a cone bounded by concentric spherical surfaces, in which both heat flow and current lines were assumed to be radial. Heat radiation was assumed negligible.

For a typical cathode cone angle of 11 deg, the maximum steady-state

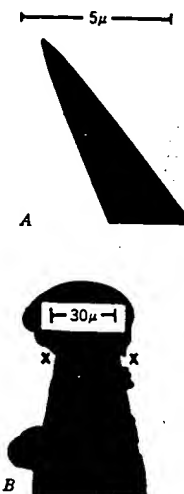


FIG. 21. Electron micrographs of a typical tungsten emitter (a) before use and (b) after vacuum arc.

temperature, which occurs at the emitter tip, may be expressed by the relation

$$T_{\max} = 9.5 \times 10^{-4} J^2 r^2 {}^\circ\text{C} \quad (21)$$

where J is current density in amp/cm², and r is emitter radius in cm. If T_{\max} is to be held at less than 1000° C, an arbitrary value used for illustration, it is clear that the product $J^2 r^2$ must not exceed about 10⁶. Thus, in the range of radii from 10⁻⁴ to 10⁻⁵ cm, J for direct-current operation may reach corresponding values of 10⁷ to 10⁸ amp/cm² under the conditions here described. It should be noted that while the permissible J varies inversely with the radius, the total current involves emitting area and so varies directly with the radius.

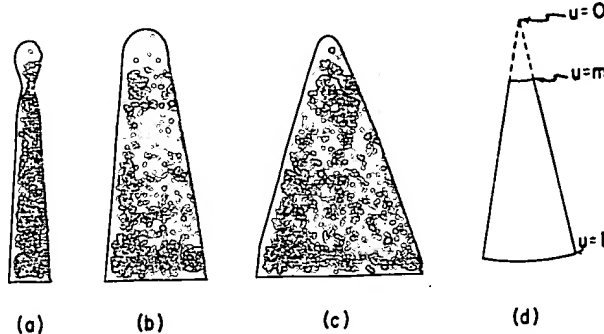


FIG. 22. A comparison between the geometry of typical field emitters (a,b,c) and the idealized conical geometry (d) used in the calculation of resistive heating and its dissipation by conduction.

The temperature rise time is such that the steady state is closely approached in 10⁻⁵ sec, and about one-fourth of the temperature increase is to be expected in a microsecond. Since T is proportional to J^2 , microsecond operation should permit about twice as large a current density as can be sustained in the steady state, and shorter pulses offer the possibility of attaining still higher levels.

For the cylindrical cathode, a similar calculation using the appropriate geometric approximation yields

$$T_{\max} = 2.45 \times 10^{-7} J^2 {}^\circ\text{C} \quad (22)$$

which may be compared with Eq. (21) for the cone. The temperature in the present case is independent of radius.

Equation (22) immediately gives a limiting value of J of about 10⁵ amp/cm² for operation at 1000° C in the steady state, which is a factor of several hundred less than the level permitted by conical emitters of typical radius. Although the temperature in conical emitters is not very

sensitive to changes in cone angle within the stated limits, the change is very rapid as the angle approaches zero, and it may be shown that Eq. (22) is the limit of Eq. (21) under such conditions.

A comparison of temperature gradients for the cylindrical and conical cases in the steady state is instructive. Figure 23 shows such a comparison, with the dotted curves indicating the corresponding temperature distributions if heat conduction is neglected. The latter curves reach no

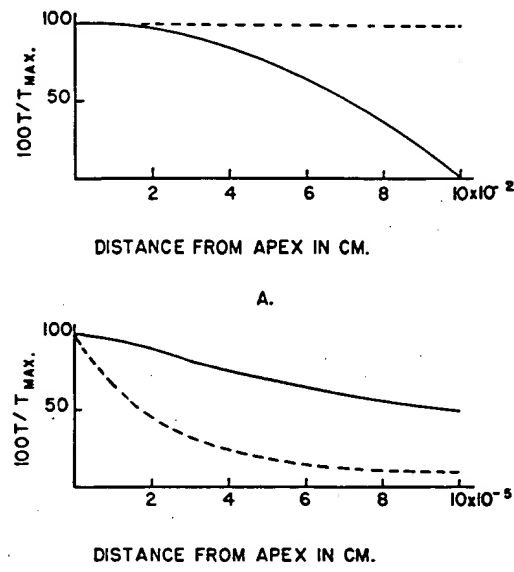


FIG. 23. A comparison between steady-state temperature distributions (solid curves) in the idealized field emitters of (a) cylindrical and (b) conical geometries, the latter assuming a tip radius of 10^{-6} cm. Dotted curves are corresponding distributions if heat conduction is neglected, adjusted to arbitrary maxima.

steady state and are arbitrarily adjusted to the same maxima. It is observed that while the temperature in the conical case decreases to one-half of its maximum in a distance of 10 emitter radii from the apex, the same fraction is reached for the cylinder at a distance of several thousand radii.

The largest current densities that have been drawn from an entire tungsten needle tip are 10^6 amp/cm² using direct current (28, 36) and 4×10^8 amp/cm² using microsecond emission (28); current densities of the order 10^8 amp/cm² have been drawn from small portions of the cathode surface using direct-current techniques (63).

The agreement between the experimental pre-arc field current density \bar{J}_z and the calculated value J_R for which T reaches 3000°C in $1\ \mu\text{sec}$, as shown in Table V, provides strong evidence that resistive heating was an arc-initiating mechanism in these experiments. On the other hand, initiation was not dependent on applied voltage, as Table V illustrates. A voltage effect has been reported under other conditions (57).

TABLE V. A comparison between observed experimental current densities J_z required to initiate arc for several emitters (Column B) and calculated current densities J_R (Column C) for which the calculated temperature reaches 3000°C in the corresponding pulse times.

A Emitter number	B J_z (amp/cm ²)	C J_R (amp/cm ²)	D V_{\max} (kv)	E Radius of the emitter tip (cm)	F Half- angle of the emitter cone (deg)	G Pulse length (μsec)	H* Tube type, electrode spacing (cm), anode material
O-3S	6×10^7	7.0×10^7	9.2	2.4×10^{-5}	5	1	S, 4.5, ABW
X-62†	4×10^7	2.4×10^7	8.8		10	$\frac{1}{2}$	S, 8.5, ABW
X-62-A	3×10^7	2.5×10^7	60.1	1.5×10^{-4}	10	1	S, 8.5, ABW
Q-1	4×10^7	7.1×10^7	4.9	1.5×10^{-5}	3	1	PTP, 1, Moly.
Q-29	7×10^7	7.4×10^7	14.2	3.2×10^{-5}	6	1	S, 8.5, ABW
O-54	1×10^8	2.7×10^8	16.1	2.0×10^{-5}	16	1	S, 4.5, ABW
2-X-4	5×10^7	5.8×10^7	13.3	3.8×10^{-5}	6	1	S, 4.5, ABW

* Experimental tube type S is shown in Fig. 1 of reference 61; type PTP, point-to-plane; ABW, aluminum-backed willemite.

† Electron micrographs of this emitter were not available; hence \bar{J}_z was calculated from its electrical behavior with the aid of Eq. (5). In this case, \bar{J}_z was known within a factor of 3. For the other emitters, electron micrographs were available and \bar{J}_z was known within ± 10 per cent.

It was found that the value of \bar{J}_z decreases with increasing resistivity as expected. For this purpose, microsecond emission was drawn from tantalum, and from platinum whose resistivity is said to increase rapidly (64) with current densities above 10^6 amp/cm². Further increases in \bar{J}_z through use of shorter current-pulse durations have been demonstrated; the comparison of such data with the foregoing theory is in-progress.

In the foregoing work, breakdown involved primarily cathode mechanisms; to illustrate the case in which anode formed ions are influential, we turn to the work of Germer and his group, who have investigated electrical breakdown at very short gap spacings during electrode closure. An interesting early observation (59) was that field currents initiated breakdown just prior to closure, contrary to the accepted theory that an

arc developed upon contact of small surface irregularities. There followed an excellent series of papers (65-70), which led to a recent one (71) in which currents preceding breakdown have been measured between closely spaced tungsten electrodes in high vacuum. The arc-initiating current was found to follow Eq. (5) when β was estimated at surface irregularities, which established the current source as field emission.

Breakdown occurred for gap spacings less than 8×10^{-4} cm at voltages less than 2.2 kv. It was shown that field currents evaporate metal

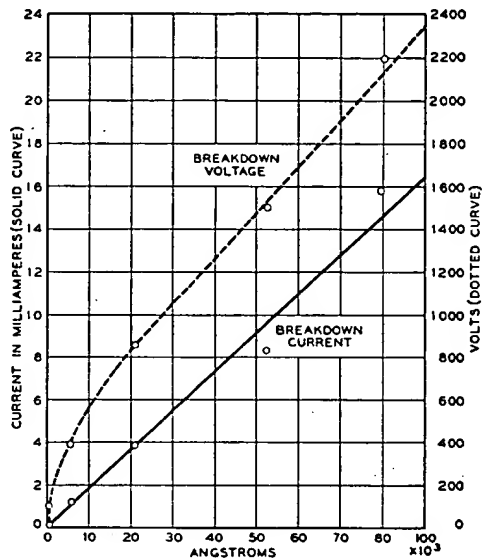


FIG. 24. Maximum prebreakdown current (—) and breakdown voltage (----) vs electrode spacing. [Permission of Boyle, Kisliuk, and Germer and the American Institute of Physics (71).]

from the anode and that breakdown occurs in the resulting vapor. Experimentally, the maximum prebreakdown current increases linearly with gap spacing, as does the voltage, approximately as in Fig. 24. It follows, if one assumes linear spreading in the electron beam, that some critical power density at the anode determines the point of arc initiation. The pressure p_1 of evaporated metal at the anode, assuming a small heated area and heat dissipation by both conduction and evaporation, is given by

$$p_1 = P_E / [3.5\sigma\rho^2(m/RT_B)^{1/2}] \quad (23)$$

where R is the gas constant, T_B the boiling temperature, ρ the radius of the heated anode disk, P_E the input power, σ the energy necessary to evaporate 1 g, and m the atomic mass. In an example of break-

down at 2 kv, with a gap spacing 7.5×10^{-4} cm, $P_E = 26$ w. With an assumed beam spreading of 20 deg, it follows that $\rho = 2.7 \times 10^{-4}$ cm and the authors calculate "a pressure p_1 of 670 atmospheres at the boiling point, or a density about 35 times that at NTP." While the latter renders the assumed 20-deg electron spreading invalid as they point out, it leaves certain the presence of a large prebreakdown vapor density.

To account for breakdown, it is necessary to account for a high yield of electrons at the cathode per positive ion created in the gap. The authors assume that the collective space charge of ions enhances the cathode field, and hence its electron current density; they calculate that breakdown will occur when the current density is thereby increased by a factor of 1.65. This certainly appears to be a sufficient condition; however, the authors did not mention the possibility that an arc could be initiated by resistive heating when the cathode surface was altered locally by the incidence of a few anode ions (or atoms). Effects due to cathode bombardment by helium ions are reported in Section VI,1; also, Müller (72) has proposed one possible mechanism whereby incident particles can cause large localized increases in current density.

V. FIELD-EMISSION MICROSCOPY

1. Introduction

The field-emission projection microscope was first described in spherical symmetry by Müller in 1937 (68), after the principle had been demonstrated in cylindrical form by Johnson and Shockley (73) using thermionic emission. It has proved to be an invaluable instrument not only for its contribution to the understanding of field emission itself but also as a device for studying surface phenomena not previously available to direct observation.

Conventional methods of optical and electron microscopy reveal details on a metal surface of the relatively large scale associated with grain structure, whereas the field-emission microscope extends observations down to molecular and atomic surface irregularities, and is particularly sensitive to monoatomic adsorbed layers. X-ray methods have provided a wealth of knowledge about the structure of the interior of crystals; however, those methods are less useful in studying phenomena at the surface layer, such as adsorption, desorption, migration, and chemical reactions, to which the field emission microscope is often ideally suited. Electron diffraction methods disclose the structure to within about 10 atom layers but are less successful in revealing detail in thinner surface layers.

The essential features of the field-emission microscope, illustrated

schematically in Fig. 25, consist of a cathode in the form of a needle with a hemispherical tip, mounted opposite a luminescent screen. Electrons emitted from the cathode follow nearly radial trajectories to the screen, where the light output from the phosphor provides a visual pattern corresponding to the distribution and intensity of emission at the cathode. The exponential sensitivity of cathode current density to both electric field and work function means that variations in the pattern (either from place to place or from time to time) may be interpreted as due to variations in one or both of these parameters. The interpretation of such emission patterns is the subject matter of field-emission microscopy.

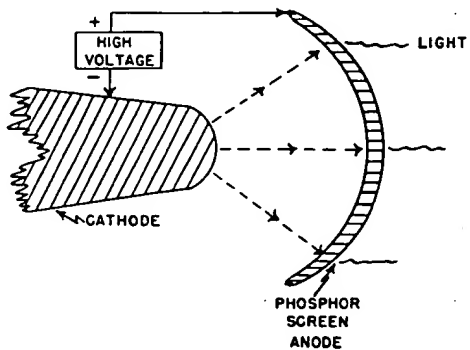


FIG. 25. Schematic of field-emission microscope; electrons from cathode (dashed arrows) diverge toward anode on which enlarged cathode emission pattern is viewed.

Ashworth has summarized field emission microscopy in Vol. III of this series (3a); earlier work has also been reviewed recently by Jenkins (2) and Müller (3). Moreover, there are new summaries by Müller (in *Handbuch der Physik*, 1956), Becker (in *Advances in Catalysis*, Vol. VII, 1955) and Gomer (also in *Advances in Catalysis*, Vol. VII, 1955). The published work in this field is much too large to be covered here; much of it is descriptive and therefore difficult to interpret with assurance. For these reasons no attempt will be made here to resurvey the complete field, but rather to review the experimental method briefly and then to consider a few developments, mostly recent, which are believed to be significant. In general, the more quantitative work is given preference.

2. Magnification and Resolving Power

It is clear from Fig. 25 that the magnification of the instrument is approximately the ratio of electrode separation to emitter radius, though the trajectories usually depart from the radial directions enough to reduce the magnification by a factor of about 2. For a typical emitter radius of

5×10^{-5} cm and a screen spacing of 5 cm, one obtains a magnification of about 10^5 .

A more exact calculation of the magnification requires consideration of the actual electron trajectories, which are influenced by the emitter shank geometry through its effect on the equipotential surfaces surrounding the emitter tip. Rose (74) has calculated exactly the magnification for the case where the emitter is idealized as a smooth paraboloid of radius of curvature r at the vertex and the screen as a confocal paraboloid at distance R ; he finds that the magnification is given by the relation

$$M = \frac{\Gamma(\frac{1}{2})}{\Gamma(\frac{1}{4})} \left(\frac{2R}{r} \right) \left(\ln \frac{2R}{r} \right)^{-\frac{1}{4}} \left[1 + \frac{1}{8 \ln(2R/r)} + \dots \right] \quad (24)$$

For most purposes this can be approximated as

$$M = \frac{1}{x} \cdot \frac{R}{r} \quad (25)$$

where the factor x lies in the range $1.5 < x < 2.0$ for various typical experimental conditions. The value of x is measurable in terms of the position on the screen of the known crystallographic directions of the clean cathode.

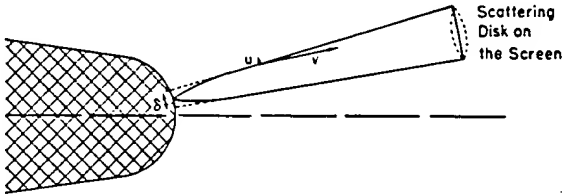


FIG. 26. Scattering disk at phosphor screen from a point source of apparent diameter δ on field emitter's surface; V is radial velocity, μ is transverse velocity of electron in transit (adapted from Müller).

In spite of the very small emitting area, current densities as great as 10^8 amp/cm² provide sufficient light at the phosphor in times as short as 1 μ sec (28) to permit photographic exposures of the emission pattern; motion pictures may also be taken (75).

Müller (76) observed that the pattern on the screen was not exactly sharp, because electrons emitted from any point on the cathode surface have a small tangential velocity component u associated with an energy of about 0.5 ev, which results in a scattering disk on the screen, Fig. 26. In calculating the value of the effective source diameter δ , Müller recognized contributions from diffraction as well as from the tangential velocity component. When the two contributions to δ were combined quad-

ratically, he obtained the approximate expression

$$\delta = \left[\frac{5.35 \times 10^{-8}r}{\phi^{3/2} \ln(4R/r)} + \frac{11.5r^{3/2}}{\phi^{3/2}} \right]^{1/2} \quad (26)$$

Gomer (16) has recently calculated δ , recognizing contributions to the transverse velocity both from transverse components in the Fermi electrons within the metal and from considerations involving the uncertainty principle. From the former alone, he deduced the result

$$\delta = 1.31 \times 10^{-4} \chi [\beta/f(y) \phi^{3/2}]^{1/2} \quad (27)$$

where χ has the same significance as in Eq. (25) and the other variables have been written in the notation of the present paper. Equation (27) yielded a resolving power of about 30 Å for $r = 3 \times 10^{-5}$ cm. While Müller combined the effects of tangential electron velocity and diffraction to get Eq. (26), Gomer neglected uncertainty considerations in deriving Eq. (27) after reasoning that their effect would be slight for the smooth cathode of typical size.

Gomer noted that the transverse velocity v_1 imposed by the uncertainty principle was, in the case of a source size Δx ,

$$v_1 = \frac{\hbar}{2m\Delta x} \quad (28)$$

For a source diameter greater than about 25 Å, the transverse velocity from Eq. (28) is negligible compared with that used in deriving in Eq. (27); therefore, for the typical smooth cathode, the uncertainty principle does not play an important role.

The resolution is improved at irregular projections on the cathode surface. For small objects placed thereon on such projections (e.g., Fig. 27), the lateral velocity arising from uncertainty considerations is greater than that transmitted from the Fermi sea. Rose (74) has pointed out that in such regions the resolution is determined by the magnification and the uncertainty principle. Large current density originates at such sites because of increased electric field and reduced work function. When the transverse velocities Δv_0 from the Fermi sea and v_1 from Eq. (28) are combined, Rose finds for δ

$$\delta = \left(\frac{2\hbar T}{mM} \right)^{1/2} \left[1 + \frac{2mT(\Delta V_0)^2}{\hbar m} \right]^{1/2} \quad (29)$$

where M is the magnification as in Eq. (24) and T is the time of flight given by $T \approx R/(2eV/m)^{1/2}$.

Rose concludes from Eq. (29) that neighboring objects of atomic scale may be resolved if they are suitably located on surface projections. In that case, one must have $\delta \approx 3 \text{ \AA}$, which follows from Eq. (29)

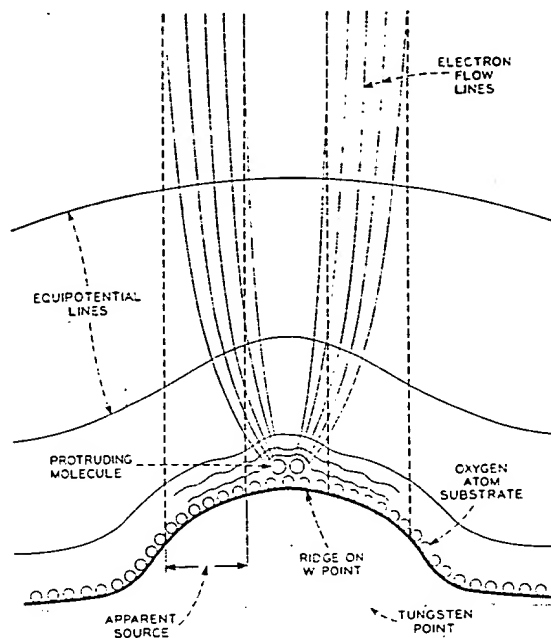


FIG. 27. Schematic equipotential and electron-flow lines near an oxygen molecule adsorbed on a substrate of chemisorbed oxygen atoms. (Permission of J. A. Becker.)

if $M \approx 5 \times 10^6$, an increase of a factor of about 20 over the normal value. For this condition Eq. (29) reduces to

$$\delta = \left(\frac{2hT}{mM} \right)^{1/2} \quad (30)$$

Rose finds that adequate magnification is expected if the size of the surface irregularity lies between 5.5 and 40 \AA . This finding tends to support the proposals in Section V,4 concerning the visibility of single atomic or molecular emission sites.

Ashworth (3a) calculated resolving power independently in Vol. III of this series. His interest was directed particularly toward the case of a very small emitter, of estimated radius $5 \times 10^{-7} \text{ cm}$, where his results indicated a possible resolution of 2 \AA . When the differences in geometric scale of their examples are taken into account, the four authors cited are in reasonably good agreement.

3. Emission from Clean Metals

The fundamental character of a field-emission pattern is determined by the crystal structure of the emitter metal. Müller observed (63) that a tungsten emitter, immediately after flashing to high temperature in good vacuum, displayed a characteristic pattern readily correlated with the body-centered cubic crystal structure, so that the Miller indexes of the various crystal surfaces served as a system of reference for observations. Furthermore, any change in the pattern through surface contamination could usually be removed and the basic pattern restored by a high-temperature flash. In tungsten at least, the usual grain size in the emitter

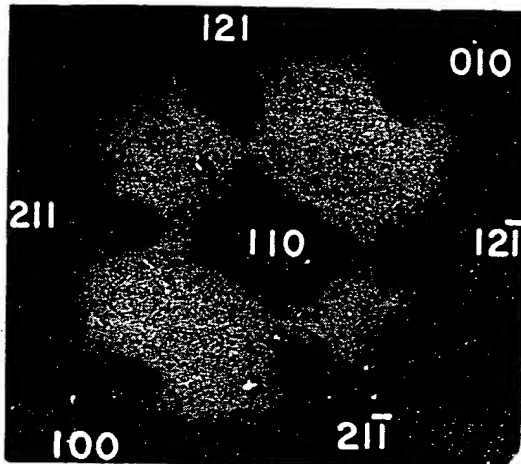
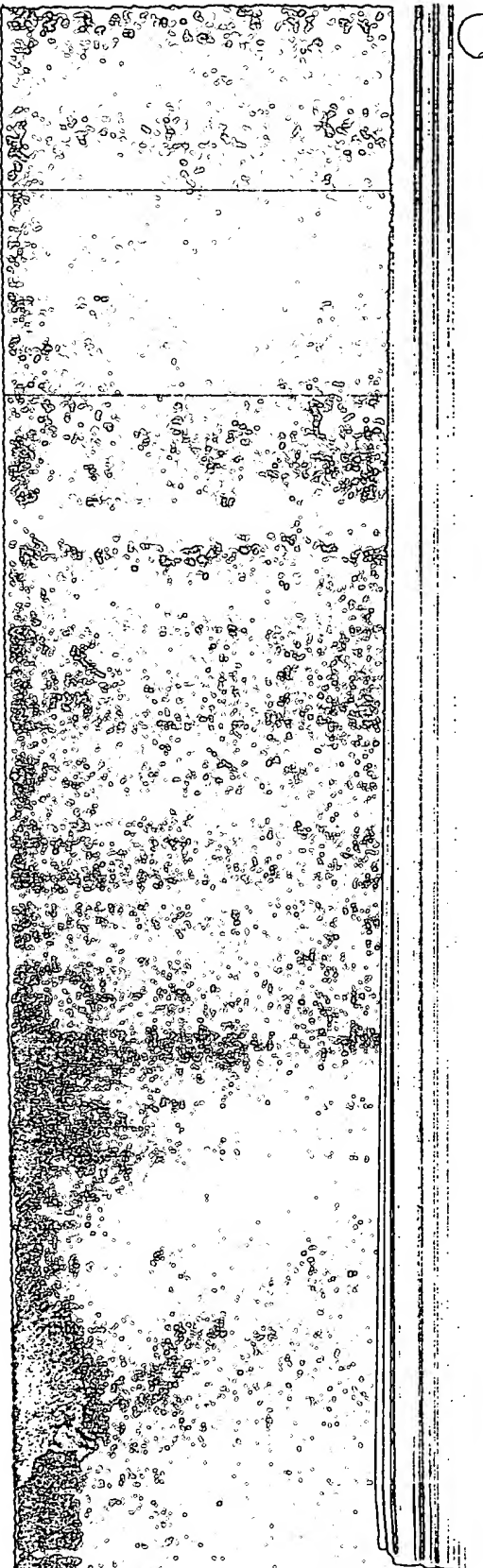


FIG. 28. Emission pattern from tungsten cathode. Bright areas correspond to dense electron emission; dark areas show weak emission and are labeled with corresponding Miller crystallographic indexes.

wire stock is enough larger than the final emitter tip so that in most cases the latter is etched from a single crystal. A typical clean tungsten pattern with indexes marked on the principal surfaces is shown in Fig. 28. As in this example, the (110) direction is usually parallel to the wire axis. An orthographic projection of the crystal faces on the tungsten hemisphere is shown in Fig. 29; individual crystallographic directions may be compared in the two figures.

An idealized representation of the surface detail for a tungsten emitter is presented by the model (suggested by J. A. Becker) shown in Fig. 30, where marbles representing the atoms have been fitted as closely to a spherical surface as the body-centered cubic structure would allow. To correlate the model with the pattern of Fig. 28 requires a change of



orientation, since it was not convenient to build the model with the (110) crystal face at the center as it appears in the emission pattern. It is evident that the smooth, closely packed (110) plane is associated with the dark central area of the pattern, that the somewhat less dense and more

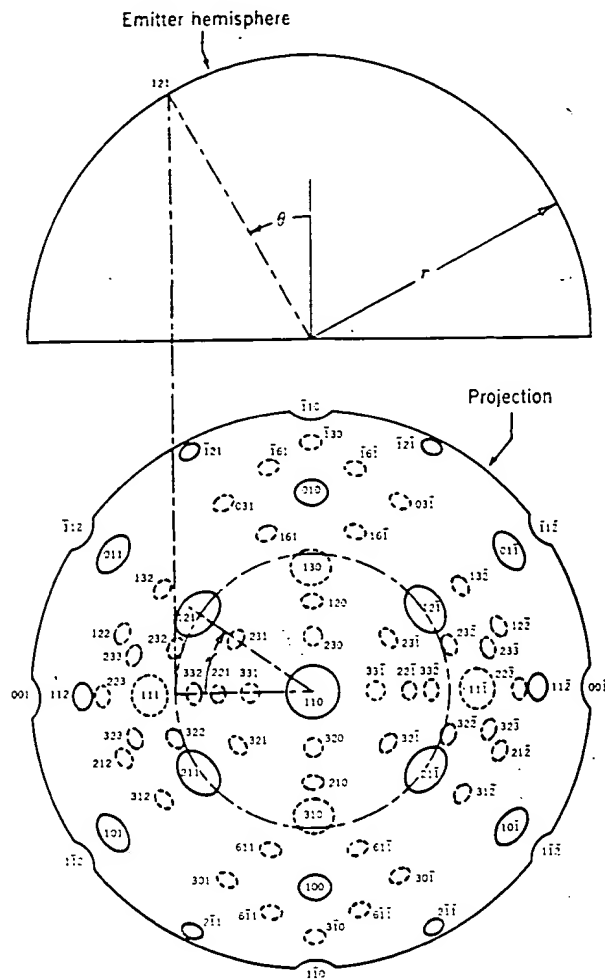


FIG. 29. Orthographic projection of hemispherical tungsten cathode surface.

rough (211) and (100) planes correspond to the smaller dark spots, and that the rough (611), (111), and (310) areas are represented on the pattern by areas of intense emission.

The black, gray, and white marbles have the following significances: a black marble touches four other marbles, i.e., the corresponding atom

has four nearest neighbor bonds; a gray marble has five nearest neighbors; a white marble has six nearest neighbors if on a surface and eight if in the deep interior. The bonding of tungsten surface atoms is important, because the fewer the near-neighbor bonds, the more bonds the atom can make with adsorbates; the fewer the bonds, generally speaking, the rougher is the emitting surface, and surface roughness enhances field

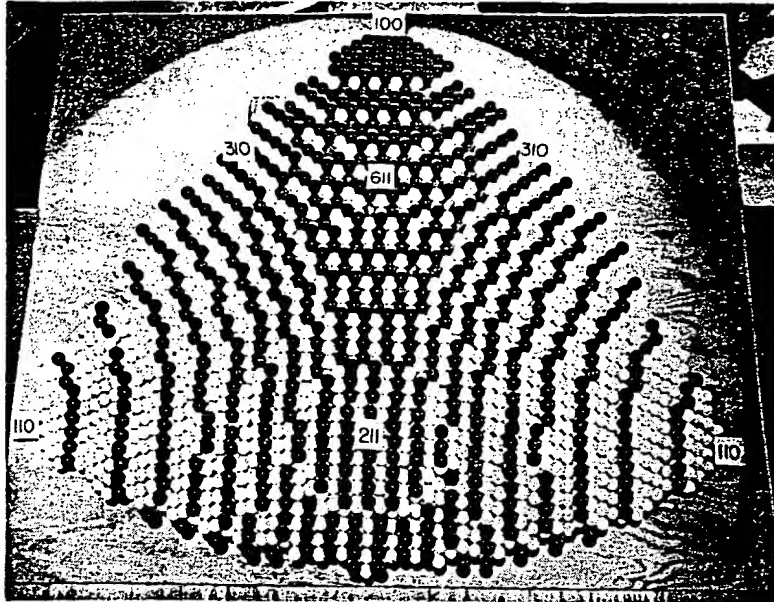


FIG. 30. "Marbles-for-atoms" model of a portion of a hemispherical tungsten field emitter, with several crystal faces identified with Miller indexes; surface radius of 50 atoms is about one-twentieth that of a typical emitter.

emission by both increasing β and decreasing ϕ . As a result, the structural detail of the surface of the marble model in Fig. 30 is closely related to both the electron emission pattern and the behavior of various adsorbates.

Another characteristic of the model is that the crystal faces of low indexes are planes of extended area. The (110) plane is of particular interest. It is the largest and most densely packed, having 1.4×10^{15} atoms/cm² for tungsten; it has the least field-current density of all faces, corresponding to the highest work function (Section III,5); its extended area or "flat" causes a localized decrease in β as was also noted in Section III,5; its edge atoms, black and gray, are less tightly bound and are therefore more readily lost through surface migration at elevated temperatures, resulting in a decrease of plane area noted in Section V,6; the

same edge atoms have unsatisfied bonds which suggests that these sites will be especially active in adsorption, in agreement with the observation that adsorbates often tend to collect at the edges of the (110) plane; electron emission is locally enhanced by surface roughness at the edge atoms of the (110) plane, as is shown in Section V,6. For these and similar reasons, a model of the type in Fig. 30 is most helpful in interpreting field-emission data.

The work function variation at the different crystal faces, together with the variation of electric field over the surface, is responsible for the distribution of emission intensity as has been discussed in Sections III,2 and III,5. Müller (15) showed that it was impossible to account for the low emission at several faces through destructive interference of free electron waves at lattice planes within the crystal.

Metals other than tungsten have not received comparable quantitative study, but many of them have been tried as field-emission sources. When it was possible to obtain clean surfaces, the patterns revealed a similar relationship to crystal structure to that observed for tungsten, with the close-packed surfaces yielding the least emission. Obtaining a clean surface, however, is not a simple process for any but the more refractory metals, since contaminants are often bound more tightly than the atoms of the substrate; hence, use of a high-temperature flash may alter cathode geometry without effecting the desired surface cleanliness. Even a tungsten surface may not be readily cleaned of some contaminants by high-temperature flashing; carbon, for example, may be very difficult to remove. The surface may be cleaned by chemical methods, e.g., reduction in a hydrogen atmosphere (72), or by vacuum-casting the cathode tip when it is melted during a vacuum arc and recrystallized in a few microseconds (Section IV); it may also be cleaned by field desorption (Section V,5).

Tantalum and molybdenum have sufficiently high melting points to serve satisfactorily as emitter materials, and their patterns are similar to that of tungsten, since the metals have the same crystal structure (51, 63, 77, 78). Nickel has been carefully studied by Gomer (79), who was able to clean the metal successfully and get excellent patterns of the face-centered cubic type. These revealed the interesting circumstance that either the (100) or the (111) crystal direction was likely to be parallel to the wire axis, i.e., at the center of the pattern, so that patterns of both threefold and fourfold symmetry were displayed. Platinum has been used experimentally (5, 80), its patterns appearing not unlike those of nickel.

Schleicher (81) fabricated emitters of iron and obtained a variety of patterns, none of which he thought represented the clean metal, perhaps

because of oxides or other adsorbed impurities which could not be removed at temperatures up to the cathode melting point. Müller (3) has reported the successful use of niobium, vanadium, and copper in addition to those named above.

A recently reported metal for use in field emission is rhenium, with which Barnes (82) obtained both reproducible current-voltage curves and apparently clean patterns. This metal, only recently available in wire form, has both high melting point and tensile strength, properties desirable in field-emitter materials. Barnes's patterns display emission variation corresponding to a metal of the hexagonal close-packed crystal system.

Field-emission patterns depend on crystal structure and exhibit changes corresponding to those which the structure undergoes. Brock and Taylor (83) obtained an interesting series of patterns from titanium during its transformation from the hexagonal-close-packed alpha phase found at low temperature to the body-centered cubic beta structure at 882° C. Electron emission patterns from the titanium single crystal held in either of the two temperature ranges showed the symmetry of their respective stable crystal structures. Daughenbaugh (84) observed iron at a similar transition temperature, using pulsed T-F emission microscopy (Section V,6) to enhance cathode geometric stability; there was some evidence of a pattern change. Schleicher (81) had been unable to maintain sufficient stability for that purpose when steady-state electric fields were used.

D'Asaro (85) has used as cathode an alloy of a few percent of zirconium in molybdenum. Upon heating the emitter, diffusion of zirconium from the interior onto the surface was observed near the (100) plane. The diffusion rate increased after a 2400° K flash, supposedly as a result of an increased vacancy concentration. Activation energies for the diffusion process can be computed from these observations.

4. On the Visibility of Single Atatoms and Admols

One of the most interesting and yet controversial subjects in recent field-emission work is the question of the visibility of emission pattern detail originating at single atom or molecule sites.

Müller originally proposed that an observed granular pattern structure was caused by enhanced electron emission at adsorbed barium atoms on the tungsten substrate (35, 86). Becker (25, 87) questioned this interpretation, suggesting that the emission originated at clusters of several barium atoms. More recently there has been additional experimental evidence on this point which will be described below.

Müller proposed also that an observed "four-leaf clover" pattern was

the image of the outline of an adsorbed phthalocyanine molecule, a proposal which received widespread popular attention (88, 89). Later work of Müller and others (8, 90) has shown that there is not necessarily any correlation between pattern detail and molecular form, similar fourfold symmetry appearing for admols of other configurations. However, several workers apparently believe that the observed emission does indeed originate at single adsorbed molecules. Becker (91), in particular, has observed intriguing patterns from oxygen on tungsten which he believes originate at single admols; this work is described briefly below.

Gomer (92) has recently introduced a theory concerning field emission from an admol which, while approximate, is an interesting and useful formulation which he partially verifies by experiment. Meanwhile, Rose (74) has predicted a 3-A resolution for the field-emission microscope under conditions discussed in Section V,2, which tends to support the proposed atomic visibility.

Trolan *et al.* (44) have offered proof that electron emission is observed from a surface irregularity of atomic dimension, as will be discussed in Section V,7. Although the irregularity is one-dimensional, i.e., the edge of a lattice plane, the observation does tend to strengthen the proposals in this section relating to the resolution of single-atomic and molecular detail.

If the present state of the question is less than convincing, it is probably not surprising in a relatively new field of science which may still lack definitive experiment and theory. It does limit the number of firm conclusions which can be drawn at this time; hence, present comments will be limited to a review of the present status and the expressed confidence that further clarification will result from considerable work now in progress.

Müller's review (8) contains the history of his observations with phthalocyanine. The first images obtained in the emission pattern, not reproducible here because of loss of the original negatives, were strikingly similar in outline to the expected fourfold symmetry of the molecule itself, while in other cases the images showed twofold symmetry as if the molecules were standing on edge. The early conclusion of direct magnification seemed almost inescapable, but later Müller and Wolf (8) and Haefer (93) discovered that other molecules of quite dissimilar shapes might also give fourfold images. Müller and Wolf concluded that the images were due to the way in which the electron paths were influenced by the interaction of the adsorbed molecule with the crystal structure beneath, i.e., to diffraction effects, and that the earlier apparent correspondence of shape was accidental. Quoting from Müller's recent review (8), "No relation is recognizable between the crystal form of the sub-

stance and its molecular image" (present authors' translation). Müller's latest interpretation of the emission mechanism at single admols is found in a recent paper (94), from which the following quotation is taken:

An important observation is that the two parts of a doublet or the four of a quadruplet always have exactly the same intensity. This could not be expected if the pattern were mainly determined by the exterior electrostatic field close to the molecule. The adsorption takes place at the edge of a lattice step, which causes an asymmetric shielding. However, this local field distortion would be less disturbant if we consider the image as a scattering pattern. Then the electron wave is primarily scattered inside the large molecule and is divided into two or four beams. Slow electron scattering on gases has not yet been extensively investigated, but we know that scattering angles of 90 deg can occur. The appearance of the divided patterns is obviously connected with the presence of π -electrons in the molecule, whose magnetic moment should yield a strong interaction with the spin of the passing slow electron and cause the beam to split. The formation of the fourfold divided beam in the quadruplet patterns remains still unexplainable with our present knowledge of electron scattering.

The high intensity of the molecule images requires a special mechanism for the emission process. Since the large erected molecule does not approach the metal surface very closely, the energy levels inside the molecule are not widened to a large extent. With ionization potentials higher than the work function of the substrate metal, the occupied zone lies below the Fermi level in the one-dimensional box model (Fig. 31). In this level we have a forbidden zone inside the molecule. The application of the electric field causes the levels to be tilted in such a manner that the next originally unoccupied band lies partly below the Fermi level and is being filled up by substrate electrons tunneling through the forbidden zone. From this reservoir, electrons can easily tunnel through the small potential hump in front of the molecule to give the observed large current density.

This model explains also why phthalocyanine patterns appear in the same way whether the substrate is covered with oxygen and emits at 60 Mv/cm or is covered with barium to emit at only 12 Mv/cm. Direct field emission from the occupied π -electron level of the molecule itself would of course, always require the same field strength.

The model holds for molecules as well as for insulating crystals. The field is far beyond the breakdown field strength of any insulator, so that there is no difficulty in tunneling through the forbidden zone. If the erected molecule or insulating crystal is large enough, between 15 and 20 Au, the potential hump in the front is lower than the Fermi level inside the cathode and the emitting particle is completely "open," the current density is generally limited only by the tunneling through the forbidden band. Small crystals of this size may therefore also give a large electron emission, but they can easily be distinguished from single molecules by their almost continuous growth in condensation experiments.

On the other hand, Gomer and Speer have found reason to favor the interpretation of such images as direct representations of the actual mo-

lecular shape (92). They achieved an additional step forward in technique by obtaining patterns from phthalocyanine on very clean tungsten (in Müller's work the adsorbed molecule rested on a layer of oxygen on tungsten) with only a few specimens or possibly a single molecule of the adsorbate visible (Fig. 32). Examining the emission from such a single

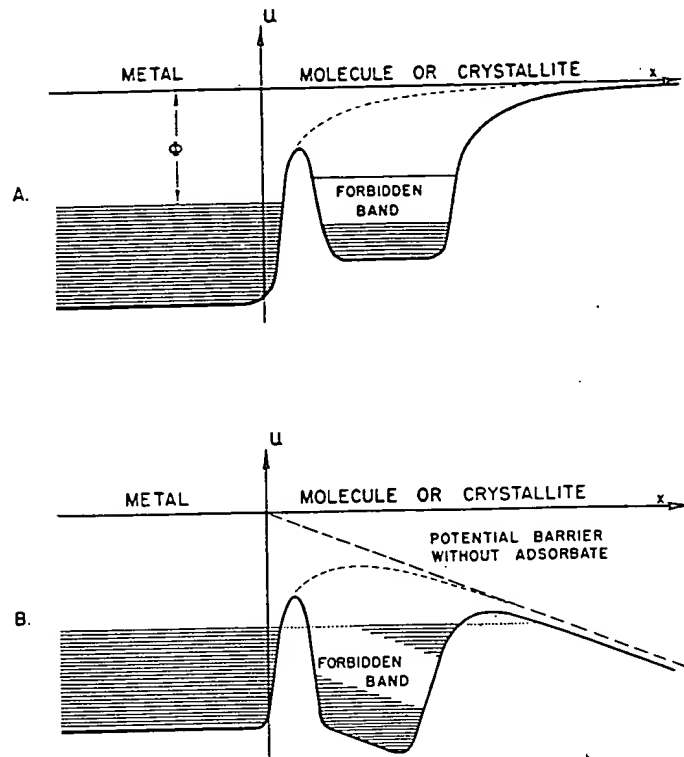


FIG. 31. Potential barriers of a metal with adsorbed molecule or crystallite; (a) with zero applied field; (b) with large applied field, substrate electrons are transmitted through forbidden band and thin surface barrier in large current densities. (Permission of E. W. Müller.)

source with a sensitive photometric arrangement, they found that current varied exponentially with voltage in the same manner as emission from a gross surface, a result which suggested field emission directly from the adsorbed molecule itself. To support this hypothesis they developed a wave-mechanical treatment of electron emission from a potential box representing the adsorbed molecule, assuming that electrons emitted from the molecule could be readily replaced through the low barrier between it and the substrate. The enhancement of surface field was estimated by

using a molecular model in an electrolytic trough. Results of this theoretical study were found to be in substantial agreement with experiment. Finally, they calculated the resolving power to be sufficient to permit separation of images from the four regions of the molecule.

In Müller's most recent work (72), while he refers to the foregoing report of Gomer and Speer, he does not accept their conclusion and reasserts his conviction that the shape of the pattern is independent of that of the molecule.

Similar disparity in points of view appears in the question of whether single-atom effects are visible in emission patterns. In this connection

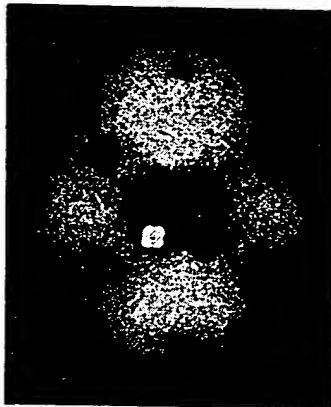


FIG. 32. Pattern of a clean tungsten emitter with a single adsorbed molecule of zinc phthalocyanine. (Permission of R. Gomer and the American Institute of Physics.)

only two recent papers will be cited. Becker (25, 87) had earlier questioned Müller's proposed resolution of electron emission from single adsorbed barium atoms (35, 86), and preferred to attribute the questionable patterns to groups or clusters of the atoms of an adsorbate. More recently, Becker has made an extensive study of oxygen on tungsten which he has described in detail in an excellent article (91) which merits careful reading. Much of the work deals with adsorption and desorption and is summarized briefly in Section V,5; at this point attention is directed to an interesting pattern detail which Becker interprets as emission from an oxygen molecule adsorbed in the third layer. Such patterns were observed only after the tungsten tip was heated in oxygen at relatively high pressure. In some cases the emitter was heated to 600° K at a pressure of 10^{-2} mm Hg; in others the pressure was gradually reduced from that value while the whole glass system was baked at 650° K for about an hour on the pumps. When the system was cool, the anode voltage was increased until a pattern was seen. The voltage was always less than that

necessary to see a pattern for two layers of oxygen-on-tungsten and was frequently less than that for clean tungsten. The patterns were of an entirely different nature from those normally observed: they consisted of intensely bright spots or groups of spots, any one of which might suddenly change its orientation or intensity or change to another grouping. The spots were usually grouped as doublets or quadruplets; the changes which these normal forms underwent are shown in Fig. 33. The groups had no obvious relation to the underlying tungsten planes; from their behavior, Becker concluded that they revealed individual atoms or individual molecules which were adsorbed on the underlying layers of strongly chemisorbed oxygen. He proposed that such visibility occurred only when

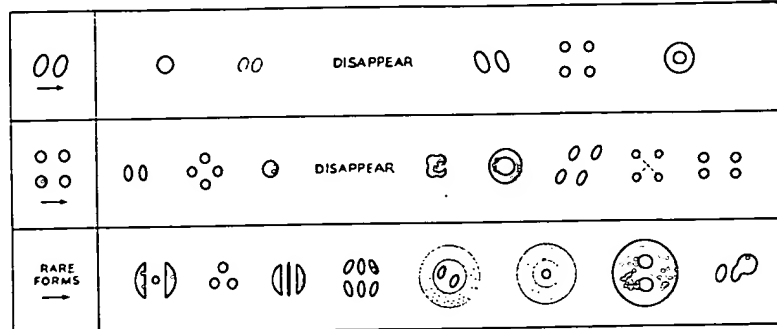


FIG. 33. Patterns of units and transitions observed in field-emission microscopes when the tungsten surface has been treated in special ways. It is believed that each bright spot in a unit is due to an individual atom in simple molecules like O_2 , O_4 , or O_6 . (Permission of J. A. Becker.)

the adsorbed molecule rested on a protruding tungsten ridge, as in Fig. 27, a condition which Rose (74) found favorable for a 3-A resolution as required for the proposed visibility (see Section V,2). Becker observed that tungsten ridges were formed at various tungsten crystal faces at intermediate temperatures in the presence of oxygen, an effect which he attributed to altered surface free energy, in keeping with the theoretical predictions of Herring (95). Molecules closer to the substrate, he reasoned, would not show sufficient contrast or have sufficient resolution for individual recognition. Visibility of single oxygen molecules on the clean metal base is still not a probability in Becker's view. Müller feels that this latest work of Becker's involves crystallites of WO_3 , not single oxygen particles (72).

Müller, however, has presented his own latest version of visible single atoms, this time with barium, using an interesting new technique (94). His arrangement consisted of a pair of emitters located at different dis-

tances from a single source of evaporated barium atoms, so that one surface received 40 times as much deposit as the other. When the nearer emitter had received a monolayer of adsorbate (identifiable by a minimum value of work function), the pattern of the more remote emitter was recorded. After the surfaces were cleaned, a smaller deposit was made until the nearer emitter pattern matched the former appearance of the other, i.e., 1/40 of a monolayer. At this point the remote emitter had only 1/1600 of a monolayer, corresponding to 40 individual adatoms; about 20 individual emission sites were counted as bright spots on the screen, which corresponded closely enough to the expected 40 to convince Müller that the sites were adatoms.

If, as Müller suggests, there is more evidence for than against the visibility of emission pattern detail arising at single atomic or molecular sites, nevertheless, in the authors' view, the question appears at present to be unsettled, pending further conclusive proof.

5. Adsorption and Desorption

One of the more important applications of the field-emission microscope is in the study of adsorption and desorption phenomena at the metallic cathode surface. Such studies provide a new approach to problems in catalysis and surface chemistry; their understanding is a prerequisite to the development of a method for controlling the electrical behavior of the cathode for use in practical electronic devices, as will be described in Section VII.

Minute quantities of adsorbate may cause large changes in field-current density, and the resulting changes in current can be measured accurately; therefore, field emission can be used to determine quantitatively the behavior of adsorbates in quantities perhaps as small as a single atom or molecule, as was discussed in the previous section. The current response usually depends on the type and extent of electron transfer between adsorbate and substrate, through its effect on the surface work function. From the observed current one may study the electron transfer and judge the nature and value of the forces bonding the adsorbate and surface.

Temperature has little effect on field-current density (Sections II and III, 8), but temperature may cause relatively large changes in the amount of adsorbed material, an effect which can be easily observed. From the foregoing it is clear that the field emission microscope is a powerful tool for the study of adsorption and desorption phenomena.

One distinguishes between chemisorption, in which the adatom or admol shares electrons with the substrate, and physical adsorption, in which the bonding is by physical forces. In chemisorption, the usual

chemical bonds between the atoms in a molecule may be broken and replaced by equivalent bonds with the substrate, resulting in a chemical reaction at the cathode surface. The resulting electric dipole layer often has a marked effect on work function and hence on field current.

The earliest field-emission experimenters were well aware of the erratic behavior of the emission and its high sensitivity to adsorbates. From Fig. 2, one sees that the field-current density can change by as much as a factor of 10^6 with reasonable changes in work function. One source of adsorbates is the residual gas in an experimental tube; the corresponding effect on the electron emission is often sufficiently strong that experiments with the cold cathode must be carried out at the highest vacuums, e.g., 10^{-9} mm Hg. Millikan and Lauritsen (23) were among the first to achieve adequate cathode stability by that means and as a result were able to establish the validity of Eq. (9).

Müller made qualitative observations at an early date on the adsorption of oxygen (63) and barium (86) on tungsten using the field-emission microscope, and from those emission patterns a dependence of adsorption upon crystallographic direction was immediately apparent. Moreover, Müller observed the desorption process at high temperatures (63), and later at high field strengths (5a, 96). Thereafter, he extended observations to a large number of adsorbate-substrate systems, and has presented an excellent summary of that work in his recent article (3). Benjamin and Jenkins (77) made an interesting series of observations, also largely qualitative, which have also been summarized by Jenkins (2).

In recent studies there is a growing trend towards quantitative observation and the interpretation of data in terms of basic concepts. Among such studies, one of the better is the new work of Becker concerning oxygen-on-tungsten (91). As Becker notes,

From experiments with the field-emission microscope we can learn that for a system like oxygen on tungsten: (a) the crystallographic plane of the tungsten has a marked influence on the adsorption properties; (b) the heat of adsorption increases with the number of W atoms a particular O atom can contact; (c) the heat of adsorption for the first layer, in which O atoms make first valence bonds with W atoms, is about four ev; for the second layer, in which O atoms make second valence bonds with W atoms, the heat of adsorption is only about two ev; (d) at a constant pressure, the rate of adsorption is constant until the first layer is complete; for the second layer, the rate of adsorption is slower by a factor of 100 or more; (e) beyond the second layer oxygen is adsorbed as admols of O_2 , O_4 , O_6 .

From experiments with a modern ionization gauge and for a system like nitrogen on tungsten we learn that (a) only a fraction of the nitrogen molecules that strike the tungsten surface stick to it and become chemisorbed; this fraction is called the sticking probability; (b) this sticking probability is about 0.4 at 300° K;

(c) it is constant to about one layer and then decreases rapidly until at two layers it is only 10^{-4} ; (d) the activation energy increases with amount adsorbed beyond the first layer.

In one experiment, the cold tungsten cathode was given a heavy oxygen coating at a pressure of 10^{-5} mm, at which a monolayer is deposited in about 0.1 sec. The pressure was then reduced to 10^{-9} mm, and the emission pattern was observed from the cold cathode between successive

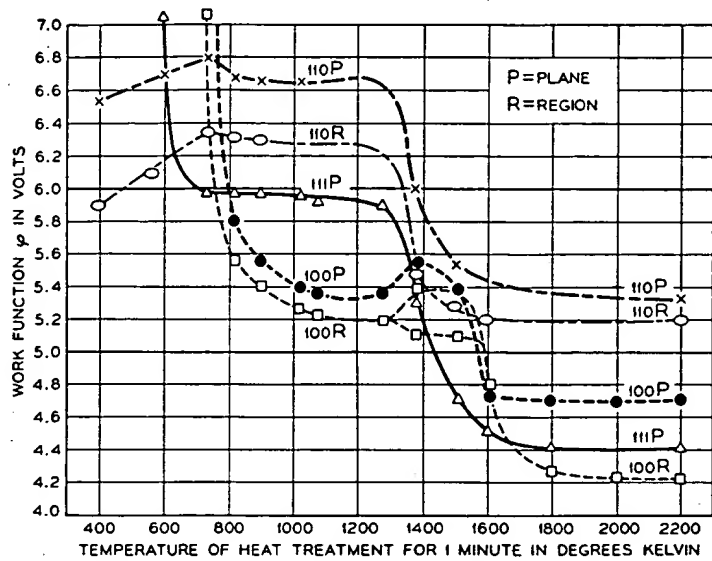


FIG. 34. The electron work functions for various crystallographic planes *vs* the temperature of heat treatment: for oxygen on tungsten. (Permission of J. A. Becker.)

heat treatments of one minute at each of several temperatures in approximately 100° K steps from about 400° K up to 2200° K. The heat treatment was given in the absence of electric field in order to avoid rearrangement of the adsorbate due to electrostatic forces. A series of photographs taken during this procedure showed startling changes in the emission from various planes; the current densities from several planes were measured photometrically, and the corresponding changes in work function deduced from Eq. (5). Becker's graphs of work function *vs* temperature are shown in Fig. 34.

To interpret these curves, Becker focuses attention on the $111P$ curve, i.e., that from the (111) plane, as follows:

A fairly obvious interpretation is that at 600 to 700° K a considerable amount of oxygen is desorbed and as a result, ϕ decreases from 7 to 6 volts. Between 700

and 1300° K, very little additional oxygen is desorbed and hence ϕ remains constant. At 1400° K more oxygen is desorbed rapidly and hence ϕ decreases. Above 1600° K the oxygen is completely desorbed and ϕ remains constant at 4.4 volts. Apparently the oxygen is desorbed in two successive stages or "layers" at about 700° K and at 1400° K, respectively. Let us call the 700° stage the second layer, and the 1400° stage the first layer.

That the observed changes in work function were indeed due to the desorption of oxygen was confirmed by subsidiary flash filament experiments in which the pressure increase due to desorbed oxygen was measured by an ion gauge.

One of Müller's most recent publications (72) includes a series of experiments similar to those described by Becker as reported above. His results are closely similar to those expressed in Fig. 34, but the scale of work functions does not agree with Becker's, and the temperatures at which the successive steps of desorption take place show considerable variation in the two papers. His interpretation of these steps as corresponding to first and second layers of oxygen is identical with Becker's.

The disparity of results between these experienced workers, using apparently identical methods and with the same purpose in mind, may serve as an example of the uncertainty that often clouds the interpretation of emission patterns.

Desorption may also result from other mechanisms besides evaporation at elevated temperatures. First, chemical reactions may lower the surface energy sufficiently to permit evaporation at reduced temperature. For example, Müller (72) observed that the entire oxygen coating was evaporated as WO_3 at temperatures below 1760° K, for which little evaporation of pure tungsten is expected. Müller and Wiegman (8) noted that oxygen on tungsten was attacked by hydrogen ions at 80° K and was removed in contact with hydrogen molecules at temperatures from 1300 to 1500° K.

Secondly, desorption occurs even at low temperatures in the presence of a very high electric field, usually greater than 10^8 v/cm. For this purpose the metal is made positive to prevent excessive electron emission and is often the needle of a usual field-emission microscope so that the effects of desorption can be viewed in the electron emission pattern obtained by a simple reversal of potential.

Field desorption of barium, thorium, and oxygen occurs in the 100-, 200-, and 500-Mv/cm ranges for the three substances, respectively. At the highest field, the tungsten substrate itself evaporates at room temperature. The quantitative interpretation of the measurement suggests that field desorption involves the evaporation of ions over an energy hump which is reduced by the Schottky effect. Accordingly, it has been

shown (97) that the field F at which field desorption occurs can be described by the relationship

$$F = C_1 + C_2\theta^{5/4}$$

where F is in MV/cm, θ is the degree of coverage of the adsorbate on tungsten, and C_1 and C_2 are constants depending on the adsorbate. For barium, $C_1 = 78$ and $C_2 = 66$ MV/cm; for thorium, $C_1 = 243$ and $C_2 = 43$ MV/cm.

Field ionization, reported by Inghram and Gomer (98), is a related although distinctly separate phenomenon of considerable importance. In this case, ionization occurs near a metal surface in the presence of a high field, with the metal positive to prevent excessive field emission. Electrons are transmitted through a thin potential barrier from the approaching atom or molecule into the metal. Ions are thus formed at or near the surface for low fields, and at distances up to several atomic diameters from the surface for fields of the order of 10^8 v/cm. The proposed electron tunneling mechanism was strengthened by the absence of any observed major mass effect on the ionization efficiency, thus precluding a mechanism based on the tunneling of positive ions.

Inghram and Gomer derived an analytical expression for ion current in which the supply of neutral particles was based on the interaction of their dipole moment with the large inhomogeneous electric field at the metal surface, a highly curved tungsten needle. The probability of ion formation was treated by wave mechanics, considering the penetration by electrons of the metal surface barrier from ion to metal and deriving the frequency of electron impact from its Bohr orbit.

Field ionization provides a point source of ions. When used with the mass spectrometer of Inghram and Gomer, it has a number of potential applications: (1) the study of fragmentation processes accompanying chemisorption, (2) the analysis of gas mixtures, (3) the determination of transient and short-lived intermediates of low concentration, (4) the determination of the lifetimes of excited atoms or molecules, (5) the analysis of solid adsorbates, (6) the formation and study of negative ions.

6. Pulsed T-F Emission Microscopy

Pulse electronic techniques extend the advantages of field emission microscopy to desirable experimental conditions not attained with steady-state electric fields (99). Such conditions include elevated cathode temperatures, increased environmental gas pressures, and cathode materials of low tensile strength. The method consists of applying to an emitter a high pulsed field of short time duration (say 1 μ sec) at a repetition rate (e.g., 30 pulses/sec) such that the image on the microscope screen is vis-

ually continuous but the field duty cycle* is low. The emission pattern provides a "motion picture" of events at the emitter surface, while the adverse effects of large steady electric fields are avoided. The desirable electrical stability which accompanies pulsed *T-F* operation and the immunity to surface contamination in the presence of relatively high gas pressures are discussed in Section VI.

Phenomena occurring at high temperatures may be studied by this technique, although they may be impossible to observe under steady fields, since surface distortion or "build-up" then leads to altered electrical performance and cathode destruction by vacuum arc. Furthermore, at temperatures above about 2000° K, thermal emission from the supporting filament with its large emitting area may mask the pattern under steady operation, whereas its effect is negligible in the pulsed case because of the high field-current densities which may be obtained. Such temperature-dependent processes as surface migration or volume diffusion may be examined by steady-state methods only through the awkward procedure of alternately activating the process by the use of temperature without field, then reducing the temperature and looking at the results with cold field emission. The limitations of time measurement are evident; events may happen so quickly as never to be seen at all, whereas the pulse method reveals events continuously, with the added advantage that one can reduce the temperature and "freeze" any unexpected condition that may occur.

Metals of low tensile strength are subject to instability when used as field emitters under large steady fields, because the large associated electrostatic forces approach the strength of crystal binding forces; difficulties have been reported with nickel (79) and iron (81). On the other hand, a nickel cathode has exhibited electrical stability under pulsed *T-F* operation at temperatures approaching its melting point.

The stability of the pulsed tungsten *T-F* emitter at gas pressures up to 10^{-4} mm Hg (Section VI) suggests that the corresponding patterns may be used to study such dynamic processes as adsorption, desorption, and catalysis.

7. Electron Emission from a Single Lattice Step

Against present uncertainties regarding the visibility of single atom and molecule effects stands the proven resolution of electron emission from a row of atoms, i.e., a single lattice edge of atomic dimension. The resolution of a single lattice step will be useful in crystal surface studies; step-height resolution has been limited to 15 Å by optical interferometric methods (100). Such data have been useful in the experimental measure-

* Duty cycle is the ratio of field-on time to total time.

ment of the work function ϕ_{110} for tungsten (Section III,5); the method permits direct measurement of activation energy for the surface migration of tungsten on tungsten as described in Section V,8.

There often appears a bright ring of electron emission concentric with and well inside of the normally dark, nonemitting (110) face of tungsten, as in Fig. 35. Such rings have been observed both on clean tungsten (31) and when adsorbates were attached to a lattice edge (75), using the field-emission microscope with steady-state fields; however, there has been no previous proof that such emission originated from a single lattice step.

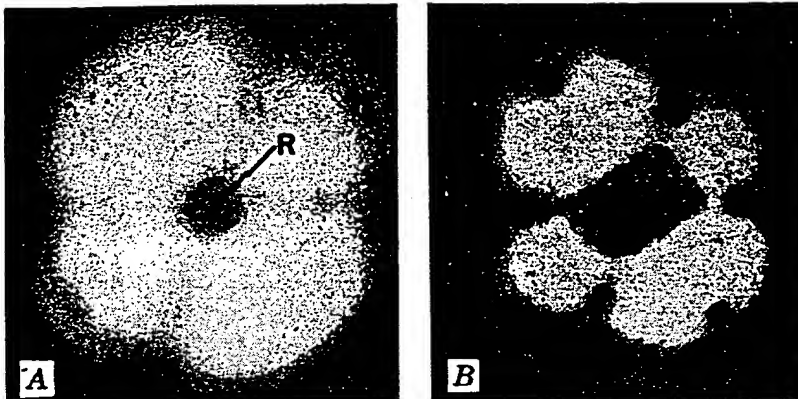


FIG. 35. Emission patterns from a clean tungsten emitter: (a) at high current density, $J = 5 \times 10^7$ amp/cm 2 , during pulsed T-F operation, showing pattern ring at R in central dark (110) area; (b) at low current density, $J = 25$ amp/cm 2 , typical steady-state operation in which large pattern contrast precludes visibility of ring.

Trolan *et al.* (44) observed similar rings using the improved techniques of pulsed T-F emission microscopy described in the preceding section. Current densities of 10^7 amp/cm 2 were drawn from tungsten at fields of the order of 6×10^7 v/cm. The normally large pattern contrast was reduced by space-charge effects, permitting accurate measurements of current density in the usually dark (110) face by photometric methods (33). A duty cycle of 3×10^{-5} provided a visually continuous emission pattern while holding at a negligible level the adverse effects of the applied electric field on both the cathode electrical stability and the mechanisms under study. In particular, it was possible to heat the cathode to temperatures up to 3000° K without causing "build-up" (Section V,8) or vacuum arc.

Figure 35b shows a typical tungsten pattern at low current densities; at high density, Fig. 35a shows a typical ring in the central (110) tungsten face; a photographic enlargement of a similar ring R is shown in Fig.

36a. When the cathode temperature is increased, e.g., to 2000° K, the ring R decreases in radius and in a few seconds disappears, as in B through D ; after a short period, the sequence is repeated. The ring rate increases rapidly with temperature, where the rate is defined as the number of rings collapsing per second.

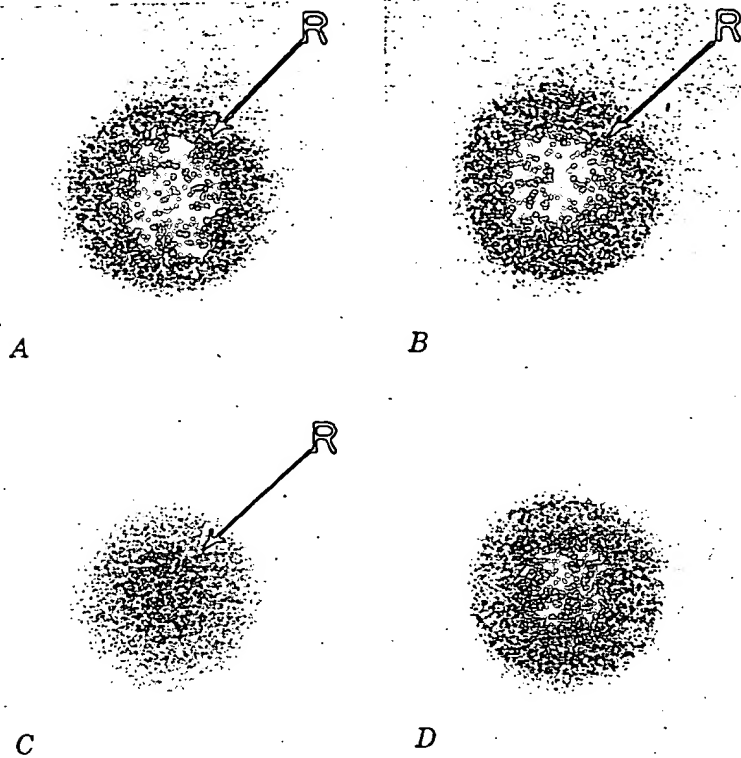


FIG. 36. Photographs of the emission pattern of the central (110) plane of tungsten showing successive stages of ring collapse, A through D , corresponding to the dissolution by surface migration of the outermost atom layer from the (110) plane of the heated tip, viewed by T - F emission microscopy.

The observations are interpreted through reference to Fig. 37, which shows in section the two outermost atom planes of the (110) crystal face whose normal is parallel with the emitter axis. The ring emission, shown as solid electron trajectories, originates at the edge atoms R (shown in black) of the outermost atom plane; enhanced emission results from increased roughness, which is known both to lower the work function (40, 96) and to increase the field factor β . The edge atoms R may be lost from their plane by two processes which thereby reduce the diameter of the

remaining outer plane: first, surface migration, arrow *M*; second, volume diffusion, vertical arrow. Correspondingly, the emission pattern ring *R* is reduced in size with time as in Fig. 36.

There were two consequences of this proposed mechanism which appeared sufficiently significant to encourage experimental investigation: first, the resolution of electron emission from a single lattice step, which, while relating to the important question of single atom visibility, had not previously been verified; and, second, a means for measuring a length change of approximately atomic dimension which could provide highly accurate methods for calibrating electron microscopes, measuring self-diffusion constants, etc. For these reasons the following experiment was

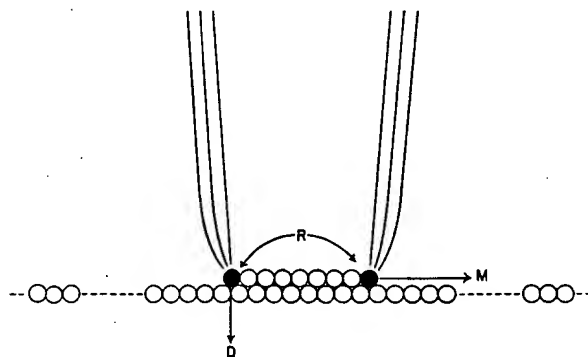


FIG. 37. Cross section of idealized tungsten emitter tip showing two outermost atom layers of the (110) face. Emission forming pattern ring originates in the vicinity of edge atoms at *R* of top layer. Edge atoms are least tightly bound, and when thermally agitated, may be removed by surface migration as at *M* or by volume diffusion into vacancies in the metal lattice as indicated by vertical arrow.

undertaken to establish whether each collapsing emission pattern ring in Fig. 36 corresponds to the removal of one atom layer from the (110) face of tungsten.

For this purpose one requires an independent method of measuring the cathode length change. Clearly, it would be difficult otherwise to observe that an object of size 1μ changes length in the amount of an atomic dimension; however, electron microscopy easily resolves size changes of 1000 atom diameters, corresponding to which 1000 collapsing rings can be counted and the desired comparison made. In Table VI are presented such comparisons for three tungsten cathodes; the length changes agree within about 10%, which establishes that each collapsing ring is associated with removal of an atom layer.

A point of reference for length measurement was required in the electron micrographs. Use was made of grain boundaries, as at *P* in Fig. 38,

TABLE VI. Number of Collapsing Rings and Change in Emitter Length, for Three Emitters.

Emitter designation	Number of rings	Change in emitter length	
		Predicted value on the basis of: ring to 1 atom layer (cm)	Measured value from emitter shadowgraphs (cm)
X160	3000	6.7×10^{-5}	$(6.4 \pm 0.6) \times 10^{-5}$
X127	1960	4.4×10^{-5}	$(5.0 \pm 0.5) \times 10^{-5}$
Q218	2500	5.6×10^{-5}	$(5.7 \pm 0.6) \times 10^{-5}$

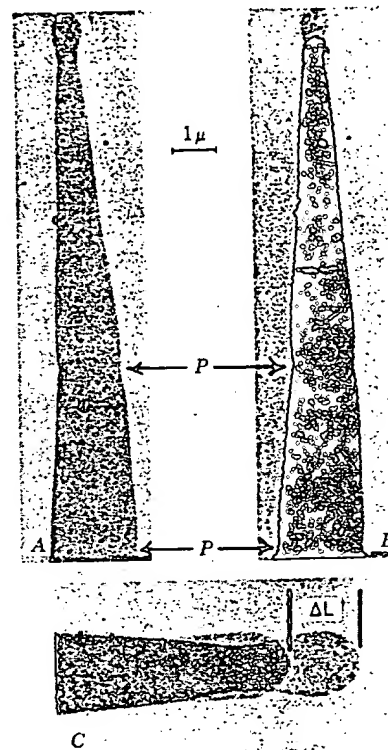


FIG. 38. Electron microscope shadowgraphs of the profile of emitter X160: (a) before operation, with length reference points indicated at P ; (b) superposition of shadowgraphs obtained before and after operation with matched reference indentations at P ; (c) expanded view of the superimposed tips, showing decrease ΔL in emitter length accompanying the collapse of 3000 pattern rings.

needle curvature and accidental deformities such as surface indentations. Overlays of the micrographs before and after dulling, as at *B* and *C*, Fig. 38, reveal the length change ΔL and the transport of tip material to areas at larger polar angles.

As added proof for the foregoing mechanism, one has the agreement of the experimentally observed surface migration with the theory of Herring presented in the next section.

8. Surface Migration

It is quite possible to find an intermediate temperature at which a metal's surface atoms receive sufficient energy to break a few, but not all of their bonds with near-neighbor atoms. Unless all bonds are broken, evaporation is impossible. If a few bonds are broken, the atom may move across the surface to a new position; this mechanism is called "surface migration."

Migration may be motivated and directed by forces derived from several sources; those which have been noted experimentally include gradients of (1) chemical potential, (2) temperature, and (3) electric field. Until recently there has been surprisingly little known about these mechanisms. The understanding and measurement of surface migration, either of an adsorbed material upon a substrate or of the emitter metal on its own lattice, have achieved notable advances by the use of field-emission microscope techniques. Müller described such phenomena in 1938 (35), when he attributed to surface migration the increase in radius of an emitter tip after heating and also observed that barium, condensed upon one side of a cold tungsten emitter, moved unmistakably across the surface when the temperature was raised. These original observations are typical of two basic methods that have been applied to quantitative migration studies using field-emission techniques: (1) measurement or calculation of the time rate of gross changes in emitter geometry and (2) measurement of the surface-flow rates of adsorbates whose work functions differ from that of the substrate and thus contribute to visible pattern changes.

a. *Clean Metals in the Absence of Externally Applied Surface Stress.* Müller (101) later measured the activation energy for the migration of tungsten on its own lattice in two different ways. In the first of these, he measured the time required to change the radius of an emitter by a certain amount, then calculated the volume of material moved; the time rate of removal of atoms from the tip was correlated with temperature to obtain an activation energy for the process of $106,500 \pm 8000$ cal/mol. From the present point of view, the accuracy of this result is open to question because (1) electron micrographs being unavailable, the radius was

not measured directly, but was deduced from the current-voltage relation, and (2) the amount of diffused material was calculated on the assumption of a consistent sphere-on-tangent-cone geometry with a vertex angle which could be estimated only within broad limits. Although a considerable geometric uncertainty may thus have been present but undetected, the experiment was nevertheless an important first achievement.

In his second method, Müller deposited additional tungsten upon an emitter tip from an auxiliary source, noted the changes thus induced in the emission pattern, and measured the time required for various crystal faces to resume their normal pattern, as a function of temperature. In the case of condensed material removed by migration from the margins of the (110) surface, the calculated activation energy was $80,000 \pm 8000$ cal/mol; several other measurements at various faces and for various types of condensate were made. He was able to make satisfactory comparisons of these rates with the theoretical studies of Stranski and Suhrmann (102), in which binding energies were based on the attractive forces of neighboring atoms at any given lattice site. In a recent theoretical study Herring (95) suggested that, under the experimental conditions reported by Müller, the observed cathode blunting was probably due to volume diffusion rather than surface migration.

Herring's theory, together with the experimental techniques of pulsed T-F emission microscopy, permit a more quantitative description of cathode blunting. It is first shown that surface migration is the primary mechanism involved and then an experiment is described in which the constants involved in that process were evaluated.

An auxiliary experiment, not involving field emission, was performed to confirm the migration hypothesis. Herring had pointed out (103) that the times required for two geometrically similar aggregates to undergo proportional changes in dimension should vary with the cube of the radius for volume diffusion, but with the fourth power for surface migration; he suggested this type of measurement as a means of distinguishing between the two processes.

The shape changes that a tungsten needle undergoes during successive stages of blunting may be used in this connection. Emitters were heated at known temperatures for measured times in the conventional electron microscope, making use of the specially modified sample rod described in Section VIII; radii were directly measured in the shadowgraph. Since geometric similarity was usually preserved at successive stages in the enlargement of emitters (except in a few anomalous cases of geometric distortion), this experiment fulfilled Herring's condition. The choice among proportionality factors is indicated by Fig. 39, where the slope 4 corresponds to surface migration.

Knowing that blunting is a surface-migration mechanism, one may turn to an evaluation of the constants involved in the process. Herring

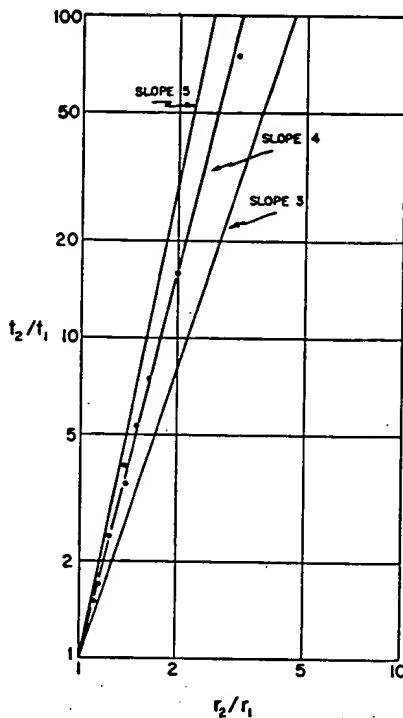


FIG. 39. Graph showing ratio of elapsed times t_2 and t_1 required for proportional changes in geometrically similar tungsten emitters of radii r_2 and r_1 , at several temperatures between 2500 and 2800° K. Slopes 3 and 4 correspond to theoretical predictions for volume diffusion and surface migration, respectively.

(95) has shown that the flux S of surface material in atoms per centimeter-second is given by the relation

$$S = \frac{D}{A_0 k T} \nabla \mu \quad (31)$$

where A_0 is the surface area per atom in square centimeters, k is Boltzmann's constant in ergs per atom degree, T is temperature in degrees Kelvin, and

$$D = D_0 e^{-Q/kT} \quad (32)$$

is the usual diffusion equation with D in square centimeters per second, Q is the activation energy, D_0 is a constant with the same units as D ,

μ , given by the relation

$$\mu = \mu_0 + \left[\gamma \left(\frac{1}{R_1} + \frac{1}{R_2} \right) + \frac{\partial^2 \gamma}{\partial n_x^2} \cdot \frac{1}{R_1} + \frac{\partial^2 \gamma}{\partial n_y^2} \cdot \frac{1}{R_2} - p_{zz} \right] \Omega_0 \quad (33)$$

is the chemical potential in ergs per atom, γ is the surface tension in ergs per square centimeter, R_1 and R_2 are the principal surface radii of curvature in centimeters, p_{zz} is any externally applied stress on the surface in dynes per square centimeter, n_x and n_y are surface normals, and Ω_0 is the atomic volume in cubic centimeters.

These equations may be used in the manner of Herring to show that D is proportional to the time rate of change in length z of a field emission cathode, assuming the second derivatives of γ in Eq. (33) are negligible because the surface is sufficiently smooth, as follows:

$$D = \frac{dz}{dt} \frac{A_0 K T R}{2 \sqrt{2} \Omega_0^2} \cdot \left(\frac{\gamma}{R^2} - \frac{\nabla F^2}{8\pi} \right)^{-1} \quad (34)$$

For the case when the effect of the electric field is negligible, the right-hand term in the brackets of Eq. (34) is zero, and dulling progresses under the action of surface forces alone; this case applies sufficiently well to pulsed T - F emission microscopy at a field duty cycle of 3×10^{-5} , for which Eq. (34) becomes

$$D = \frac{dz}{dt} \cdot \frac{A_0 K T}{2 \sqrt{2} \gamma \Omega_0^2} \cdot R^3 \quad (35)$$

This yields values of D directly from measured values of dz/dt , temperature, and tip radius R . A highly accurate measurement of the time rate of length change, dz/dt , results from direct observation of the dissolving atom planes of the tungsten (110) face by means of pulsed T - F emission microscopy as described in the preceding section; for example, a rate of 10^{-8} cm/sec can easily be observed by counting the number of collapsing rings per unit time in the emission pattern. Values of R were measured from electron micrographs before and after each run. When experimental values of $\ln D$ are plotted against $1/T$, the result is a linear graph such as that of Fig. 40, which combines several runs of a single emitter, corrected for radius changes between runs as estimated from the current-voltage relationship. The negative of the slope of this graph is proportional to Q , the activation energy used in Eq. (32); the average slope for several tungsten emitters yielded the value $Q = 73,000$ cal/mol, or about 3.2 ev/atom. This is consistent with the hypothesis, established with the aid of the crystal model of Fig. 30, that the edge atoms of the

(110) face must break three of their five bonds with near neighbors in order to migrate over the second plane.

From the intercept on the infinite temperature axis in Fig. 40, the value $D_0 = 0.1 \text{ cm}^2/\text{sec}$ was obtained with an estimated uncertainty of a factor of 5. While no independent values of D_0 were found for comparison, the value of Q obtained here is in reasonable agreement with that from Müller as quoted above for tungsten condensed on the (110) margins.

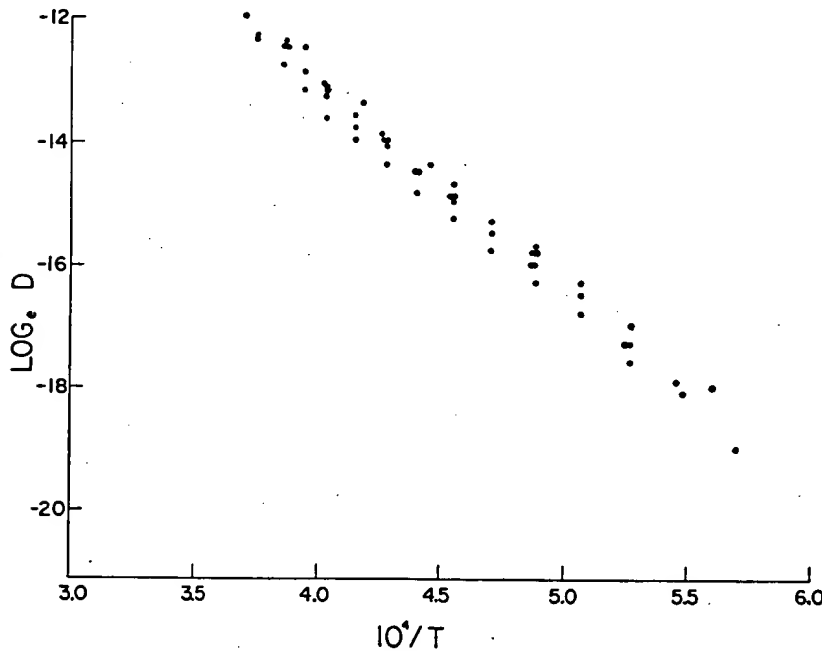


FIG. 40. Graph of natural logarithm of surface diffusion coefficient D in cm^2/sec as a function of reciprocal temperature T , in $^\circ\text{K}$, for several runs of one tungsten field emitter.

In a manner similar to that above, the value $Q = 60,000 \text{ cal/mol}$ was obtained for self-migration on the outermost (110) face of clean tantalum. No comparable measurement is known to have been reported, but the values given here for tungsten and tantalum are consistent with the known approximate proportionality of activation energies to melting points. They also support the conclusion that surface migration, not volume diffusion, is the dominant process at work at the temperatures reported here and at radii of about $3 \times 10^{-5} \text{ cm}$, since the activation energies expected for volume diffusion would be appreciably higher; a value of $108,000 \text{ cal/mol}$ has been given for tantalum (104), and tungsten would be expected to be still higher.

Because the activation energy Q is expected to vary with the binding energy for atoms on various crystal faces, it follows that the rates of surface migration should be a function of crystallographic direction; hence, the cathode should exhibit local variations in both surface curvature and principal face areas with temperature change. Similar changes have been reported experimentally (25).

It was noticed that the radius of a collapsing (110) emission pattern ring (Fig. 36) could be temporarily enlarged by a sudden increase in temperature at the cathode support filament. This indicates a transient reversal of dulling effected by transport of atoms towards the emitter tip. It is conjectured that a wave of material may be swept along the emitter needle from shank to tip by forces accompanying a transient temperature gradient. There is no evidence that ring rate was affected by migration accompanying steady-state temperature gradients known to exist along needles due to radiation loss (101); ring rates were measured in the absence of gradient when the needle was enclosed in a heated black box and were identical with those previously measured.

Occasionally, spiral dislocations on the tungsten (110) face were evidenced as the outermost lattice edge unwrapped as a spiral, instead of the usual collapsing elliptical forms shown in Fig. 36. Drechsler (105) reports frequent observation of similar spiral dislocations using ion microscopy, again for the tungsten (110) face.

There are two practical considerations which relate to the increase of cathode radius during blunting: when intermediate temperatures are used to maintain electrical stability, blunting may cause undesired decreases in β (Section III,3); blunting of several cathodes to a common value of final radius usefully matches their β 's to permit parallel operation at a common applied potential (Section VII). In the latter case, the effect is obtained when the dulling rate is sufficiently reduced by increasing radius, as shown in Fig. 41, which was graphed after integrating Eq. (35) subject to $T = 2000^\circ \text{K}$ and other constants suitable for tungsten. An initially large dulling rate becomes negligible as the tip radius approaches $7 \times 10^{-5} \text{ cm}$, with little further change during subsequent heating. In general, dulling rates increase with decreasing melting point; for example, relatively high dulling rates were observed with nickel, platinum, and iron at temperatures for which the tungsten rate would have been small. The cone angle of an emitter also has an influence on the dulling rate.

b. *Clean Metals in the Presence of Externally Applied Surface Stress.* Equally interesting is surface migration in the presence of a strong electric field (106), for which Eq. (34) is applicable. In this case the electrostatic forces oppose the surface forces and dz/dt may have values that are positive, negative, or zero, conditions for which are seen in the bracket of

Eq. (34). Dulling occurs for $\nabla F^2 < 8\pi\gamma/R^2$; on the other hand, when $\nabla F^2 > 8\pi\gamma/R^2$, principal crystal planes are enlarged and the edges between them are accentuated, a process known experimentally as "build-up," which is unstable and leads to electrical breakdown (Section IV). The case $\nabla F^2 = 8\pi\gamma/R^2$, for which dz/dt is zero independent of

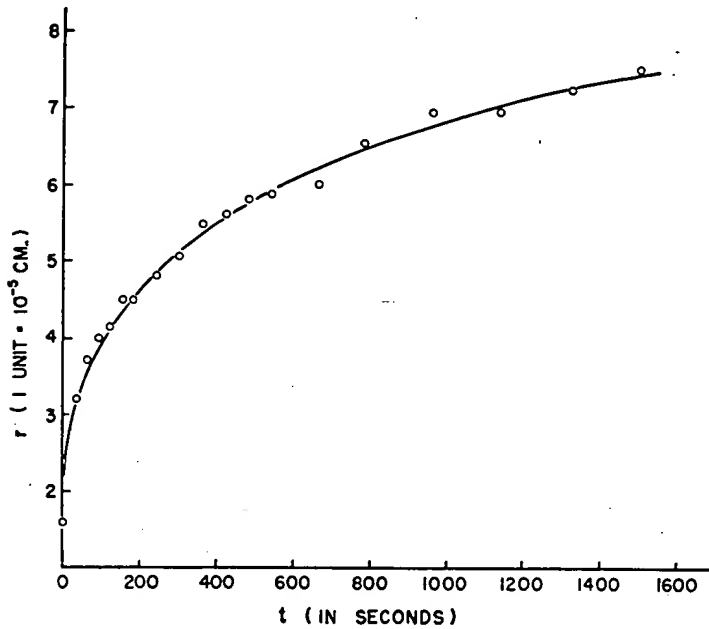


FIG. 41. Radius of a tungsten field emitter (from electron micrographs) as a function of elapsed heating time at approximately 2800° K. Data points (circles) are compared with cubic curve (solid curve) derived from Eq. (35).

temperature is of particular interest: first, the parameter γ can then be evaluated from the equality

$$\gamma = \frac{R^2 \nabla F_0^2}{8\pi} \quad (36)$$

using experimentally determined values for r and for F_0 , the field at which the ring rate vanishes; second, a low-level steady-state bias field can be used to prevent cathode dulling, while an intermediate temperature maintains electrical stability during emission resulting from a separate, higher pulsed field. In this way the technique of T - F stabilization can be extended to emitters with radii smaller than 7×10^{-5} cm which would otherwise dull excessively, as indicated by Fig. 41.

To test Eq. (34) experimentally, one may observe collapsing emission pattern rings in the (110) face of tungsten through the method of pulsed T - F emission microscopy, with a superimposed steady-state bias field F . It is convenient to plot ring rate against increasing values of F for a constant temperature; the data from a typical emitter appear in Fig. 42. Using $R = 5.5 \times 10^{-6}$ cm as obtained from electron micrographs and $F = 1.1 \times 10^7$ v/cm from the graph, one may calculate γ from Eq. (36)

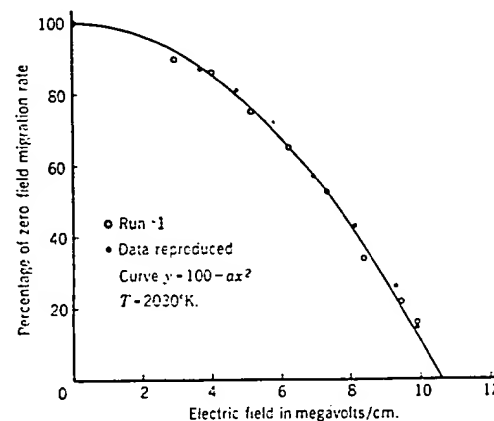


FIG. 42. Graph showing the percentage of the zero field rate of surface migration as a function of applied field, independent of temperature. Experimental data are circles; solid curve is parabola expected from Eq. (34).

obtaining a value of 2500 ± 700 ergs/cm² for the (110) tungsten surface at 2000° K. Herring has estimated a value of

$$\gamma = 4000 \text{ ergs/cm}^2$$

for the cold surface, and it is not surprising that the estimated value is greater than the measured value just reported. First, the measurements were made at high temperatures and a decrease of γ with temperature is reasonable; and second, γ is expected to be a function of crystallographic direction, being of relatively low value on the (110) face where the present measurements were made, as compared with the average value for all faces as estimated by Herring. The main known uncertainty in the measured value of γ is caused by a 15% uncertainty in the value of F_0 , for reasons discussed in Section III.

c. *The Surface Migration of Adsorbates.* In the case of adsorbed coatings on a substrate of tungsten or other metal, quantitative measurements of migration phenomena have also been the exception until relatively recently, most of the publications being largely descriptive.

Studies on tungsten substrates (107, 108) indicate qualitatively similar behavior for hydrogen and oxygen. At very low initial coverages (0.1 monolayer) activated diffusion occurs. The activation energies are 30 and 16 kcal for oxygen and hydrogen respectively, and the migration temperatures for mean diffusion rates of 50 Å/sec are 600° and 250° K respectively. The activation energies represent ~21% of the respective heats of binding at low coverage.

At very high coverages (> 1 monolayer) diffusion occurs with a sharp boundary moving almost uniformly over the tip, and sets in at 40° K for oxygen and below 20° K for hydrogen. The activation energy in the case of oxygen is 1.5 kcal. This type of diffusion involves mobility of gas physically adsorbed above the now immobile chemisorbed layer. Molecules spilling over the edge become chemisorbed, thus extending the layer. This is confirmed by the existence of an upper temperature limit, corresponding to evaporation before trapping at the layer edge can occur. The heat of adsorption in the second layer is calculated to be 7.5 kcal in the case of oxygen, from the spreading time and upper temperature limit. This is approximately five times the activation energy.

At intermediate coverages (~1.0 monolayer) a third type of migration is observed, and occurs at 500° K for oxygen and 220° K for hydrogen. The activation energies are 19 and 9 kcal respectively. A boundary moving radially outward from the central 110 face of the tip is observed. The phenomenon is interpreted as follows. The 110 face is the most closely packed and hence smoothest in bcc crystals, so that energies of adsorption might be expected to be least and mobilities greatest on it. Ad-atoms will therefore diffuse quickly over this face and will spill over its edges, where they will be trapped on the atomically rough surface. However, if the holes or traps can be saturated, even rough faces will approximate the 110 face in decreased binding energy and increased mobility of adsorbate. Thus further gas atoms will diffuse relatively fast over the partially covered rough surface, to be in turn trapped at the completely bare edge, continuing the smoothing process and permitting further migration.

Incidentally to his work on field desorption of oxygen from tungsten, described above in Section V,5, Müller (72) has measured the time required for oxygen to flow from the emitter shank to the tip, replacing a layer removed by high field. He calculated an activation energy for this process of 14,000 cal/mol, independent of the degree of coverage in the shank region at the beginning of the migration.

Klein (109, 110) measured the migration rate of carbon on tungsten, under conditions such that there was a sharply defined moving boundary in the emission pattern between the carbon-coated and the clean tungsten regions. He obtained about 55,000 cal/mol for the activation energy of

this process. Another recent example is that of Kruse and Coomes (111) concerning strontium oxide on molybdenum; here the time rate of surface migration was measured from recorded pattern changes as the SrO migrated from the side of the emitter on which it was originally deposited to other parts of the surface. Although the complexity of these patterns leaves much to the judgment of the observer as to the elapsed time between one stage and another, Kruse and Coomes were able to calculate an activation energy of 14,000 cal/mol for the process described.

Drechsler has written a series of three papers (112-114), in the first of which he set forth the geometric-mechanical foundations of a method for calculating theoretical binding energies of arbitrary adsorbates on a crystal surface, in the manner of Stranski (102), where the energy between two atoms is taken to be proportional to the inverse sixth power of the distance and the effects of several neighboring atoms are additive—an assumption characterized as "naive" by Herring (95), but which has been found useful by many workers. In the second of the series, Drechsler used the same method for predicting the preferred direction of migration (either for foreign adsorbates or for tungsten on its own lattice) on various crystal surfaces. These are most readily understood by direct examination of a surface model such as that in Fig. 30, where it appears probable that superficially located atoms will migrate in the directions requiring the surmounting of the lowest saddles. Results were confirmed for several experimental examples, and agree also with the observations of Becker (25) somewhat earlier. It would be interesting to see further examples of the corresponding experimental activation energies for comparison with Drechsler's theoretical tables, as described for one case in the following paragraph.

Drechsler's third paper reported the direct measurement of activation energies of migration for barium adsorbed on various crystal faces of tungsten. This was accomplished by comparing the time required for altering an initial pattern into a recognizable final pattern at two different temperatures for each crystal face studied, and deducing the activation energy from a comparison of the two readings. Results were closely in accord with the theoretical energies calculated in Drechsler's first paper, varying from 0.20 ev/atom (corresponding to 4600 cal/mol) for barium on the (110) face to 1.45 ev (33,000 cal/mol) for lateral migration on the (112) surface, i.e., in the most difficult direction across the ridges of that surface. Such agreement with the theory may be fortuitous in view of the fact that the activation energy, which is obtained directly from the slope of the graph of logarithm of elapsed time vs reciprocal temperature as in Fig. 40, was apparently obtained from just two points of the graph, and furthermore was dependent upon qualitative visual judgment of the

emission patterns for the determination of equivalent surface distribution. The work is nevertheless notable as one of the few efforts to make such a comparison.

VI. ELECTRICAL STABILITY AND CATHODE LIFE

The unique electrical properties of the field emitter, described briefly in the introduction, suggest its application to a number of devices; however, widespread use of the cathode has not been practical heretofore because of its erratic performance and short life. For most applications, a time-independent current-voltage relationship is required, conditions for which are seen from Eq. (8). The most sensitive current dependence is on the exponential factor $\phi^{3/2}/\beta$.

Mechanisms altering β and ϕ , and hence the current density distribution, were identified in Sections III, 1, 2, and 5, their prevalence and effect accounting for the well-known erratic behavior of the cold cathode.

1. The Cold Cathode with Steady-State Fields

Two mechanisms will be illustrated here, one in which β is increased during sputtering by helium ions (115), and another in which ϕ changes through adsorption of chemically active gases. When such mechanisms are minimized, the resulting improvement in performance and life of the cold cathode in steady-state operation will be noted.

Energetic helium ions incident on tungsten cause local surface roughness at which β increases. As a result, J may increase at some areas by more than a factor of 10^3 , leading eventually to a localized vacuum arc which usually removes the surface projection and often spreads over the entire cathode tip, with a resulting discharge which is indistinguishable from the arcs described in Section IV.

Helium diffuses into some glass experimental tubes from the atmosphere; for a one-liter Pyrex flask in the normal atmosphere, the pressure rise is about 2×10^{-9} mm/hr, or of the order of 10^{-5} mm/yr. When field current is drawn at constant voltage, the rate of current increase with time is proportional to the helium pressure; a typical curve appears in Fig. 43 with corresponding emission patterns. Intense emission at small areas of surface roughness is shown in the speckled pattern C. An arc is initiated when the current increase exceeds about a factor of 2, although of course current density is the critical factor.

Residual gases in highly evacuated Pyrex tubes may alter the work function, thereby changing the current-voltage relationship in an undesired fashion. Such adsorption often has the effect shown in Fig. 44, in which current is depressed for a given voltage. Adsorption begins as a dark "X" on the (110)-(211) zones where sticking probability is high

(at *B*); the gas eventually covers the entire tip, thereby reducing the total current by a factor of about 100 from its initial value. Similar "X" patterns of this type result from oxygen (63), nitrogen (116), and hydrogen (117) on tungsten.

The foregoing problems were minimized and useful cathode life was extended when highly evacuated tubes having envelope materials with low helium diffusivity were used; a table of such materials is given by

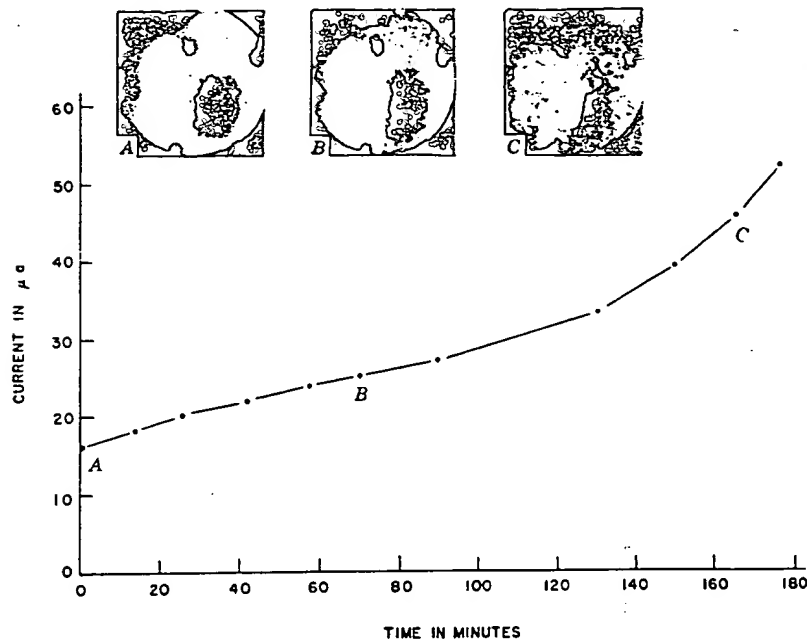


FIG. 43. A graph from the cold tungsten cathode showing the increase of emission current with time at constant voltage, attributed to cathode sputtering by atmospheric helium diffused into the Pyrex experimental tube; emission patterns show local current density increase at corresponding times.

Norton (118). In particular, a tube of lead glass, Corning 0120, with a pressure of chemically active gases of the order of 10^{-14} mm Hg, yielded the field current-time graph at constant potential shown in Fig. 45, in which no helium effect was detected. The gradual decrease in current with time was attributed to some residual adsorption.

Improved vacuum and surface cleanliness are a line of approach which holds further promise for stabilizing the performance of the cold cathode in steady-state operation. On the other hand, no material immune to changes in β and ϕ has yet been found. Although equilibrium coatings such as oxygen on tungsten exhibit very little further change in ϕ on con-

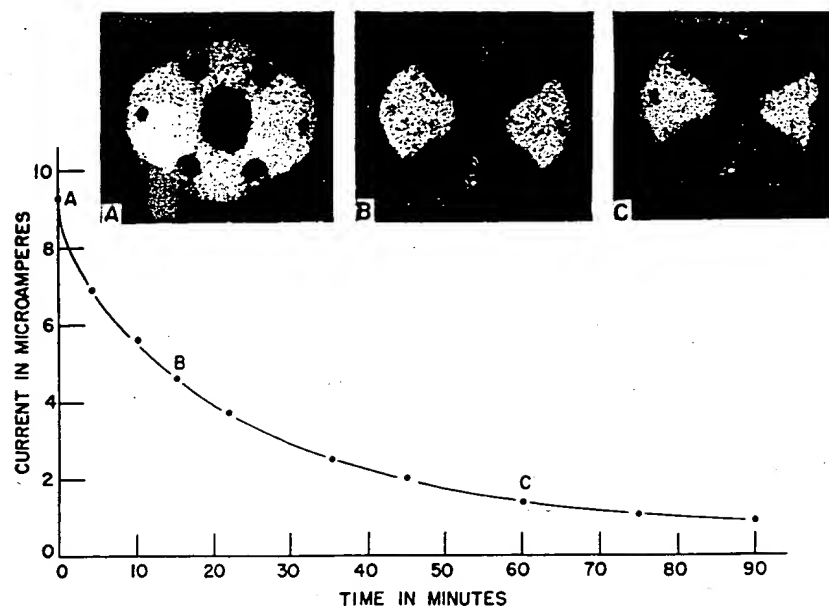


FIG. 44. A graph showing decrease of emission current with time at constant voltage, when residual oxygen in the tube contaminates the tungsten emitter surface as shown in the accompanying emission patterns; dark "X" in pattern B illustrates high sticking probability in the (110)-(211) region; for corresponding changes in work function see Fig. 34.

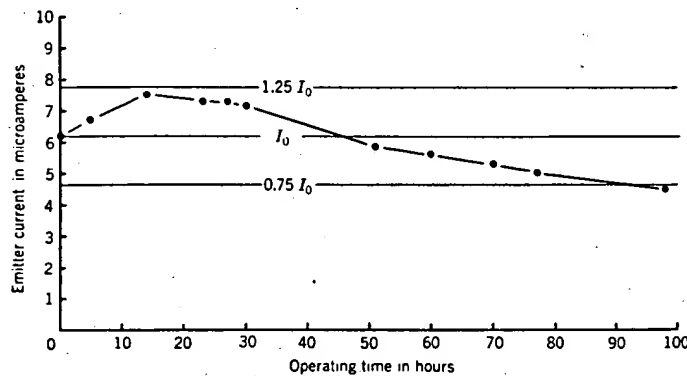


FIG. 45. A graph showing improved current-voltage stability of a cold tungsten cathode during steady-state operation in a tube of Corning 0120 glass, other conditions being similar to those for the experiment of Fig. 43.

tinuous exposure to the adsorbate, nevertheless, the mechanical strength of such surfaces is generally insufficient to resist geometric alteration when exposed to strong electrostatic forces. As a result, coated surfaces generally exhibit less stable electrical performance than does clean tungsten.

2. The T-F Emitter with Pulsed Fields

There are two observations which will be useful in the following discussion: first, the smooth, clean tungsten cathode exhibits excellent electrical stability (Fig. 45) and, second, favorable surface conditions can be restored by briefly elevating the cathode to high temperature in vacuum, in the absence of electric field.

The foregoing facts suggested the use of a continuously high temperature to stabilize the electrical performance of field emitters. Unfortunately, the method is not useful with steady-state fields, which, if large enough to give appreciable emission, are then sufficient to cause build-up (Section V,8). The method is useful with pulsed fields (119) when conditions are chosen (1) to limit build-up during the field-on period and (2) to permit surface forces to restore the original smooth, clean cathode surface during the field-off period. Conditions for limiting build-up (small dz) are seen from Eq. (34); since large values of F may be required for desired emission, dz can be restricted by limiting the field-on time dt and by a suitable choice of temperature and cathode material.

Tungsten is a useful material because of its low values of D at temperatures high enough to maintain a smooth, clean surface, e.g., $1700 < T < 2200^\circ \text{K}$. Under such conditions, fields up to $7 \times 10^7 \text{ v/cm}$ can be applied for periods up to at least 0.01 sec at duty cycles up to about 0.25. The current-voltage relationship then remains constant for long periods of useful operation, provided that means previously discussed are used to minimize cathode dulling. Its constancy is seen from its unchanging emission pattern and from current-voltage oscilloscopes; constancy is maintained at residual gas pressures less than about 10^{-4} mm Hg . Temperature must be high enough to maintain a smooth, clean surface in spite of incident material and will vary with the rate of incidence and type of material. Temperature must be low enough to minimize blunting, the volume diffusion of impurities to the surface, and thermal emission from cathode support structures. These factors determined the foregoing range for tungsten, which need be exceeded only in unusual cases, e.g., to remove carbon from the tip (110).

There are two problems introduced by thermal agitation. First, the needle-shaped cathode is gradually dulled by surface migration; dulling causes a decrease in β , which then requires an increase in voltage to maintain constant current. However, the dulling rate decreases with the third power of increasing radius, Eq. (35), and becomes practically negligible

for tungsten cathodes with radii $r > 7 \times 10^{-5}$ cm, when $T = 2000^\circ$ K, Fig. 41. Fortunately, many applications will use cathodes with radii sufficiently large that dulling can be neglected; for example, with $r = 3 \times 10^{-4}$ cm, no dulling was detected during 100 hr of operation. When smaller radii are required, a suitable steady-state bias electric field can minimize dulling; its resulting electrostatic forces oppose the forces derived from chemical potential that normally motivate surface migration (Section V,8).

The second difficulty introduced by thermal agitation results when impurities are supplied to the surface by volume diffusion, eruption at grain boundaries, etc. Such impurities can lower ϕ , increase J , and terminate cathode life through arc initiation by mechanisms described in Section IV. A typical eruption of about 10^6 atoms, believed to be thorium on tungsten (99, 120) has been visible in emission patterns, together with its subsequent dissipation. This suggests that cathode performance may improve with cathode purity; therefore, the cathodes described in the following table were made of a high-purity tungsten wire, Phillips Type HCA, which was subsequently heated for 30 hr in vacuum at temperatures in the range 1700 to 2800° K. Several such pulsed T - F tungsten cathodes have been subjected to life tests, typical results appearing in Table VII.

TABLE VII

Emitter No.	Peak current (amp)	Peak voltage (kv)	Pulses/sec	Pulse length (μ sec)	Life
					Tube type (hr)
Q-135	0.5	60	3	1	PTP* >100
Q-141	0.1	27	1000	1	PTP >103
Q-267	0.1	27	1000	1	PTP 50
Q-147	0.1	27	1000	1	FEM* 6
N-145	0.01 to 0.2	27-50	300-1000	1	FEM >200

* PTP: Point-to-plane, i.e., tungsten needle-shaped cathode, plane tungsten anode. FEM: Field-emission microscope, with tungsten needle-shaped cathode, and spherical aluminum-backed willemite anode, radius 4 cm.

Pressures in the quiescent tube were in the range 10^{-10} to 10^{-12} mm Hg for chemically active gases, 10^{-6} to 10^{-8} mm Hg for helium; during operation, chemically active gas pressures often increased to 10^{-6} mm Hg. While the effect of increasing duty cycle on cathode life is not yet well known, build-up of tungsten cathodes is observed at duty cycles greater than 0.25 with fields high enough for useful emission and $T > 2000^\circ$ K.

The developments just described provide for the first time a method for maintaining a stable field current-voltage relationship during long periods of pulsed operation at useful duty cycle and power and under

easily attained vacuum conditions. This will appreciably extend the usefulness of the field emitter in practical applications. Significant advances in electronic device development may result in view of the desirable and unique electrical properties of the cathode. Progress towards several devices is described in Section VII.

VII. PROGRESS TOWARDS PRACTICAL APPLICATION

1. Large Total Current

The improved stability and life of field and *T-F* emitters have stimulated renewed interest in the application of these cathodes to useful electronic devices. A number of such applications require large total current, which can be obtained only through large values of current density J or emitting area A , or both. In Section IV it was shown that the upper limit microsecond current density is in the range $10^7 < J < 10^8 \text{ amp/cm}^2$, depending on the particular cathode material and geometry, if a vacuum arc is to be avoided. At a given value of J , current can be increased to any reasonable level by increasing the value of emitting area. There are several methods for achieving this in practice: first, needles of larger tip radius; second, several needles operated in parallel; third, emitters of other geometry, such as a "razor edge." Since the latter possibility has had very little study, it will not be discussed further here.

Consider first the single needle with emission restricted to a hemispherical tip of radius r . Area increases with r^2 ; the maximum J permitted is proportional to r^{-1} when resistive heating is considered (Section IV). Hence, the maximum current obtainable from a needle increases with the first power of increasing tip radius. However, the current increase in this case is made at the expense of β , which, roughly speaking, is inversely proportional to radius (Section III,1). Approximately then, the required voltage increases linearly with the maximum current yield, assuming that work function, cone angle, and electrode spacing remain constant. Maximum microsecond current yields obtained experimentally from typical cathodes are shown in Table VIII; the largest microsecond current thus far obtained from a single tungsten needle is 6.5 amp, at 100 kv and with $r = 3 \times 10^{-4} \text{ cm}$.

TABLE VIII

Emitter radius (cm)	Applied voltage (kv)	Current (amp)
2×10^{-5}	5	0.05
5×10^{-6}	25	0.2
3×10^{-4}	100	6.5

Some devices require yet larger currents at various voltages, often less than 100 kv. Several needles in parallel operation lend themselves to such use. If β is chosen to match the given voltage, a proper choice of electrode geometries is required, particularly cathode radius and cone angle, and

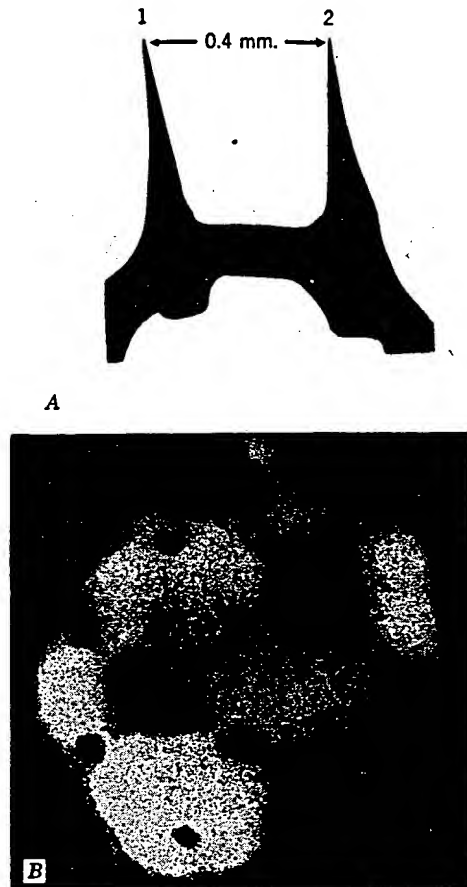


FIG. 46. (a) Micrograph of twin emitters, mounted on common filament, etched and vacuum heat-treated simultaneously; (b) simultaneous emission patterns obtained from twin emitters; equality of current densities indicates close matching of the field factor β for the two needles.

less important, the needle length, needle separation, and cathode-anode spacing.

At first glance, the fabrication of multiple needles with geometries adequately matched to insure current densities sufficiently alike appeared to be impossible. For example, for a current density variation of 10%,

the values of β can differ by no more than 1%, in view of the tables of Appendix I. This means that the product of cone angle and tip radius must be held constant from needle to needle within that limit, the question being how to achieve this for metallic objects of such small dimension, i.e., about 1μ .

The solution of the problem turns out to be surprisingly simple (121). Cone angles are reasonably uniform when multiple needles are formed simultaneously by the electrolytic etch method described in Section VIII,1. When the needles are heated simultaneously in vacuum, they dull by surface migration until the tip radii reach a value of about

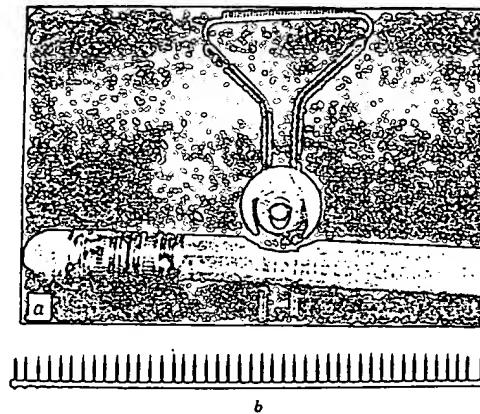


FIG. 47. Two views of a "comb"-type cathode, i.e., a linear array of needle-shaped emitters, mounted on common support, simultaneously fabricated, and suitable for parallel operation at a common potential.

$r = 7 \times 10^{-5}$ cm (Fig. 41), when the rate of dulling becomes negligible. The practical result is that all needles dull to nearly a common tip radius; hence their β 's are suited to simultaneous parallel operation at a common value of current density for a common applied voltage.

Two tungsten needles formed in this fashion are shown in Fig. 46; their overlapping emission patterns illustrate the approximate equality of their current densities, which was also established photometrically (Section III,2).

When the same technique was extended to a comb of 40 needles spot welded to a common 10-mil filament, Fig. 47, increased current was drawn as expected. When such a comb was spaced 1 mm from a plane tungsten anode, peak powers as large as 3 Mw were drawn during micro-second emission intervals. Typical values of peak current and voltage for two cathodes are indicated in Table IX.

TABLE IX

<i>I</i> (amp)	<i>V</i> (kv)
20	55
30	100

2. Application to X-ray Devices

Earlier workers were quick to recognize that field emission could be applied to the generation of x-rays, and considerable patent art may be found thereon (122); however, the practical value of such devices has heretofore been limited by lack of both adequate power and life. Improvements in both of the latter as described here have encouraged the development or suggestion of several new x-ray devices with field-emission sources.

The comb-type cathode described above has been applied to flash x-ray photography and cineradiography. When such a cathode is spaced about 1 mm from a plane tungsten anode and when the anode plane is appropriately inclined to the film, a linear x-ray source is formed which has the following advantages (123):

1. Small effective spot size, with resulting optical clarity.
2. High x-ray intensity, permitting microsecond exposures.
3. A repetitive pulse capability, characterized by a constant pulse-to-pulse output.

Field emission is a controlled process, as distinct from the relatively uncontrolled vacuum-arc cathodes previously applied to single-microsecond x-ray photography (124).

These features are illustrated in the several x-ray photographs of Fig. 48. Figure 48a shows a .22-caliber bullet stopped in flight on emergence from the gun barrel; use of x-rays avoids the smoke screen, and both the optical and time resolution are evident from the photographic sharpness. Figure 48b illustrates the repetitive pulse capability described above; an aperture pendulum, i.e., a hole in a swinging lead plate, is visible in several successive positions. Figures 48c and 48d illustrate the application of the flash x-ray source to acceleration studies, using a young rabbit under 1g and 20g accelerations, respectively. Noticeable are the vertebral separation and the movement of abdominal organs and facial tissues toward the head.

There are two proposed x-ray devices in which electron optical means are used to image the high-density point source of field emission electrons.

Pattee (125) has proposed a scanning field-emission x-ray microscope, in which the electron beam is focused into a small spot on a foil target,

with the specimen outside the foil in air, and a fluorescent screen beyond it. Marton and Schrack (126) have proposed a similar electron source as an improvement for the Cosslett x-ray microscope (127), which in its original form used a thermal cathode. Increased x-ray intensity with correspondingly decreased exposure time was one desired objective.

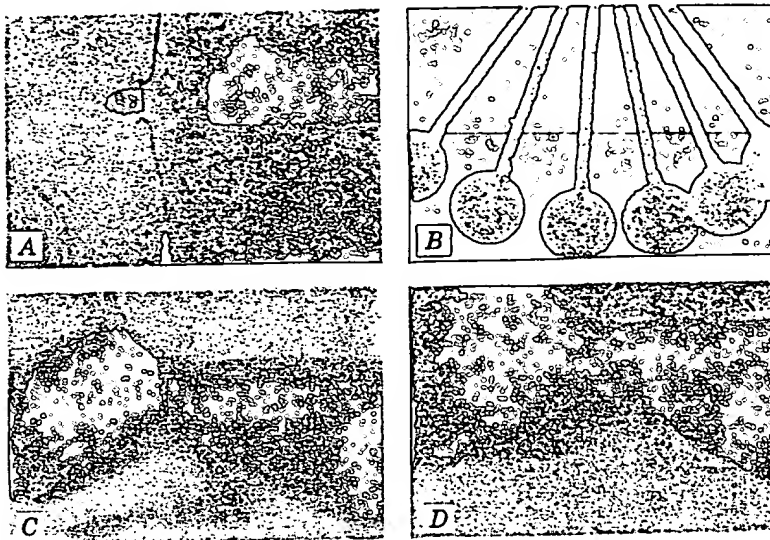


FIG. 48. X-ray photographs with microsecond exposures using field emission x-ray tube equipped with parallel cathode array as in Fig. 47: (a) bullet emerging from gun barrel; (b) aperture in lead-plate pendulum, taken with repetitive pulses; (c) body of rabbit attached to centrifuge at acceleration of 1 g; (d) same rabbit with centrifuge at 20 g, showing displacement of vertebrae, face tissue, and internal organs.

Attention has been called to other possible areas of application for the field and *T-F* emitters (4).

VIII. EXPERIMENTAL TECHNIQUES

1. Fabrication of Metal Cathodes

The requirement of high surface field at reasonable values of applied potential has led in all useful cases to sharp-pointed, needle-shaped field emitters. These have been experimentally fabricated in a variety of ways, including mechanical grinding (24), chemical etching (36, 63), and electrolytic etching (26, 77). In at least one case, emission was obtained from the end of a broken wire (37), and undesired field emission from irregularities of undetermined geometry doubtless contributes to many cases of electrical breakdown in vacuum (Section IV). Electrolytic etching,

however, has come to be regarded as the most satisfactory method of fabrication because it is convenient and reproducible and usually results in a simple and useful geometric configuration. Considerable variety in techniques exists; those described here have been found to be most uniformly satisfactory in this laboratory. The ideal fabrication procedure would be one that could be duplicated by any operator at will and would lead to a predicted emitter geometry whose details could be controlled by known variations in the process. Although considerable progress in

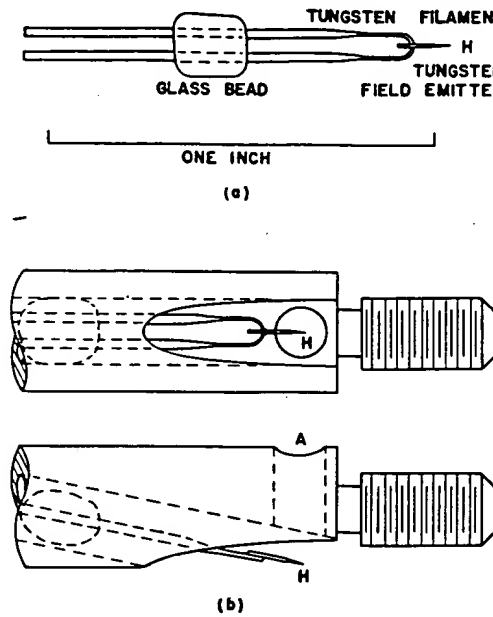


FIG. 49. (a) Typical field cathode assembly. (b) Modified sample rod for RCA type EMT electron microscope, with field cathode assembly inserted.

this direction has been made, emitter fabrication still remains to some degree an art, subject to the individual skill and experience of the worker. The general shape of the emitter, its smoothness and uniformity, the radius of the tip, and the cone angle are significant variables subject only imperfectly to deliberate control, yet increasingly well understood.

Tungsten, because of its high melting point, great mechanical strength and good electrical properties, has been the most widely used emitter material. The cathode is usually a needle of about 1-mm length spot-welded to a structure which provides mechanical support and serves as a heating element, the latter to shape and clean the needle tip, and later to maintain its electrical stability (Section VI). The illustration of Fig. 49a shows the usual method of mounting used here; different arrange-

ments have been used successfully elsewhere (3). The U-shaped supporting filament is of 15-mil tungsten wire, reduced in the apex region to about 4 mils by electrolytic etching. This localizes the high-temperature region when the emitter is to be heated electrically by filament current; it also smooths away surface irregularities that might lead to undesired emission, for example at spot welds. The emitter blank, spot-welded to the filament, is of 5-mil wire of high purity (e.g., Phillips Type HCA), extensively preheated to encourage the growth of large crystals and to further localize or remove residual impurities. For tungsten, an electrolyte of 1.0 normal NaOH is used, in which the emitter blank is one electrode and a nickel helix is the other. A 60-cycle alternating potential of about 10 v is applied. Control of the voltage, the time of etching, and the depth of immersion of the blank are all at the operator's disposal. The resulting tip will be generally conical; larger angles are obtained by lower potential and smaller depth of immersion, while smaller angles follow use of higher potential and deeper immersion. Since the entire immersed portion of the wire would eventually be removed, the time of etching is a critical factor. The current is switched off at the operator's discretion, after a sharp point is formed but before too much material is removed. The completed emitter should not extend more than 1 or 2 mm beyond the filament, since otherwise it is difficult to heat because of radiation loss.

After the emitter is thus formed, heat treatment in vacuum at 2200° C or more removes small irregularities by preferential surface migration and by the same process tends to increase the tip radius. This treatment may be accomplished at the same time that the structure is heated to degas it during evacuation of the experimental tube. The dulling rate is dependent on the radius (Fig. 41) so that very fine points are dulled rapidly but larger ones more slowly; in fact, the rate becomes so slow at a radius of about 7×10^{-5} cm (Section V,8) that larger tips cannot be conveniently obtained by this method. The cone angle has considerable influence on the shape achieved by heating. Emitters of relatively large angle retain their shape well, while small-angle emitters tend to develop a bulbous tip. Both radius and cone angle are significantly related to the field factor β , as already mentioned. Figure 50 includes typical examples of the results of heat treatment after etching.

If emitters of larger radius, say 10^{-4} cm or more, are desired in order to operate them at relatively high voltages or to obtain higher total current from the larger emitting area, special fabrication methods are needed. In one of these, a long-tapered point of small cone angle is etched as described above, then lifted partially from the solution and subjected to a higher dc potential, say 75 v, which has the effect of truncating the cone at the surface of the solution. It is then lowered more deeply again

and the ac etch applied just long enough to round off the truncated tip, resulting in an emitter of large radius but small cone angle.

Another method of preparing emitters of large radius is to subject them deliberately to a vacuum arc as described in a previous section. If the total energy during the arc is limited, the result as revealed in electron micrographs is an enlarged point, as if melted back (Fig. 21b shows an extreme example), which in favorable cases may be useful for further operation at higher potentials. Enough experiments with such arcs have been performed to give assurance that it is possible to control the change

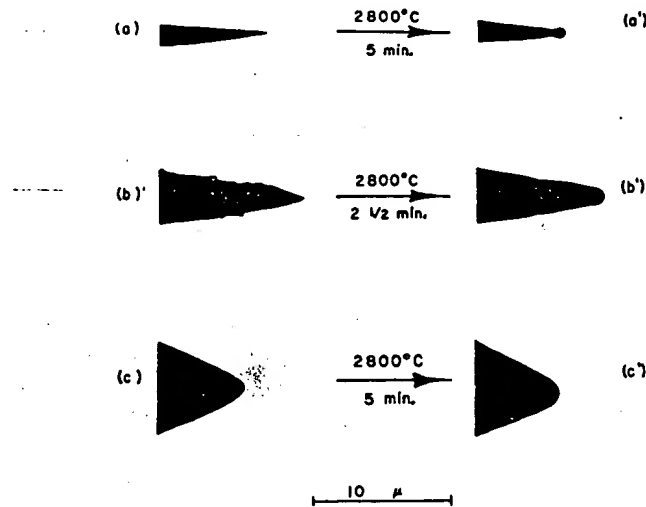


FIG. 50. Typical electron micrographs of field emitters, indicating use of the electron microscope for comparison of emitter profiles before (left) and after (right) the designated heat treatments.

in radius usefully. During arc the tip is melted and recrystallized, and the resulting surface appears to be of exceptionally high purity as judged by its emission pattern and subsequent stable electrical performance.

It is also possible to use a gaseous discharge accompanying large field current to bombard, enlarge, and smooth a tungsten cathode. The energy thus imparted to the cathode has been controlled by use of pulse techniques, with the result that reasonably well-controlled changes in cathode geometry were obtained. For example, a microsecond discharge was used to round the tip of a tungsten needle which had been truncated by the electrolytic method described above.

Cathodes of very small radius, on the other hand, may be useful for low-voltage work or for the sake of the high resolution obtainable in their patterns (Section V,2). A useful method first proposed by Müller (35) is

sometimes known as the "oxygen etch." Oxygen is admitted into the tube while the emitter is heated and forms a tungsten oxide layer on the metal surface which is readily evaporated, leaving an extremely sharp point; Müller, in his early work, obtained enough emission for a visible pattern at less than 100 v from such an emitter corresponding to a radius of about 10^{-6} cm; however, the pattern was not clean, and further heating to remove contaminants increased the radius at the same time. In Section V,8 it is pointed out that a low-level steady-state bias electric field can stabilize the geometry of small heated emitters.

Very small emitters, in the form of surface roughness on tungsten, are formed when low field currents are drawn in argon or helium (128); β is thus increased locally so that the required voltage for constant current is reduced. Tips of small radius (estimated $r < 10^{-6}$ cm) can be formed at such surface projections by this method, and these may often be useful in experiment. However, reasonable total currents are obtained only with high current density, leading to practical difficulties noted in Section IV.

Equilibrium between the radius-increasing heat treatment and the radius-decreasing oxygen etch has been obtained experimentally, temperature and oxygen pressure being appropriately balanced in the absence of field. Presumably, each combination of the two variables would maintain a certain radius so that the current-voltage relationship could be maintained constant.

The fabrication of multiple tungsten needles for parallel operation is described in Section VII.

Other metals have required different etching procedures; those given here have in no case been subject to the same extensive experience as tungsten, but have met with some success and are therefore described briefly. Molybdenum may be etched by the same method used for tungsten. Iron emitters were prepared by Schleicher (81) using perchloric-acetic acid into which the wire was quickly dipped; the process was accelerated by using dilute HCl at intervals. A HCl electrolytic etchant has also been used in this laboratory (84). Gomer (79) described his own process for preparing nickel as ". . . electrolytic etching in a 30% HCl solution, saturated with $KClO_4$, at 1-20 volts ac, until smooth points could no longer be resolved in a light microscope at 500-fold magnification. The points were then rinsed carefully in distilled H_2O ." Gomer also suggested fabricating tantalum by electrolytic etch, using equal parts of HF and H_2SO_4 at 40 v dc.

Platinum has been prepared by a three-stage process beginning with etching in 11 normal NaOH at 15 v ac (which left a rough surface); it was then smoothed by heating in vacuum at $1600^\circ C$ for 2 min, then further sharpened in concentrated HNO_3 at 6 v ac for about 5 min. In

the case of Barnes' work with rhenium (82), where low-voltage etching in an aqueous solution of 1.0 normal NaOH was ineffective, success was gained by applying a high enough ac potential (from 25 to 35 volts) to produce a visible arc under the surface of the liquid. From 10 to 30 pulses of about 0.05 sec each were required before optical microscope inspection indicated satisfactory results, confirmed in the electron microscope. An alternate method which has been successful with rhenium is the use of 8 normal H₂SO₄ at about 15 v dc, wherein the arc was not necessary to achieve satisfactory results.

Although other metals have been used for experimental field emitters as mentioned above, methods of preparation have not been described.

2. Determination of Cathode Geometry

Most field-emission experiments require for their quantitative interpretation an accurate determination of cathode geometry; examples include but are by no means limited to (1) calculation of electric field (Section III,1), (2) area and current-density distribution (Section III,2), (3) surface-migration studies (Section V,8), (4) the resistive generation of heat and its flow (Section IV), (5) the resolution of electron emission from a lattice edge (Section V,7), (6) the simultaneous operation of multiple needles in parallel (Section VII), (7) calculation of work function from observed field-current density (Section III,5), (8) cathode fabrication, etc.

Surprisingly little of the published field-emission work includes a sufficiently well-determined geometry. This doubtless accounts for the considerable existing disagreement in conclusions drawn therefrom; a typical example is found in the field dependence, which has only recently come into reasonable agreement with theory. The small physical dimensions of a field emitter, commonly between 10⁻⁶ and 10⁻⁴ cm in radius and frequently an order of magnitude smaller, preclude the adequate resolution of its geometry by optical microscopy and suggest the use of conventional electron microscopy, as first employed by Haefer (36) and Benjamin and Jenkins (77).

One reason for the earlier neglect of the method was the difficulty of adapting certain microscope models for convenient examination of emitters. The available sample holding devices were small in size and of such design that the emitter tip had to be removed from its supporting filament, mounted very delicately in the instrument, then removed with considerable danger of loss or damage and with little hope of subsequent remounting for operation. A solution for these difficulties was found in a modification of the sample rod of the RCA Type EMT instrument (129), making it possible to mount the entire field emission cathode assembly

with the emitter tip in viewing position, and later to demount the assembly for operation and subsequent re-viewing.

Figures 49b and 51 show such a modification and are self-explanatory. The instrument is adapted either to direct viewing of the magnified emitter profile on a luminescent screen or to photographic recording of the image. A magnification of about $3000\times$ is suitable for most purposes, being large enough to reveal surface details in the profile, yet small enough so that the emitter tip is visible over a length of several radii from the vertex. With such techniques, it is possible to keep a permanent

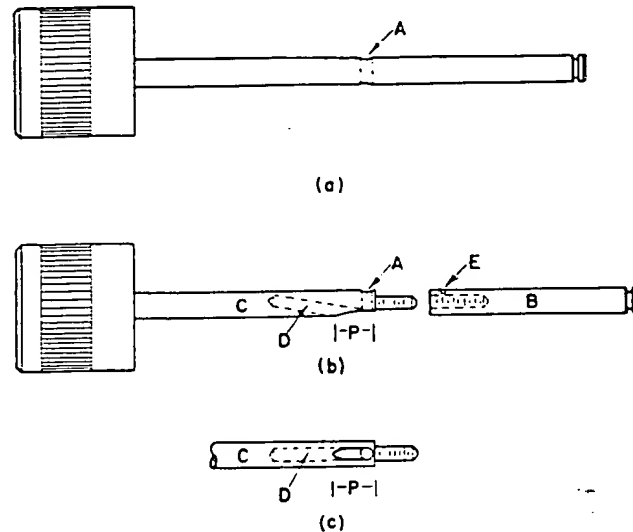


FIG. 51. Sample rods for RCA type EMT electron microscope: (a) normal rod, (b) and (c) modified rod. Section *B* remains in microscope as vacuum seal while Section *C* is removed to insert field cathode assembly in cavity *D* as in Fig. 50; electron beam is at *A*.

record of the shadowgraphs of all emitters, correlated with a history of their fabrication and subsequent treatment.

The sample rod described above is limited to one position of the emitter at an insertion. To view another profile, it is necessary to remove the emitter support from the rod and reinsert it in another position. Since emitters do not always display radial symmetry, it may be desirable to examine several profiles. For this purpose, a further modification (130) was devised, but will not be described in detail here. The entire sample rod is so designed that it may be rotated from outside the instrument through any desired angle and returned accurately to its initial position through reference to a graduated angular scale. It is thus possi-

ble to detect irregularities or asymmetry quickly by visual examination, then to photograph the emitter profile from any pertinent angle.

A third modification (130) includes a pair of fine wires for use as electrical leads for the purpose of heating the emitter while mounted in the microscope. One use for this device was described in Section V,8 and involved a study of the time rate of change of emitter radius under surface migration at various temperatures.

The possibility exists of a more extensive modification of the instrument to permit observation of an emitter profile during actual operation as a field emitter. The advantages of such an arrangement for several purposes are obvious, but no attempt has been made to accomplish it. The difficulty of controlling the electrons of the microscope beam in the presence of the second field necessary for emitter operation points toward the possibility of using alternate short pulses for the two functions.

ACKNOWLEDGMENTS

The authors wish to acknowledge with thanks the friendly cooperation of many authors who have supplied reprints or manuscripts of their own work and have given permission for reference to such material here. The use of previously published papers in several cases has been authorized by publishing agencies in a generous manner.

Colleagues on the staff of Linfield College have contributed to many of the results reported here, well beyond the limits of individual credit in the references. They have also been most helpful in the preparation and editing of the manuscript and illustrations. The Linfield College research was initiated through grants by Research Corporation. Much of the research described has been performed under later contract support from the Office of Naval Research and the Wright Air Development Center of the U.S. Air Force; the continuous cooperation of these agencies is gratefully recognized.

APPENDIX I. Common logarithms of field current density J in amp/cm², from Eq. (5), for various values of electric field F in v/cm and work function ϕ in ev.

$F \times 10^{-2}$ (v/cm)	ϕ (ev)				
	2.00	2.50	3.00	3.50	4.00
1.0	3.04	-0.54	-4.45	-8.64	
1.2	4.51	+1.48	-1.80	-5.32	
1.4	5.56	2.94	+0.10	-2.94	
1.6	6.36	4.04	1.53	-1.14	
1.8	6.98	4.90	2.66	+0.26	
2.0	7.48	5.59	3.56	1.39	-0.90
2.2	7.90	6.16	4.30	2.32	+0.22
2.4	8.25	6.64	4.92	3.09	1.16
2.6	8.54	7.05	5.45	3.75	1.96
2.8		7.40	5.91	4.32	2.65
3.0		7.71	6.30	4.82	3.25
3.2		7.98	6.65	5.25	3.78
3.4		8.22	6.96	5.64	4.24
3.6		8.43	7.24	5.98	4.66
3.8		8.63	7.49	6.29	5.03
4.0		8.80	7.71	6.57	5.37
4.2		8.96	7.92	6.82	5.67
4.4			8.11	7.06	5.96
4.6			8.28	7.27	6.21
4.8			8.44	7.46	6.44
5.0			8.59	7.65	6.66
5.2			8.72	7.82	6.87
5.4			8.85	7.97	7.05
5.6			8.97	8.12	7.23
5.8			9.08	8.25	7.39
6.0			9.18	8.38	7.55
6.2			9.28	8.50	7.69
6.4				8.61	7.83
6.6				8.72	7.95
6.8				8.82	8.07
7.0				8.92	8.19
7.2				9.01	8.30
7.4				9.09	8.40
7.6				9.18	8.50
7.8				9.25	8.59
8.0				9.33	8.68
8.2				9.40	8.76
8.4				9.47	8.84
8.6					8.92
8.8					9.00
9.0					9.07
9.2					9.14
9.4					9.20
9.6					9.27
9.8					9.33
10.0					9.39

APPENDIX I. (Continued)

$F \times 10^{-7}$ (v/cm)	ϕ (ev)					
	4.35	4.50	4.65	5.00	5.50	6.30
2.0	-2.58	-3.32	-4.06	-5.85	-8.50	-12.97
2.2	-1.31	-1.99	-2.66	-4.30	-6.71	-10.78
2.4	-0.25	-0.87	-1.50	-2.99	-5.22	-8.96
2.6	+0.65	+0.08	-0.50	-1.89	-3.95	-7.41
2.8	1.43	0.90	+0.36	-0.94	-2.86	-6.08
3.0	2.11	1.61	1.10	-0.11	-1.91	-4.92
3.2	2.70	2.23	1.75	+0.61	-1.08	-3.91
3.4	3.22	2.78	2.33	1.25	-0.34	-3.02
3.6	3.69	3.27	2.84	1.82	+0.32	-2.22
3.8	4.11	3.71	3.30	2.34	0.90	-1.50
4.0	4.49	4.11	3.72	2.80	1.44	-0.85
4.2	4.84	4.47	4.10	3.22	1.92	-0.27
4.4	5.15	4.80	4.45	3.60	2.35	+0.26
4.6	5.44	5.11	4.76	3.95	2.76	0.75
4.8	5.71	5.38	5.06	4.28	3.13	1.20
5.0	5.95	5.64	5.33	4.58	3.47	1.62
5.2	6.18	5.88	5.58	4.85	3.78	2.00
5.4	6.39	6.10	5.80	5.11	4.08	2.35
5.6	6.59	6.31	6.02	5.35	4.35	2.68
5.8	6.77	6.50	6.22	5.57	4.60	2.99
6.0	6.94	6.68	6.41	5.78	4.83	3.28
6.2	7.10	6.85	6.59	5.97	5.06	3.55
6.4	7.26	7.01	6.76	6.16	5.28	3.81
6.6	7.40	7.16	6.91	6.33	5.48	4.04
6.8	7.53	7.30	7.06	6.50	5.66	4.27
7.0	7.66	7.43	7.20	6.65	5.84	4.48
7.2	7.78	7.56	7.33	6.80	6.00	4.68
7.4	7.90	7.68	7.46	6.93	6.16	4.88
7.6	8.01	7.80	7.58	7.07	6.31	5.06
7.8	8.11	7.90	7.69	7.19	6.46	5.23
8.0	8.21	8.01	7.80	7.31	6.60	5.40
8.2	8.31	8.11	7.91	7.43	6.72	5.55
8.4	8.40	8.20	8.00	7.54	6.85	5.70
8.6	8.48	8.29	8.10	7.64	6.97	5.85
8.8	8.57	8.38	8.19	7.74	7.08	5.98
9.0	8.65	8.46	8.28	7.84	7.19	6.12
9.2	8.72	8.54	8.36	7.93	7.30	6.24
9.4	8.80	8.62	8.44	8.02	7.40	6.36
9.6	8.67	8.69	8.52	8.10	7.49	6.48
9.8	8.94	8.76	8.59	8.18	7.58	6.59
10.0	9.00	8.83	8.66	8.26	7.67	6.69
12.0	9.54	9.40	9.25	8.91	8.41	7.58
14.0		9.83	9.69	9.39	8.95	8.23
16.0				9.76	9.37	8.72
18.0					9.70	9.12
20.0					9.97	9.44

APPENDIX II. Common logarithms of emission current density J (amp/cm²) as a function of temperature T ($^{\circ}$ K), electric field F (v/cm), and work function ϕ (ev).

NOTE: In some cases, entries for 500 $^{\circ}$ and 1000 $^{\circ}$ are smaller than those tabulated in Appendix I for $T = 0^{\circ}$ because of the difference in methods of calculation as outlined in text.

F	T						
	500	1000	1500	2000	2500	3000	3500
$\phi = 4.0$ ev:							
2×10^7	-1.79	-0.09	1.72	3.43	4.64	5.46	6.05
3	3.26	3.50	4.03	4.85	5.63	6.25	6.75
4	5.34	5.47	5.72	6.11	6.56	6.98	7.35
5	6.61	6.69	6.84	7.07	7.34	7.62	7.88
6	7.47	7.53	7.63	7.78	7.96	8.15	8.35
7	8.09	8.14	8.22	8.32	8.45	8.58	8.71
8	8.57	8.61	8.67	8.74	8.83	8.93	9.03
9	8.95	8.98	9.02	9.08	9.15	9.22	9.30
10	9.26	9.28	9.31	9.36	9.41	9.46	9.52
$\phi = 4.5$ ev:							
2×10^7	-3.18	-2.34	-1.40	2.20	3.64	4.63	5.38
3	1.63	1.91	2.55	3.62	4.63	5.46	6.04
4	4.09	4.24	4.53	5.01	5.61	6.17	6.65
5	5.59	5.70	5.87	6.13	6.48	6.85	7.22
6	6.61	6.68	6.80	6.97	7.19	7.45	7.70
7	7.35	7.40	7.49	7.61	7.77	7.95	8.13
8	7.92	7.96	8.02	8.11	8.23	8.36	8.50
9	8.36	8.39	8.44	8.51	8.60	8.70	8.81
10	8.72	8.75	8.79	8.84	8.92	9.00	9.08
$\phi = 5.0$ ev:							
2×10^7	-5.69	-4.66	-1.63	0.91	2.63	3.78	4.63
3	-0.07	0.24	1.01	2.37	3.63	4.59	5.33
4	2.79	2.96	3.28	3.87	4.63	5.34	5.99
5	4.54	4.64	4.83	5.14	5.58	6.06	6.50
6	5.73	5.80	5.92	6.12	6.39	6.71	7.03
7	6.58	6.64	6.73	6.86	7.05	7.28	7.52
8	7.24	7.28	7.35	7.45	7.58	7.75	7.93
9	7.75	7.78	7.84	7.92	8.02	8.15	8.29
10	8.16	8.19	8.24	8.30	8.39	8.49	8.59

REFERENCES

1. Wood, R. W., *Phys. Rev.* **5**, 1 (1897).
2. Jenkins, R. O., *Repts. Progr. Phys.* **9**, 177 (1943).
3. Müller, E. W., *Ergeb. exakt. Naturw.* **27**, 290 (1953).
- 3a. Ashworth, F., *Advances in Electronics* **3**, 1 (1951).
4. Dyke, W. P., *Proc. Inst. Radio Engrs.* **43**, 162 (1955).
5. Schottky, W., *Z. Physik* **14**, 63 (1923).
- 5a. Müller, E. W., *Z. Physik* **131**, 136 (1951).

6. Fowler, R. H., and Nordheim, L. W., *Proc. Roy. Soc. A119*, 173 (1928).
7. Nordheim, L. W., *Proc. Roy. Soc. A121*, 626 (1928).
8. Sommerfeld, A., and Bethe, H., "Handbuch der Physik." (Vol. 24, Part 2, p. 441. Springer, Berlin, 1933.)
9. Guth, E., and Mullin, C. J., *Phys. Rev.* **61**, 339 (1942).
10. Frank, N. H., and Young, L. A., *Phys. Rev.* **38**, 80 (1941).
11. Miller, S. C., Jr., and Good, R. H., Jr., *Phys. Rev.* **91**, 174 (1953).
12. Burgess, R. E., Kroemer, H., and Houston, J. M., *Phys. Rev.* **90**, 515 (1953).
13. Dolan, W. W., *Phys. Rev.* **91**, 510 (1953).
14. Henderson, J. E., and Dahlstrom, R. K., *Phys. Rev.* **55**, 473 (1939).
15. Müller, E. W., *Z. Physik* **120**, 261 (1943).
16. Gomer, R., *J. Chem. Phys.* **20**, 1772 (1952).
17. Richter, G., *Z. Physik* **119**, 406 (1942).
18. Dolan, W. W., and Dyke, W. P., *Phys. Rev.* **95**, 327 (1954).
19. Millikan, R. A., and Eyring, C. F., *Phys. Rev.* **27**, 51 (1926).
20. de Bruyne, N. A., *Phil. Mag.* **5**, 574 (1928).
21. Nakai, J., *Technol. Repts. Osaka Univ.* **1**, 213 (1951).
22. Houston, W. V., *Phys. Rev.* **33**, 361 (1929).
- 22a. Bardeen, J., *Phys. Rev.* **49**, 653 (1936).
23. Millikan, R. A., and Lauritsen, C. C., *Proc. Natl. Acad. Sci. (U.S.)* **14**, 45 (1928).
24. Eyring, C. F., Mackeown, S., and Millikan, R. A., *Phys. Rev.* **31**, 900 (1928).
25. Becker, J. A., *Bell System Tech. J.* **30**, 907 (1951).
26. Dyke, W. P., Trolan, J. K., Dolan, W. W., and Barnes, G., *J. Appl. Phys.* **24**, 570 (1953).
27. Smythe, W. R., "Static and Dynamic Electricity." McGraw-Hill, New York, 1949.
28. Dyke, W. P., and Trolan, J. K., *Phys. Rev.* **89**, 799 (1953).
29. Drechsler, M., and Henkel, E., *Z. angew. Phys.* **6**, 341 (1954).
30. Drechsler, M., and Müller, E. W., *Z. Physik* **134**, 208 (1953).
31. Müller, E. W., *J. Appl. Phys.* **26**, 732 (1955).
32. Wilkinson, M. K., *J. Appl. Phys.* **24**, 1203 (1953).
33. Dyke, W. P., Trolan, J. K., Dolan, W. W., and Grundhauser, F. J., *J. Appl. Phys.* **25**, 106 (1954).
34. Houston, J. M., private communication.
35. Müller, E. W., *Z. Physik* **108**, 668 (1938).
36. Haefer, R. H., *Z. Physik* **116**, 604 (1940).
37. Stern, F., Gossling, B., and Fowler, R. H., *Proc. Roy. Soc. A124*, 699 (1929).
38. Barbour, J. P., Dolan, W. W., Trolan, J. K., Martin, E. E., and Dyke, W. P., *Phys. Rev.* **92**, 45 (1953).
39. Sachs, R. G., and Dexter, D. L., *J. Appl. Phys.* **21**, 1304 (1950).
40. Smoluchowski, R., *Phys. Rev.* **60**, 661 (1941).
41. Lewis, T. J., *Proc. Phys. Soc. B67*, 187 (1954).
42. Müller, E. W., *Z. Physik* **102**, 734 (1936).
43. Nichols, M. H., *Phys. Rev.* **57**, 297 (1940).
44. Trolan, J. K., Barbour, J. P., Martin, E. E., and Dyke, W. P., *Phys. Rev.* **100**, 1646 (1955).
45. Smith, G. F., *Phys. Rev.* **94**, 295 (1954).
46. Hutson, A. R., *Phys. Rev.* **98**, 889 (1955).
47. Goss, W. H., and Henderson, J. E., *Phys. Rev.* **56**, 857 (1939).
48. Henderson, J. E., *Phys. Rev.* **41**, 261A (1932).
- 49a. Henderson, J. E., and Badgley, R. E., *Phys. Rev.* **38**, 540 (1931).

- 49b. Henderson, J. E., and Dahlstrom, R. K., *Phys. Rev.* **45**, 764A (1934).
50. Dyke, W. P., Ph.D. Thesis, University of Washington, unpublished.
51. Gomer, R., and Hulm, J. K., *J. Chem. Phys.* **20**, 1500 (1952).
52. Fleming, G. M., and Henderson, J. E., *Phys. Rev.* **58**, 887 (1940).
53. Nottingham, W. B., *Phys. Rev.* **59**, 906 (1941).
54. Fleming, G. M., and Henderson, J. E., *Phys. Rev.* **59**, 907 (1941).
55. Dyke, W. P., Barbour, J. P., Martin, E. E., and Trolan, J. K., *Phys. Rev.* **99**, 1192 (1955).
56. Cranberg, L., *J. Appl. Phys.* **23**, 51S (1952).
57. Trump, J. G., and Van de Graaff, R. J., *J. Appl. Phys.* **18**, 327 (1947).
58. Webster, W. M., Van de Graaff, R. J., and Trump, J. G., *J. Appl. Phys.* **23**, 264 (1952).
59. Germer, L. H., and Haworth, F. E., *J. Appl. Phys.* **20**, 10S5 (1949).
60. Bennett, W. H., *Phys. Rev.* **45**, 891 (1934).
61. Dyke, W. P., Trolan, J. K., Martin, E. E., and Barbour, J. P., *Phys. Rev.* **91**, 1043 (1953).
62. Dolan, W. W., Dyke, W. P., and Trolan, J. K., *Phys. Rev.* **91**, 1054 (1953).
63. Müller, E. W., *Z. Physik* **106**, 541 (1937).
64. Ignateva, L. A., and Kalashnikov, S. G., *Zhur. Eksppl. i Teor. Fiz.* **22**, 385 (1952).
65. Germer, L. H., *J. Appl. Phys.* **22**, 955 (1951).
66. Germer, L. H., *J. Appl. Phys.* **22**, 1133 (1951).
67. Germer, L. H., and Smith, J. L., *J. Appl. Phys.* **23**, 553 (1952).
68. Germer, L. H., *J. Appl. Phys.* **25**, 332 (1954).
69. Kisliuk, P., *J. Appl. Phys.* **25**, 897 (1954).
70. Boyle, W. S., and Germer, L. H., *J. Appl. Phys.* **26**, 571 (1955).
71. Boyle, W. S., Kisliuk, P., and Germer, L. H., *J. Appl. Phys.* **26**, 720 (1955).
72. Müller, E. W., *Z. Elektrochem.* **59**, 372 (1955).
73. Johnson, R. P., and Shockley, W., *Phys. Rev.* **49**, 436 (1936).
74. Rose, D. J., *J. Appl. Phys.* **27**, 215 (1956).
75. Müller, E. W., 16 mm. Film, Deutsche Physikalische Gesellschaft, Karlsruhe (Sept. 1951).
76. Müller, E. W., *Z. Physik* **120**, 270 (1943).
77. Benjamin, M., and Jenkins, R. O., *Proc. Roy. Soc. A176*, 264 (1940).
78. Birkshenkel, H., Haefer, R., and Mezger, P., *Acta Phys. Austriaca* **7**, 402 (1953).
79. Gomer, R., *J. Chem. Phys.* **21**, 293 (1953).
80. Martin, E. E., unpublished.
81. Schleicher, H. W., *Z. Naturforsch.* **76**, 471 (1952).
82. Barnes, G., *Phys. Rev.* **97**, 1579 (1955).
83. Brock, E. G., and Taylor, J. E., *Phys. Rev.* **98**, 1169A (1955).
84. Daughenbaugh, M., unpublished thesis, Linfield College, McMinnville, Ore.
85. D'Asaro, L. A., *Bull. Am. Phys. Soc.* **30**, No. 7, 31A (1955).
86. Müller, E. W., *Z. Naturforsch.* **5a**, 473 (1950).
87. Becker, J. A., Abstracts of Field Emission Seminar, Linfield College, McMinnville, Ore., 1952 (unpublished).
88. Müller, E. W., *Sci. American* **186**, 58 (May 1952).
89. *Life*, **28**, 67 (June 19, 1950).
90. Wolf, P., *Z. angew. Phys.* **6**, 529 (1954).
91. Becker, J. A., *Advances in Catalysis* **7**, 136 (1955).
92. Gomer, R., and Speer, D. A., *J. Chem. Phys.* **21**, 73 (1953).
93. Haefer, R., *Acta Phys. Austriaca* **8**, 105 (1953).
94. Müller, E. W., Electron Microscope Society of America, 1953 (unpublished).

95. Herring, C., in "Structure and Properties of Solid Surfaces" (R. Gomer and Smith, C. S., eds.), p. 5. U. of Chicago Press, Chicago, 1953.
96. Müller, E. W., *Naturwissenschaften* **29**, 533 (1941).
97. Müller, E. W., *Phys. Rev.* **102**, 618 (1956).
98. Inghram, M. G., and Garner, R., to be published; also *J. Chem. Phys.* **22**, 1279 (1954).
99. Dyke, W. P., and Barbour, J. P., *J. Appl. Phys.* **27**, 356 (1956).
100. Verma, A. R., "Crystal Growth and Dislocations. Academic Press, New York, 1953.
101. Müller, E. W., *Z. Physik* **126**, 642 (1949).
102. Stranski, I. N., and Suhrmann, R., *Ann. Physik* [6] **1**, 153 (1947).
103. Herring, C., *J. Appl. Phys.* **21**, 301 (1950).
104. Langmuir, D. B., *Phys. Rev.* **86**, 642A (1952).
105. Drechsler, M., Pankow, G., and Vanselow, R., *Z. physik. Chem. [N.S.]* **4**, 249 (1955).
106. Barbour, J. P., to be published.
107. Gomer, R., and Hulm, J. K., *J. Am. Chem. Soc.* **75**, 4114 (1953).
108. Gomer, R., and Wortman, R., to be published.
109. Klein, R., *J. Chem. Phys.* **21**, 1177 (1953).
110. Klein, R., *J. Chem. Phys.* **22**, 1406 (1954).
111. Kruse, P. W., and Coomes, E. A., *Phys. Rev.* **93**, 929A (1954).
112. Drechsler, M., *Z. Elektrochem.* **58**, 327 (1954).
113. Drechsler, M., *Z. Elektrochem.* **58**, 334 (1954).
114. Drechsler, M., *Z. Elektrochem.* **58**, 340 (1954).
115. Martin, E. E., to be published.
116. Becker, J. A., private communication.
117. Gomer, R., private communication.
118. Norton, F. J., *J. Am. Ceram. Soc.* **36**, No. 3 (1953).
119. Dyke, W. P., Barbour, J. P., Trolan, J. K., and Martin, E. E., *Phys. Rev.* **98**, 263A (1955); Dyke, W. P., Abstracts, Westinghouse Field Emission Symposium, Pittsburgh (November 1954).
120. Becker, J. A., and Brattain, W. H., *Phys. Rev.* **43**, 428 (1933).
121. Dyke, W. P., to be published.
122. Lilienfeld, J. E., *U. S. Patent* 1,559,714 (1920).
123. Dyke, W. P., to be published.
124. Slack, C. M., *Phys. Rev.* **58**, 206 (1940).
125. Pattee, H. H., Jr., *Phys. Rev.* **92**, 541A (1953).
126. Marton, L., and Schrack, R. A., Abstracts, Westinghouse Field Emission Symposium, Pittsburgh (November 1954); also L. Marton, *Natl. Bur. Standards Circ.* **527** (1951).
127. Cosslett, V. E., and Nixon, W. C., *J. Appl. Phys.* **24**, 616 (1953).
128. Müller, E. W., *Z. Physik* **106**, 132 (1937).
129. Reisner, J. H., and Dornfeld, E. G., *J. Appl. Phys.* **21**, 1131 (1950).
130. Boling, J. L., and Perry, L. M., to be published.